ABSTRACT

An Experimental Investigation of Round and Racetrack Shaped Jets for Leading Edge Region Cooling of Gas Turbine Blades

Weston V. Harmon, M.S.M.E.

Mentor: Lesley M. Wright, Ph.D.

Jet impingement is often utilized in the leading edge of actively cooled turbine airfoils to protect the blades from the extreme heat loads encountered within the engine. This thesis will discuss two experimental investigations that employ a traditional, steady state, copper plate technique to obtain regionally averaged Nusselt numbers on a concave surface, which models the leading edge of a turbine blade. The first experiment will investigate the effect of jet shape, orifice edge condition, jet-to-jet spacing, and relative jet length. The effect of inlet supply condition will also be investigated by implementing a radial bypass. The second experiment investigates the effect of rotation on both round and racetrack shaped impinging jets. Results show that racetrack shaped jets generally outperform circular jets both in a stationary test section, and under rotating conditions. Further, the effects of non-square edge conditions and radial bypass prove to be detrimental to heat transfer.

An Experimental Investigation of Round and Racetrack Shaped Jets for Leading Edge Region Cooling of Gas Turbine Blades

by

Weston V. Harmon, B.S.M.E.

A Thesis

Approved by the Department of Mechanical Engineering

_____

William Jordan, Ph.D., Chairperson

Submitted to the Graduate Faculty of
Baylor University in Partial Fulfillment of the
Requirements for the Degree
of

Master of Science in Mechanical Engineering

Approved by the Thesis Committee

_____

Lesley M. Wright, Ph.D., Chairperson

_____

Stephen T. McClain, Ph.D.

_____

Michael W. Thompson, Ph.D.

Accepted by the Graduate School

August 2014

_____

J. Larry Lyon, Ph.D., Dean

Page bearing signatures is kept on file in the Graduate School.

TABLE OF CONTENTS

LIST OF FIGURES

LIST OF TABLES

NOMENCLATURE

A_c	Cross-sectional area of supply duct
A_s	Convective surface area
Bi	Biot Number
Bo	Buoyancy number for impingement jet
D	Diameter of curved target surface
D_1	Plenum diameter
D_2	Diameter of the orifice plate
$d_{h,\ duct}$	Hydraulic diameter of the supply duct
d_{jet}	Diameter of round jet, hydraulic diameter of racetrack-shaped jet
G	Specific gravity of air
h	Convective heat transfer coefficient
H	Jet-to-target surface distance
K	Discharge coefficient
k_{air}	Thermal conductivity of air
k_{al}	Thermal conductivity of aluminum
L_c	Characteristic Length
$\dot{m}_{impinge}$	Mass flow rate of fluid being used for impingement
$\dot{m}_{supply}$	Total mass flow rate of supply fluid
NGV	Nozzle Guide Vane
Nu	Regionally or locally averaged Nusselt number on target surface
$Nu_{Average}$	Surface averaged Nusselt number

Nu_{avg}	Surface averaged Nusselt number
Nu_{Stag}	Stagnation region averaged Nusselt Number
$Nu_{Stationary}$	Nusselt numbers in the stationary channel
$\overline{Nu}$	Circumferential averaged Nusselt Number
P_1	Absolute static pressure upstream of the orifice
P_{Duct}	Perimeter of supply duct
P_{Jet}	Perimeter of jet orifice
ΔP	Pressure differential across the orifice
$\dot{Q}$	Rate of heat transfer
$\dot{Q}_{high}$	Power supplied to heater during high heat loss calibration
$\dot{Q}_{loss}$	Power lost to ambient surroundings during testing
$\dot{Q}_{low}$	Power supplied to heater during low heat loss calibration
$\dot{Q}_{net}$	Net rate of heat transfer
r	Radial distance from jet centerline
R	Resistance of the flexible heater(s)
$\overline{R}$	Mean rotating radius of test section
Re	Reynolds number
Re_{duct}	Supply duct Reynolds number
Re_{jet}	Jet Reynolds number
R_{fillet}	Fillet radius of the jet
RIT	Rotor Inlet Temperature
Ro	Rotation number for impingement jet
RT	Racetrack

s	Streamwise spacing of jets
SS	Steady state
t	Jet plate thickness
T_1	Temperature at the inlet of the orifice
TBC	Thermal Barrier Coating
T_{jet}	Bulk jet temperature
T_c	Coolant Temperature
T_{high}	Plate temperature during high heat calibration case
TLC	Thermochromatic liquid crystal
T_{low}	Plate temperature during low heat calibration case
T_{room}	Room temperature during impingement testing
$T_{room, high}$	Room temperature during high heat calibration case
$T_{room, low}$	Room temperature during low heat calibration case
T_w	Regional surface temperature
T_∞	Mainstream fluid temperature
V	Voltage supplied to the the flexible heater(s) or free jet velocity
V_{duct}	Average supply duct velocity
V_{jet}	Average jet velocity
w	Total mass flow rate of air
W	Jet diameter
x	Streamwise location on the target surface
X	Streamwise location on the target surface
y	Supercompressability factor

Y	Expansion factor
z	Jet-to-target surface distance
μ	Dynamic viscosity of cooling air
ρ	Density of cooling air
Ω	Rotating speed of test section

ACKNOWLEDGMENTS

Completing my graduate degree has proved to be one of the most challenging pursuits in my life thus far. Furthermore, the writing of this thesis has been a process I have been haunted with for the last two years. In hindsight, it wasn't as terrible as I thought it would be, and that is due to the amazing people that I have been fortunate enough to be surrounded by during my long academic career.

I am eternally grateful to my academic mentor, Dr. Lesley Wright, whose constant guidance, and often times necessary prodding, were crucial during my time here at Baylor University. Dr. Wright has demonstrated incredible patience with me over the last three years that I have been performing research. Lastly, her passion for research and her students has been evident as long as I have known her, and it is this that truly makes her a great mentor, colleague, and friend. Additionally, I would like to extend my gratitude to Honeywell Inc., under the advisement of Dan Crites, for their generous funding and commitment to the research I was performing. Mr. Crites and the rest of the Honeywell team provided valuable insight and recommendations throughout the course of this research project.

I would like to extend my deepest appreciation to Dr. Stephen McClain and Dr. Michael Thompson for serving on my thesis committee. I would also like to thank Baylor University and the entire mechanical engineering faculty and staff for their knowledge and support throughout my six years on this campus. This school has provided me with countless memories, and I can say with all certainty that these six have been the best years of my life.

I am grateful to Mr. Ashley Orr for his mechanical expertise in designing and building anything he is asked to. I was fortunate enough to have the opportunity to work in his machine shop during my undergraduate years, and the knowledge and know-how he instilled in me during that time is priceless. Additionally, Ashely is a great friend, and a wonderful personality within the department. I know I drove him crazy, and he took it like a champ.

I would also like to thank the previous graduate students from the 107 for setting such a high standard to strive for. Specifically I would like to extend my appreciation to Neil Jordan, who initially convinced me to get involved in undergraduate research. Neil and his successor, Cassius Elston, both provided tremendous knowledge and encouragement as I was moving into my graduate degree. I would also like to thank my fellow graduate students Charlie Brown, Trae Liller, and Chris Walker for their support as we journeyed through graduate school.

I am also thankful to the Baylor University Stonewall ultimate team for providing a physical outlet to help me keep my sanity. I thoroughly enjoyed the friendships I made, and the opportunity to represent Baylor University in competition.

Finally, I can honestly say that I would not have made it through this journey without the unconditional support I received from my family. The values of hard work that they instilled in me have proven invaluable. I would also like to thank my wife, Brooke, who put up with me through the early mornings, late nights, and weekends when I was working. To all of you, thank you.

DEDICATION

To my family and my wife Brooke
without whose love and encouragement, this would not have been possible

CHAPTER ONE

Introduction

Gas Turbine Engines with Modern Cooling Technology

Gas turbine engines have become an integral part of the world; each day these engines are used to meet a variety of power and propulsive requirements. Most notably, these engines are used as the propulsion system for aircraft. Their usefulness does not end with aircraft; gas turbine engines can be found on cruise ships, helicopters, military tanks, and are often paired with an electrical generator to supply power for industrial applications and residential communities. Given the breadth and importance of these applications, it is clear why these gas turbine engines must operate as efficiently as possible. Gas turbine engines operate on the Brayton cycle and have three main components: the compressor, the combustor, and the turbine. A cut-away view of a typical gas turbine engine used for aircraft propulsion can be seen in Figure 1.1.

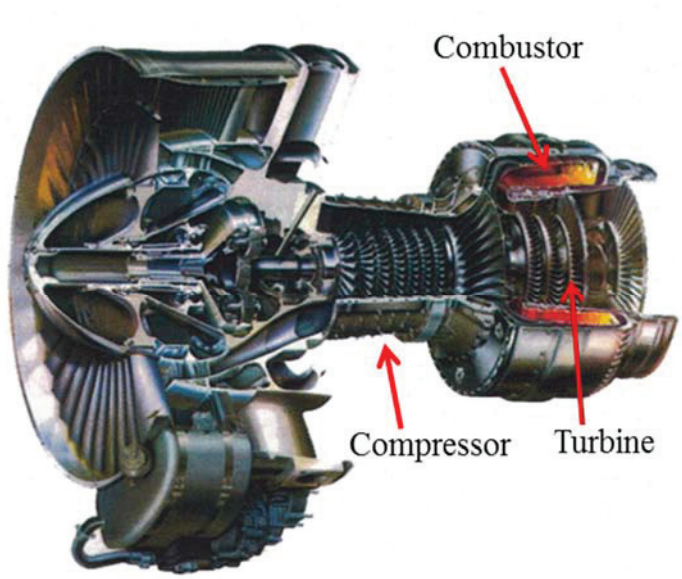

Figure 1.1: Cut-away view of Honeywell Aerospace ALF502.

The compressor takes ambient air and compresses it in successive stages. The now high pressure, high temperature air enters the combustor where fuel is added. Once ignited the gas increases in temperature and expands rapidly as it exits the combustor and enters the turbine. The turbine uses airfoils to extract the kinetic energy of the mainstream gas and converts it to shaft work to drive the compressor. For propulsive applications, it is important for the turbine to only remove enough energy to drive the compressor as the additional energy of the mainstream flow will be necessary to provide thrust. Power generation turbines, however, attempt to capture and convert as much of the energy from the flow with the turbine as possible. One approach to increasing power within the engine is to increase the overall temperature of the hot gases entering the high pressure turbine of the engine. This temperature is commonly referred to as the rotor inlet temperature (RIT). Figure 1.2 shows how the specific core power of a gas turbine engine is directly related to the RIT, as well as how engine technology has progressed over time.

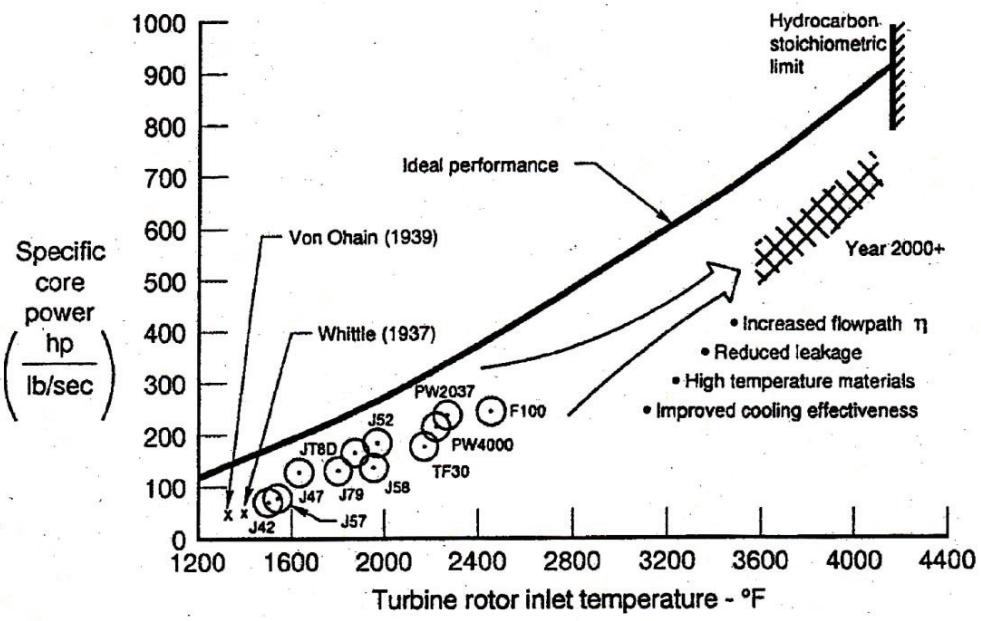

Figure 1.2: Effect of rotor inlet temperature on power produced by turbine [1].

Turbine blade cooling can be divided into two sub-categories: internal cooling and external cooling. Figure 1.3 provides an illustration of the various cooling techniques used throughout the turbine airfoil.

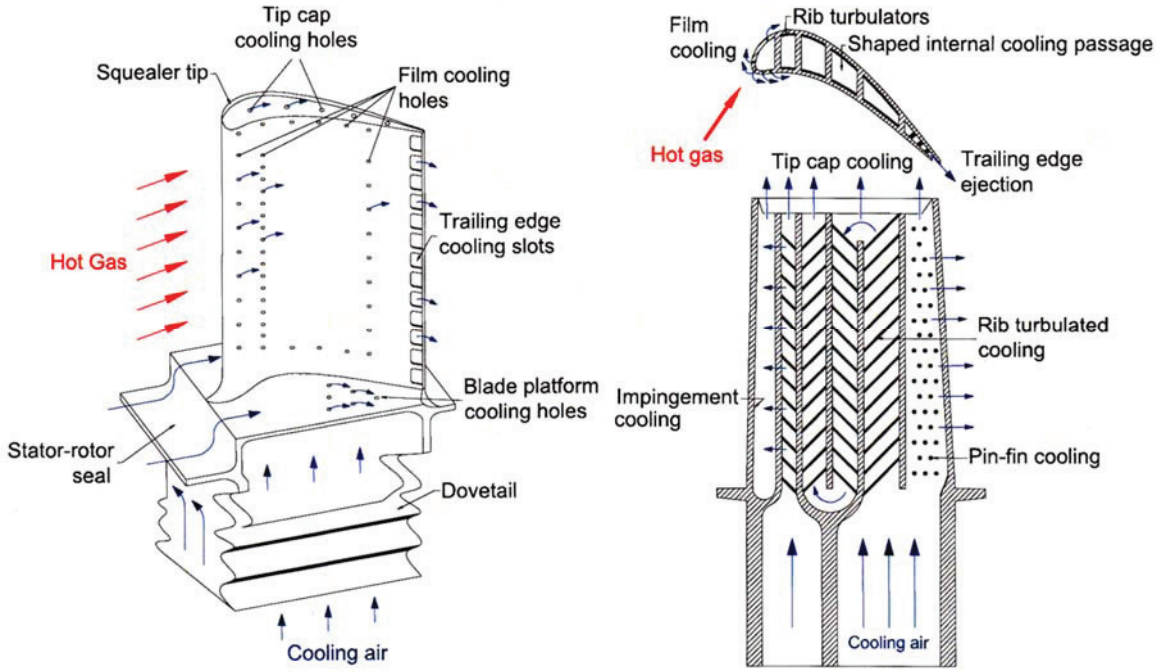

Figure 1.3: Commonly used internal and external cooling techniques for a turbine airfoil [2].

In general, relatively cool air from the compressor is passed through the interior passages of the blade, used for internal cooling, and then ejected to the outside of the blade to be used for external cooling. This external cooling process known as film cooling provides protection on the exterior surface of the airfoil by creating an insulating film of air, or buffer zone, between the hot mainstream gas and the surface of the turbine blade. Unfortunately, by introducing this cooling fluid to the mainstream, the bulk temperature of the working fluid is decreased, which in turn, reduces the power that can be produced by the engine. Because of this, it is important for engine designers to maximize the effectiveness of their film cooling schemes as this will allow for a

minimum amount of coolant to be expelled from the blade. External cooling also includes the application of a thermal barrier coating (TBC), which is typically a ceramic-like material. The TBC reduces heat transfer to the blade by offering a decreased thermal conductivity compared to that of the blade material.

For internal cooling, techniques include several means to induce additional turbulence by adding surface features (i.e. rib turbulators, dimples, or pin-fins), all of which increase heat transfer by providing additional mixing of the warm fluid near the surface and the cool core of the cooling fluid. Pin-fins are generally employed in the trailing edge of turbine airfoils for additional structural support where the blade walls are very thin. Ribs and dimples are utilized most often in the mid-chord region of the airfoil. Another form of internal cooling is that of jet impingement. Jet impingement consists of blowing a jet of relatively cool air onto a surface, and is perhaps the most aggressive form of internal turbine blade cooling. Because of this, jet impingement is typically used in the leading edge of turbine blades where the heat load is the highest, as shown in Figure 1.4.

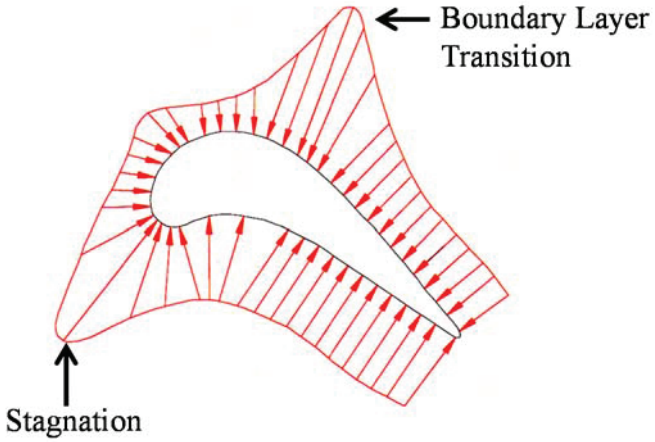

Figure 1.4: Heat load distribution on a turbine blade [2].

Jet impingement can also be found in the mid-chord region of select stator airfoils (particularly the nozzle guide vane just downstream of the combustion chamber). Generally, cool air is supplied for impingement via channel flow where one or more of the channel walls are perforated with a row or array of discrete jets. Cool air makes its way through these orifices and impinges on the surface intended to be cooled.

Characteristics of an Impinging Jet

As mentioned previously, impingement cooling for gas turbine engines utilizes relatively cool, high pressure air that has been siphoned from the compressor. This cool air is routed through the internal passages of the turbine airfoil and, in the case of impingement, is forced through a discrete orifice before stagnating on the intended target surface. Figure 1.5 provides an illustration of a typical impinging jet.

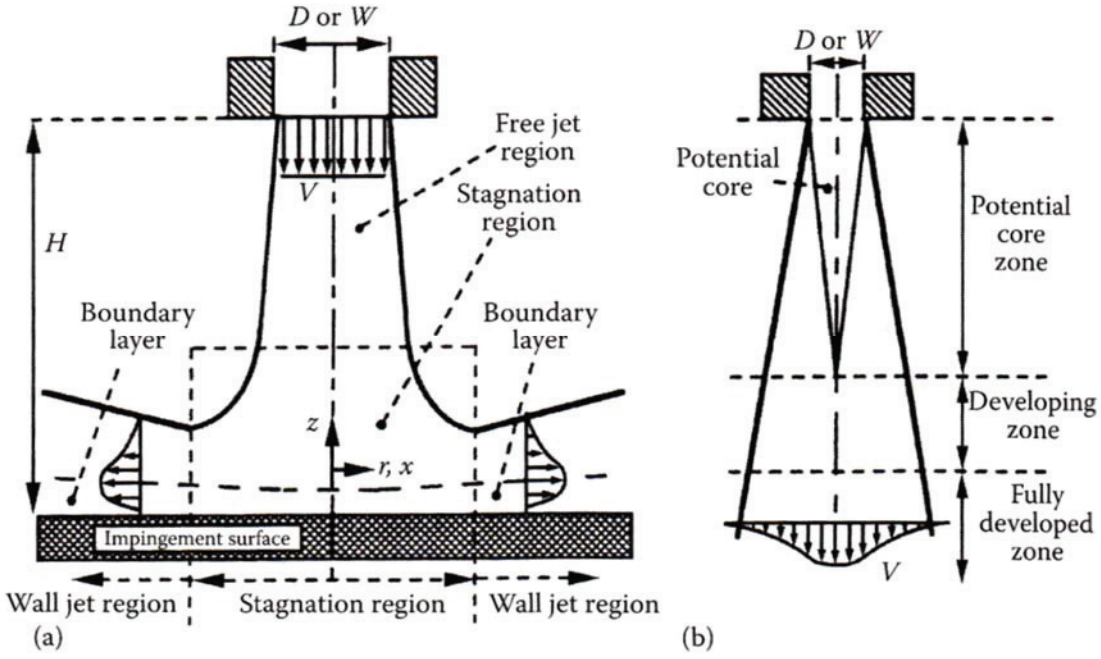

Figure 1.5: (a) Flow regions of an impinging jet; (b) Flow regions of a free jet [3].

In general, there are three distinct regions that characterize impingement flow: the free jet, the stagnation region, and the wall jet. The free jet consists of the region immediately after the exit of the orifice until the jet begins to feel effects of the target surface. The characteristics of this region are very similar to what one would expect from a typical, unconfined free jet. Perhaps the most important part of the free jet region is the potential core. Within this potential core there exists a uniform velocity profile and the flow is unaffected by the surrounding ambient air. However, as the flow moves further away from the exit of the orifice, the potential core begins to diminish. Researchers have shown that the potential core diminishes quickly upon exiting the orifice (generally within four to six jet diameters of the exit of the orifice [3]). Additionally, the heat transfer trends associated with jet impingement are extremely sensitive to whether the potential core is still intact upon stagnation. The weakening of the potential core as it exits the jet is a direct result of the interactions between the fast moving fluid of the jet, and the slow moving, or stagnant, fluid within the impingement channel. As the coolant moves further away from the exit of the orifice, the formation of a shear layer around the jet entrains ambient fluid. This mixing effect propagates as the air moves further from the orifice exit, resulting in radial spreading of the jet. Once the potential core is fully diminished this spreading continues, and the jet velocity is further reduced.

The stagnation region of an impinging jet begins where the free jet begins to feel the presence of and ultimately strikes the target surface. The flow begins to decelerate as it approaches the target surface, and then quickly accelerates parallel to the surface. This sudden change in flow direction and acceleration results in thin boundary layers on the target surface, and thus high heat transfer. For an impinging jet there are two heat transfer

trends typically observed. Which trend will occur is dependent on whether or not the potential core is still intact when the coolant strikes the target surface. If the jet-to-target surface spacing is sufficient to allow the potential core to fully dissipate, the resulting heat transfer trend will look much like a Gaussian curve. This is because the highest heat transfer occurs at the very center of the jet upon striking the target surface. As the flow moves radially outward from the jet center, the boundary layer thickens and heat transfer decreases. On the other hand, if the jet-to-target surface spacing lends itself to the existence of the potential core, a secondary maxima will be observed in the Nusselt number. The first peak will again occur at the very center of the jet. Once the potential core strikes the target surface, the flow turns and accelerates along the surface. The second peak is caused by the transition of the boundary layer from laminar to turbulent as the coolant accelerates away from the stagnation region. Figure 1.6 presents the two heat transfer trends typically observed from an impinging jet.

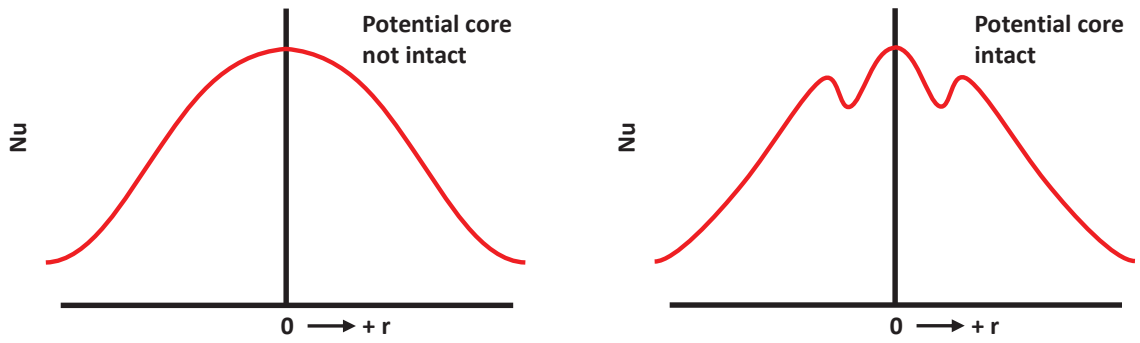

Figure 1.6: Nusselt number distributions for varying jet-to-target surface spacing.

The final region of an impinging jet is the wall jet. The wall jet occurs as the spent coolant air exits the stagnation region and begins to decelerate. There are two forces acting on the spent air to cause this. On the target surface, the shear forces that form as a

result of the no-slip condition aide in the deceleration. Additionally, slow moving ambient air is entrained on the exposed side of the wall jet, much like was seen with the free jet, slowing the fluid down further. Similar to the stagnation region, as the wall jet moves further away from the location of impingement, the heat transfer on the target surface will gradually decrease. Because impinging jets are often part of an array, the heat transfer characteristics of an impingement cooling scheme can be improved by taking advantage of wall jet interactions of multiple jets. When the wall jet regions of two or more jets interact, secondary mixing flows are induced that can create areas of increased heat transfer on the target surface. However, the management of the spent coolant for large impingement arrays is crucial. If the spent air is not removed efficiently from the impingement cavity, the, now warmer, impinged air will be entrained, and can degrade target surface Nusselt numbers.

Statement of the Problem

The majority of past impingement literature has focused on the heat transfer characteristics afforded by a circular, square edged jet. However, this is not indicative of the current geometries utilized in modern turbine blade designs. Due to manufacturing limitations, impingement orifices often turn out misshapen and with rounded inlet and outlet edges. Additionally, it is important to identify how realistic inlet supply conditions affect the performance of an impinging jet. Limited work has been performed to quantify the heat transfer characteristics of varying orifice shapes with varying inlet flow conditions. Because of this, it is imperative that these relevant impingement conditions are examined extensively. Not only is this necessary to ensure that the “imperfect” hole

geometries are providing adequate heat transfer, but it can also as a tool to potentially enhance the complex impingement cooling schemes currently in use. Furthermore, the effect of high rotation on jet impingement will be examined for varying jet geometries. Because jet impingement is most commonly utilized in areas of turbine airfoils under the highest heat loads, it is vital that researchers fundamentally understand the effect of high rotation on an impinging jet in order to implement the most effect cooling schemes possible.

Aims and Objectives

This thesis aims to provide the quantitative heat transfer characteristics of varying jet geometries with varying inlet flow characteristics in the leading edge of a turbine blade. For the non-rotating portion of this research, the TLC impingement test section used by Jordan et al. [4-7] was modified to accommodate a new custom target surface. A classic steady state heat transfer experiment was conducted with this new target surface, and will allow for the examination of various jet shapes and edge conditions. In addition, the effect of varying inlet supply conditions will also be investigated. Initially the objective of the steady state experiment was to validate the results obtained by Jordan et al. [4-7]. In addition to the work performed by Jordan et al. [4-7], the effect of varying other geometric parameters was investigated. These include: jet-to-jet spacing and additional values of the jet thickness. Furthermore, this research has the potential to provide valuable insight into the performance of circular and racetrack shaped jets under the various geometric conditions tested.

The objective of the rotating portion of this research is to build on the previous study conducted by Elston et al. [8]. However, instead of using multiple impinging jets, a single jet will be utilized in an attempt to isolate the effect of rotation on a single jet rather than the effect of rotation coupled with crossflow effects. Using a single jet minimizes the effect of spent air crossflow. It could be argued that since a typical turbine blade uses an array of impinging jets for cooling, data for a single jet will not provide a realistic model of rotating impingement flow. However, the researchers feel that showerhead film cooling provides adequate removal of spent air thus making the testing of a single jet applicable. Additionally, the performance of both a circular and racetrack jet under high rotation conditions will be investigated in this study.

CHAPTER TWO

Literature Review

Cooling techniques within gas turbine engines are constantly progressing, so it is important for engine designers to remain current on the state of research within the gas turbine community. As previously mentioned, there are various methods used to cool the many regions of turbine blades. This chapter will provide a fundamental review of jet impingement research relevant to the present study.

Jet impingement is most often found in the leading edge region of turbine blades and the mid-chord region of stator vanes where heat loads are highest. Jet impingement cooling on curved surface (leading edge) introduces numerous complexities; therefore, it is important to first understand the fundamental characteristics of jet impingement on a flat plate (mid-chord region). After a brief overview of flat plate impingement characteristics, features of jet impingement on a curved surface can be discussed along with the heat transfer trends associated with varying the geometric parameters associated with leading edge impingement. The geometric properties of the jets themselves will also be discussed at length, including varying parameters such as jet shape, relative jet length, and edge condition. Additionally, the effect of varying supply flow conditions will be examined. Finally, the effect of rotation on turbine cooling techniques will be discussed.

Flat Plate Impingement

For decades, engine designers have been utilizing jet impingement, as well as, various other cooling techniques mentioned previously. Large scale jet impingement

(when a large surface area is needed to be cooled) is typically reserved for the mid-chord region of stator vanes, particularly in the first stage, nozzle guide vane. The nozzle guide vane is the first obstacle encountered by the hot mainstream gases as they exit the combustion chamber. As a result, the nozzle guide vane is subject so some of the most extreme heat loads found in gas turbine engines.

A typical stator airfoil, shown in Figure 2.1, contains a hollow channel through the center. Cooling air is routed into this channel and then travels through discrete jets that line the channel to impinge on the interior surface of the airfoil. Because the target surface has a relatively large radius of curvature, flat plate impingement studies are typically used to model the heat transfer trends for this region. Additionally, the mid-chord region comprises a significant portion of the surface area of the airfoil; therefore, large arrays of impingement jets are typically utilized for cooling.

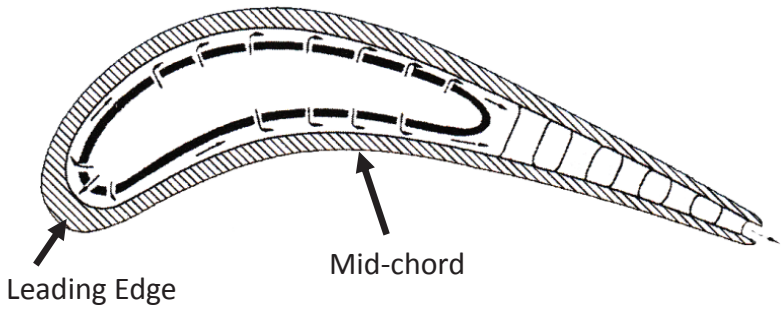

Figure 2.1: Cross-sectional view of the Nozzle Guide Vane (NGV) [9]

In 2013, Han et al. [1] assembled a comprehensive review of open literature pertaining to gas turbine cooling techniques, and the fundamental trends for impingement cooling will be highlighted here. For jet impingement on a flat surface, the heat transfer is dependent on several parameters: jet Reynolds number (Re_{jet}), jet-to-jet spacing (s/d_{jet}), and jet-to-target surface spacing (z/d_{jet}). It should be noted that often times length based

parameters, such as jet-to-jet spacing and jet-to-target surface spacing, are normalized by the diameter of the jet to allow for comparison of multiple studies that may or may not utilize the same jet or test section dimensions.

Once a jet impinges on a surface, the spent cooling air quickly attempts to exit the channel. As the cooling air moves through the channel, it begins to accumulate and create a crossflow effect. As the air moves toward the channel exit the crossflow effect intensifies as additional spent air accumulates. Because of this, crossflow near the target surface can have a significant effect on the heat transfer within the channel. For flat plate impingement, in general, as the Reynolds number is increased, one can expect increased heat transfer on the target surface. It has also been shown that there is only marginal variation in the level of heat transfer observed when the jet-to-target surface spacing is less than approximately 5 diameters ($0 < z/d_{jet} < \sim 5$). Once the spacing exceeds approximately 5 diameters the jet has ample distance to allow for the potential core of the jet to diminish resulting in lower jet velocities striking the surface. Subsequently, decreased heat transfer coefficients will be observed on the target surface.

It has also been shown that reducing jet-to-jet spacing (until you approach a continuous slot jet) will continue to increase target surface heat transfer. This increase in overall target surface heat transfer is attributed to having more jets in the same area and having less of the target surface area receiving low heat transfer, rather than providing higher peak Nusselt numbers in the stagnation region. However, this comes at a cost of more coolant flow. By moving the jets closer together, designers can take advantage of the jet-to-jet interactions that provide increased mixing and, therefore, higher heat transfer. It was mentioned earlier that once the jet-to-jet spacing becomes so small that

the jet shape approaches a continuous slot, a decrease in the surface heat transfer coefficients would be observed. This is because a slot jet provides two dimensional flow characteristics, while discrete jets benefit largely from the three dimensional mixing caused by the jets interacting.

For impingement arrays, the arrangement of jets becomes important. There are two common ways to arrange jets, a staggered array or an inline array. Examples of these arrangements can be seen in Figure 2.2. Because of the crossflow generated by the spent air of the jets in the impingement channel, the two arrangements can provide significantly different heat transfer capabilities.

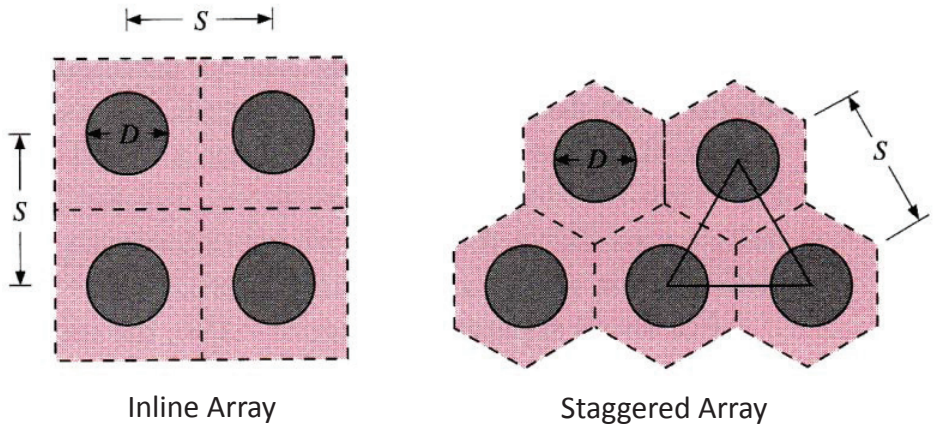

Figure 2.2: Illustration of two common orifice arrangements [10].

Once discharged, the spent impingement air is swept toward the exit of the channel. The spent air from a single jet is not significant, but when dealing with multiple jets, the spent air quickly accumulates, and the crossflow grows stronger. Once the bulk motion of the fluid is moving parallel to the target surface, the impinging jet is deflected, thus increasing the jet-to-target surface distance and degrading the heat transfer performance in the stagnation region. For a staggered array, downstream jets will see a

large crossflow effect, and the jets will begin to deflect rather quickly. In addition, the jet is no longer impinging perpendicular to the surface which results in decreased heat transfer in the stagnation region. An inline array, on the other hand, provides a channel between the rows of jets which facilitates the removal of spent air with less degradation of the stagnation region heat transfer. Figure 2.3 illustrates the degradation as a result of crossflow. While the stagnation region heat transfer is degraded when crossflow is present, the overall heat transfer of the surface can be enhanced compared to what is observed when crossflow is not present.

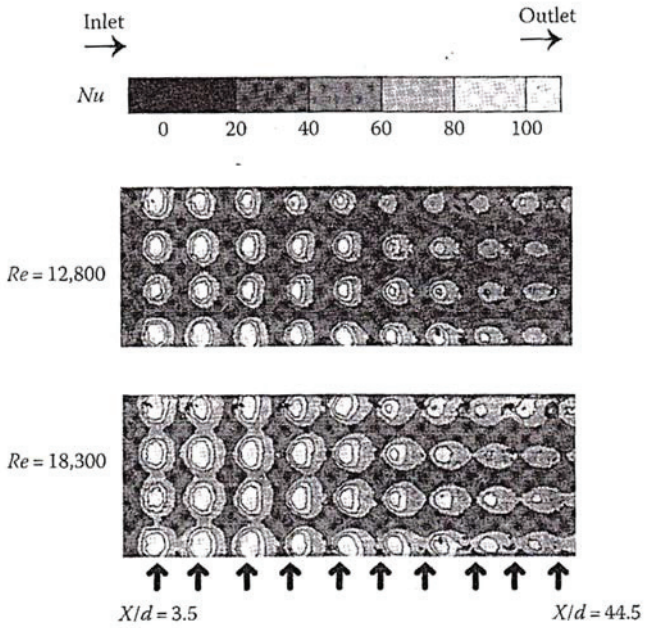

Figure 2.3: Heat transfer degradation as a result of crossflow [11]

Several studies have been performed to examine the effect of crossflow on jet impingement heat transfer. Kercher and Tabakoff [12] showed that an increase in jet-to-target surface spacing allows for the spent air to be diffused and reduces the effect of crossflow. Any benefits from reduced crossflow may be washed out as the increasing jet-

to-target surface spacing has been shown to reduce heat transfer. Ekkad et al. [13] performed a study on a staggered impingement array on a flat plate with film cooling ejection. It was shown that by removing the spent cooling air through these film cooling ejection holes, the effect of crossflow was weakened. While removing the crossflow effect also reduced the overall heat transfer within the impingement cavity, perhaps this loss can be overcome with the additional protection afforded by the film cooling on the exterior of the airfoil.

Curved Surface Impingement

Impingement is also widely used in the leading edge of turbine airfoils. In this region the target surface typically has a relatively small radius of curvature, and because of this, flat plate impingement does not provide a good model of the heat transfer characteristics. In 1969, Chupp et al. [14] pioneered the way for leading edge impingement by performing a parametric study in which flow conditions (Reynolds number) and geometric characteristics such as jet-to-target surface spacing, relative target surface curvature, and jet-to-jet spacing were considered. Platinum strip heaters were used to obtained regional heat transfer coefficients on a concave target surface. The experimental setup used by Chupp et al. [14] is shown in Figure 2.4. Chupp et al. [14], was then able to develop correlations for determining the Nusselt number in the stagnation region of the curved target surface (Nu_{Stag}), as well as the overall surface averaged Nusselt number (Nu_{avg}). The correlations developed by Chupp et al. [14] are still used today by designers and researchers to benchmark new impingement designs. The correlations from Chupp et al. [14] demonstrate that the heat transfer on the target

surface increases as jet Reynolds number (Re_{jet}) increases, jet-to-jet spacing (s/d_{jet}) decreases, jet-to-target surface distance (z/d_{jet}) decreases, and as the ratio of the target surface diameter-to-jet diameter (D/d_{jet}) increases.

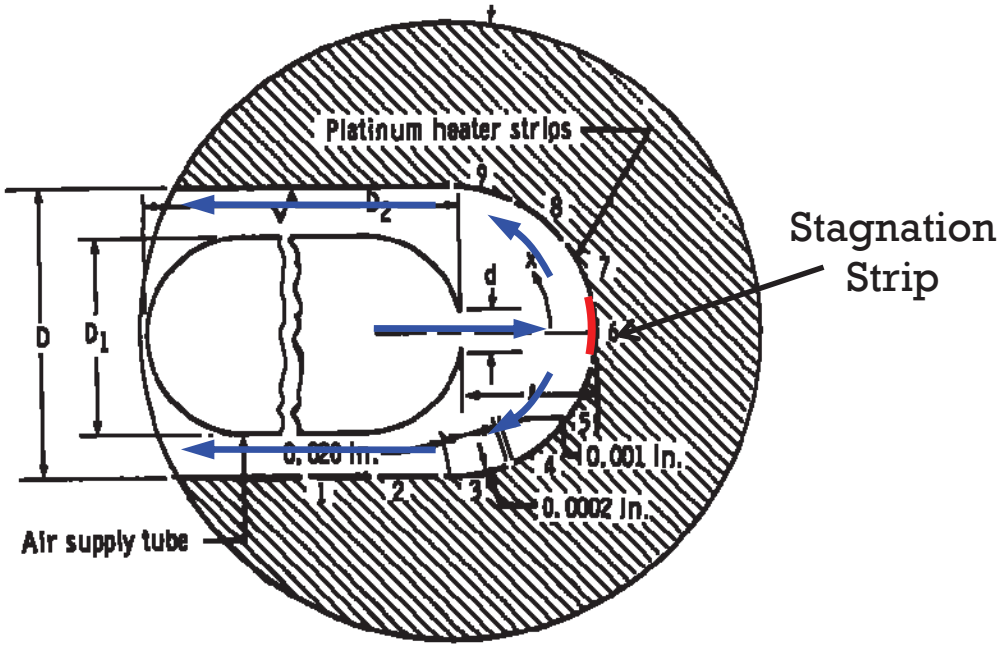

Figure 2.4: Experimental apparatus, with flow lines, used by Chupp et al. [14]

Effect of Varying Reynolds Number

While it is generally accepted that the Nusselt number increases with increasing Reynolds number, the extent to which these Nusselt numbers increase can differ significantly, depending on whether the flow is laminar or turbulent. Looking at the Chupp et al. [14] correlation for stagnation region heat transfer (Equation 2.1), one sees that the expected Nusselt number is proportional to the Reynolds number raised to the 0.7 power.

$$Nu_{Stag} = 0.44 \cdot Re_{jet}^{0.7} \left(\frac{d_{jet}}{s}\right)^{0.8} \exp\left[-0.85\left(\frac{z}{d_{jet}}\right)\left(\frac{d_{jet}}{s}\right)\left(\frac{d_{jet}}{D}\right)^{0.4}\right] \qquad (2.1)$$

$$Nu_{avg} = 0.63 \cdot Re_{jet}^{0.7} \left(\frac{d_{jet}}{s}\right)^{0.5} \cdot \left(\frac{d_{jet}}{D}\right)^{0.6} \exp\left[-1.27 \cdot \left(\frac{z}{d_{jet}}\right)\left(\frac{d_{jet}}{s}\right)^{0.5}\left(\frac{d_{jet}}{D}\right)^{1.2}\right] \quad (2.2)$$

According to Jordan et al. [4], turbulent flow theory suggests that this exponent should range from 0.7 to 0.8, whereas, for laminar flows the Nusselt number is proportional to the Reynolds number to the 0.5 power. Because of this discrepancy, the jet-to-target surface spacing becomes extremely important. Lee et al. [15] developed a Nusselt number correlation for the stagnation region of a curved surface and showed that the Reynolds number exponent varied depending on whether jet-to-target surface spacing allows for the existence of a potential core when striking the target surface. For smaller jet-to-target ($2 \leq z/d_{jet} \leq 6$) surface spacing, the potential core remains intact through impingement. The flow within the potential core is inviscid, and therefore, can be considered laminar. This results in Reynolds number exponents that more closely resemble that of laminar flow. When the jet-to-target surface length is sufficiently long to allow the potential core to diminish, increased Reynolds number exponents are observed.

Jet-to-Target Surface Spacing

There seems to be a disagreement in regard to the effect of jet-to-target surface spacing in open literature. The correlation developed by Chupp et al. [14] indicates that the average stagnation region Nusselt number continues to increase as the jet is moved closer to the target surface. However, the correlation developed by Chupp et al. [14] may provide a simplistic understanding of the z/d_{jet} trend. The effect of the jet-to-target surface spacing is multifaceted. Metzger et al. [16] and Fenot et al. [17] both observed,

from an average heat transfer perspective, that it is beneficial to have the potential core impinge on the target surface. However, other researchers, Lee et al. [15] observed that the highest stagnation heat transfer occurred when the jet-to-target surface spacing was just beyond the potential core. Similarly, Metzger et al. [16] showed that the maximum Nusselt numbers are encountered within a single diameter of the jet exit, and that as the jet is moved further away from the target surface, the Nusselt numbers decrease.

Contrary to the findings of Chupp et al. [14] and Metzger et al. [16], Lee et al. [15], showed that a maximum Nusselt number is observed at approximately six jet diameters from the target surface, and decreasing the jet-to-target surface spacing further does not significantly affect the surface heat transfer. The findings of Martin et al. [18] were similar, in that there were minimal changes to the Nusselt numbers observed at jet-to-target surface distances of less than $z/d_{jet} = 4$. Recall that at jet-to-target surface distances of less than approximately five, the potential core of the jet is still intact. Because of this, the velocity of the jet changes only marginally with a decreased jet-to-target surface spacing, and as a result, the heat transfer observed on the target surface does not change. However, once the jet-to-target surface distance exceeded $z/d_{jet} = \sim 5$, the stagnation region Nusselt numbers begin to decrease rapidly.

Jet-to-Jet Spacing

It is generally accepted that decreasing the jet-to-jet spacing will result in higher overall heat transfer on the target surface, and the correlation developed by Chupp et al. [14] agrees with this for $4 \leq s/d_{jet} \leq 16$. The increase observed in the overall surface heat transfer is typically attributed to the increased mass flow of cooling air within the

impingement cavity, due to having more jets cooling the same surface area. However, having jets packed close together allows engine designers to take full advantage of the three dimensional mixing as a result of the jet-to-jet interaction. In general, adjacent jets are thought to have a meaningful interaction when placed within eight diameters of one another. Contrary to this, Tabakoff and Clevenger [19] performed a study where the highest surface heat transfer occurred for a jet-to-jet spacing of $s/d_{jet} = 8.8$ with an impingement distance of $z/d_{jet} = 1$. While this may seem to contradict earlier findings, it was determined that the small jet-to-target surface spacing did not allow for the spent air to be removed from the channel, thus resulting in decreased heat transfer for the lower jet-to-jet spacing. These findings were confirmed by Metzger et al. [16] when investigating single row of impinging jets. For their experiment, both the jet-to-jet spacing and the jet-to-target surface spacing were varied. It was again shown that the highest heat transfer was observed for a large jet-to-jet spacing and $z/d_{jet} = 1$. Typically, jet-to-jet interaction can increase the surface heat transfer by providing additional mixing within the impingement cavity, however, because the jet-to-target surface spacing was so small for these studies, the spent air had little room to escape without disturbing the jet flow. Therefore, higher heat transfer coefficients were observed at large jet-to-jet spacings that provided sufficient room for spent air to escape.

Based on the studies mentioned above, it would stand to reason that spent air extraction would play a significant role in the heat transfer trends for varied jet-to-jet spacing. Many recent blade designs incorporate complex film cooling schemes through the mid-chord region and on the leading edge. This is typically referred to as "showerhead film cooling", due to the large amount of cooling holes littering the exterior

surface of the blade. Once the cooling air has been used for impingement on the interior of the blade, it is passed through these film cooling holes and used to form an insulating layer of cool air on the outer surface of the airfoil. As mentioned previously, the accumulation of spent impingement air within the channel can hinder cooling performance by inducing destructive crossflow effects. By removing the spent cooling air, these destructive effects are minimized thus resulting in better heat transfer characteristics. Metzger and Bunker [20, 21] studied the effect of jet impingement on a curved surface with and without film coolant extraction. The researchers observed that the presence of film coolant extraction yielded higher spanwise average Nusselt numbers than that afforded by the baseline case with no film cooling. It was also shown that the position of the extraction holes relative to the impinging jets can also affect the rate of heat transfer experienced. The maximum heat transfer occurred when the film coolant extraction holes were aligned with the impinging jets.

Jet-to-Target Surface Curvature

Recall that, according to the correlation developed by Chupp et al. [14], the heat transfer observed on a curved surface will increase as the curvature of the surface decreases. That is as the ratio of the surface diameter of curvature (D) to the jet diameter (d_{jet}) increases and the surface becomes more and more like a flat plate. Bunker and Metzger [20, 21] performed a study investigating leading edge sharpness. Using a single row of equally spaced, circular jets, cooling air impinged on a curved target surface. The diameter of curvature of the target surface was held constant while the jet-to-target spacing was changed, as shown in Figure 2.5. From this experiment, it was shown that a

sharper leading edge provided decreased Nusselt numbers at the stagnation point while at the same time providing a secondary area of increased heat transfer on either side of the stagnation region. This secondary area of increased heat transfer was a result of the flow accelerating out of the sharp leading edge. The sharper leading edge model produced a more uniform Nusselt number distribution resulting in lower thermal stresses on the target surface. It is thought that in such cases of sharp curvature, pockets of coolant become trapped in the apex of the channel preventing the jet from stagnating fully on the surface. Unfortunately, the sharpness effect cannot be fully captured from this study. As the curvature of the surfaces was altered case to case, so was the jet-to-target surface distance (z/d_{jet}). As mentioned previously, increasing this z/d_{jet} distance also results in decreased heat transfer on the target surface.

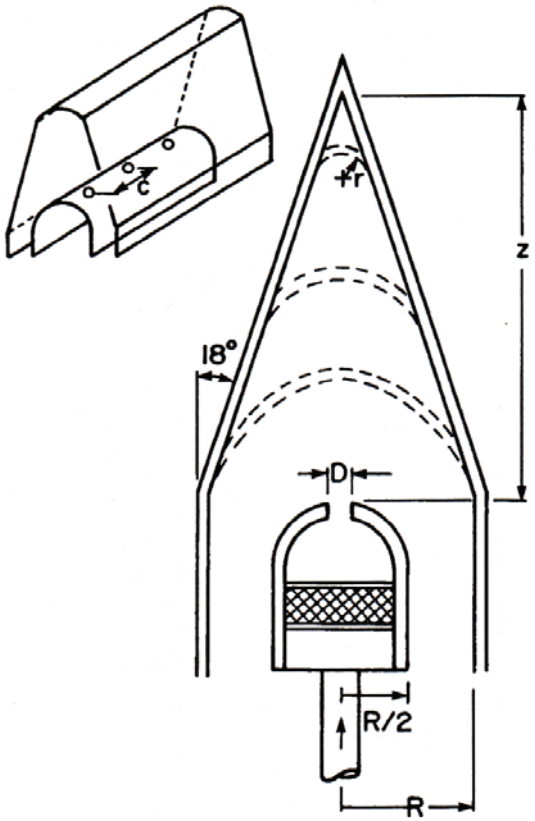

Figure 2.5: Experimental setup investigating leading edge sharpness [20]

Hrycak [22] also investigated the effect of target surface curvature on impingement heat transfer. It was shown that increasing the curvature of the target surface increased the surface average Nusselt number. Additionally, it was shown that the effect of curvature was more significant at lower Reynolds numbers. Fenot et al. [23] showed that as relative curvature increases (diameter of the surface decreases) there is a marginal increase in Nusselt number in the impingement region. Increasing this curvature however, produces a confinement of the jet's flow that results in a decrease in the surface averaged Nusselt number. Expanding on this, Cornaro et al. [24] performed a flow visualization study to determine the effect of target surface curvature on the length of the potential core. It was shown that impinging on a curved surface the potential core of the jet breaks down sooner than with flat plate impingement due to additional entrainment of outside air.

Jet Orifice Shape

Most of the earlier studies regarding jet impingement heat transfer focus on the cooling performance afforded by discrete circular jet orifices. In an effort to further improve the cooling schemes within the passages of these blades, researchers and designers began investigating other orifice shapes. One shape of particular interest is that of a continuous slot jet. A continuous slot jet would provide fairly uniform heat transfer in the streamwise direction and limit the potential for large temperature gradients. Though this does come at a cost, as such a jet shape could compromise the integrity of the blade itself, and provide lower rates of heat transfer. Gau and Chung [25], Choi et al. [26], and Yang et al. [27] all investigated the use of slot jets on a curved surface.

However, in addition to the previously mentioned drawbacks of a slot jet, in order to match the heat transfer performance of a discrete jet, a slot jet would require significantly more coolant air. As mentioned previously, heat transfer increases as jet-to-jet spacing decreases. However, this trend only holds for discrete jets. Once the jet-to-jet spacing becomes so small that there is a continuous jet, the cooling performance suffers. This is explained by the lack of three dimensional mixing characteristics afforded by individual jets interacting with one another. Several researchers [19, 20] have shown the advantages of using discrete jets over a continuous slot jet. Born out of this, researchers began investigating elongated discrete jets hoping to capture some of the benefits of the continuous slot while maintaining the complex flow interactions of discrete circular jets. Gulati et al. [28] performed a study to determine the effect of square and rectangular shaped jets at matching Reynolds numbers (i.e. the mass flow rate will vary slightly between shapes). It was determined that the elongated shape of the rectangular jet increases the turbulence intensity, thus increasing heat transfer on the target surface. Additionally, the rectangular shaped jet provided a larger stagnation region compared to round and square jets. Lee and Lee [29] investigated the performance of an elongated ellipse with varying aspect ratios. It was shown that the magnitude of the Nusselt number was highly dependent on the aspect ratio of the jet and the jet-to-target surface spacing. Compared to a circular jet, the ellipse shaped orifices provided increased turbulence intensity at the exit, resulting in increased heat transfer. An elongated "racetrack" shaped jet has been of particular interest in recent years. In general these racetrack shaped jets offer higher heat transfer than their cylindrical counterparts, at an equivalent mass flow rate [5, 30-31]. Jordan et al. [6] also examined the effect of various supply conditions

with racetrack shaped jets, and based on his results, racetrack jets were again shown to outperform cylindrical jets at an equivalent mass flow rate. Taslim et al. [30-32] has considered the effect of impingement jet shape (cylindrical and racetrack), target surface roughness, varying supply conditions, and film cooling extraction. It was shown that heat transfer enhancement occurs with the use of a racetrack shaped jet, roughened target surface, and film cooling extraction.

Jet Edge Condition

In addition to varying the shape of the jet in an attempt to optimize cooling performance, much work has been done investigating the effect of jet edge condition. A square edge jet has a sharp corner at the inlet and exit of the jet orifice, and is typically modeled in impingement literature; however, due to manufacturing limitations, a perfectly square edge jet cannot be produced. Therefore, researchers began to examine the effects of jets with varying degrees of filleting around the entrance and exit of the orifice. A square edge orifice produces a jet with relatively high turbulence intensity, and consequently high surface heat transfer. However, by using a gradual inlet or exit to the jet orifice, the flow characteristics can be altered dramatically yielding significantly different heat transfer trends. For a square edged jet orifice, as cooling fluid enters the orifice, a vena contracta effect begins to form on the walls of the jet. This phenomenon is a result of separation along the edges of the orifice which forces the fluid through a smaller effective cross sectional area. This confinement produces higher jet velocities (which will offer higher heat transfer), but at a cost of an increased pressure drop through the orifice. An illustration of the vena contracta effect is shown in Figure 2.6.

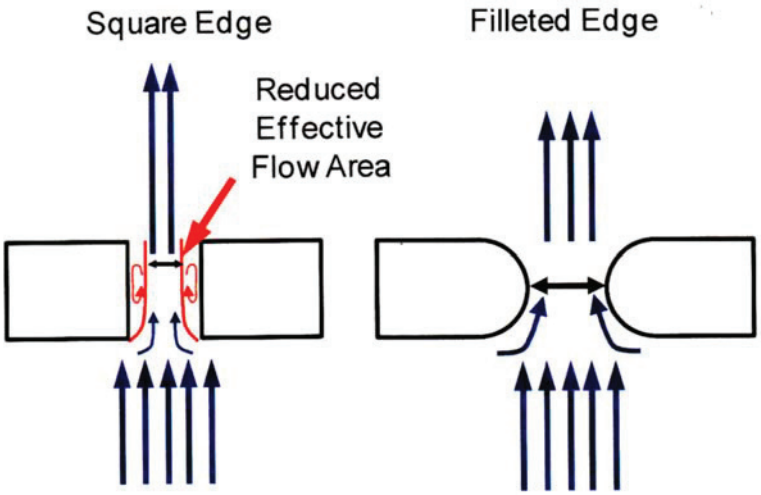

Figure 2.6: Vena contracta effect with varying edge conditions [4]

To combat this, researchers have investigated the use of gradual orifice inlets. Brigoni and Garimella [33] examined the performance of impinging jets with varying degrees of chamfering on the inlet side. Through this study it was shown that a narrow chamfer minimized the vena contracta effect through the orifice, thus reducing the pressure drop. On the other hand, the jet velocity decreases along with the turbulence intensity of the jet, resulting in decreased heat transfer. Additionally, researchers have investigated the effect of varying degrees of filleting on an orifice. More recently, Jordan et al. [4-7] used a transient TLC technique to obtain detailed Nusselt number distributions on a concave impingement surface using circular and racetrack shaped jets with various filleting. The orifices were all examined at a constant jet-to-target surface spacing (z/d_{jet} = 4), surface curvature (D/d_{jet} = 5.33), and jet-to-jet spacing (s/d_{jet} = 8). The Reynolds number was varied along with the inlet supply condition. Jordan et al. [4-7] showed that the racetrack shaped jet outperformed the circular jet consistently (at an equivalent mass

flow rate). The square edge orifices offered the highest level of heat transfer in the stagnation region, but also sustained the highest pressure drop across the jet plate.

Other Impingement Considerations

Most leading edge impingement schemes model an evenly distributed flow throughout the impingement array. However, design limitations within the engine may dictate otherwise. Often times, excess air is bled from the impingement supply channel to be used for tip cap cooling, resulting in a skewed distribution of coolant to the impingement array. Through the use of radial bypass flow, Jordan et al. [7] captured the effect of large inlet crossflow velocities in an impingement channel. It was shown that these large inlet crossflow velocities have destructive effects on the target surface heat transfer enhancement. This is because the cooling fluid carries some of the streamwise momentum from the supply channel into the impingement channel, and results in deflecting of the impinging jet.

Other flow effects such as the impinging jet temperature have also been studied. In the 2008 study by Fenot et al. [23] the heat transfer afforded by a round impinging jet with varying jet injection temperatures (temperature differential of up to 38°C) was investigated, and showed that the resulting surface Nusselt number distribution was independent of the changing jet temperature. Martin et al. [34] investigated the effect of high jet temperature (temperature differentials up to 222°C) on impingement heat transfer. It was again shown that target surface Nusselt numbers, unlike heat transfer coefficients, do not depend on the jet temperature.

Rotating Flows

With the addition of rotation, rotational Coriolis and buoyancy forces act on the flow. It has been well documented how these forces effect both the velocity and temperature distributions within rotating channels. Early work on rotational effects was performed by Wagner et al. [35] in 1991, when radially outward flow in a smooth, rotating channel was investigated. From the experiment, they showed that for radially outward flow, heat transfer is enhanced on the trailing side of the passage (pressure side), and degraded on the leading surface (suction side). This phenomenon is due to the fact that, for radially outward flow, the buoyancy and Coriolis forces are working together. This joint effort results in the effects of these forces compounding with one another to dramatically increase or decrease heat transfer on the trailing and leading surfaces of the channel, respectively. On the trailing wall, the boundary layers become very thin allowing for high heat transfer between the surface and the cooling fluid. The opposite is true for the leading wall where the boundary layer is thick. Expanding on this study, Wagner et al. [36] investigated the effect of rotation on flow through a serpentine passage, so that the effect of radially inward flow could be considered. The trend observed for radially inward flow was opposite of that for radially outward flow. Heat transfer is enhanced on the leading side of the passage and degraded on the trailing surface due to the reversal of the Coriolis force. The magnitude of the enhancement seen for radially inward flow is less than that for radially outward flow, due to the fact that now, instead of the Coriolis and buoyancy forces assisting one another they now oppose one another. A conceptual view of rotation induced secondary flow patterns is shown in Figure 2.7.

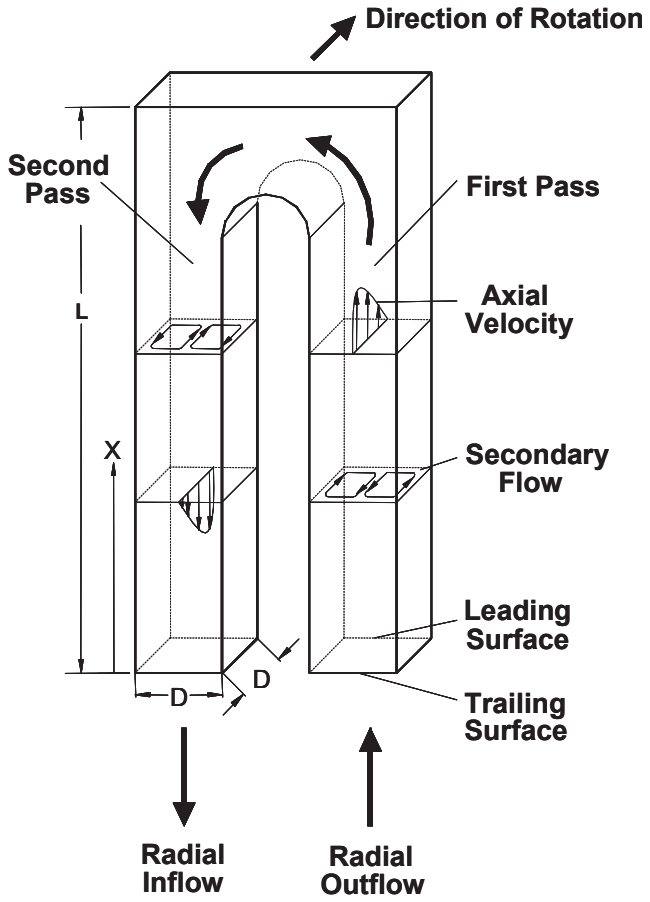

Figure 2.7: Visualization for rotating channel flow [1]

Researchers have also experimentally investigated the effects of rotation combined with surface roughness features, varying channel shape with different aspect ratios, as well as channel orientation with respect to the direction of rotation [37-52]. The addition of surface roughness features, such as ribs, to a rotating channel can either enhance or degrade surface heat transfer depending on how secondary flows induced by these surface features interact with the rotation induced flows. The degree of this interaction is highly dependent on the orientation of the ribs. Additionally, the shape of the channel greatly influences the size and strength of the rotation induced vortices, and effects can be either constructive or destructive. Furthermore, as the channel orientation deviates from 90°, heat transfer enhancement can be altered significantly.

In recent years, studies performed on rotating channel heat transfer have been expanded to consider rotation and buoyancy numbers that more closely model realistic conditions found in production engines. Employing the scalable non-dimensional rotating and buoyancy parameters (defined in Equations 5.1 and 5.2) has proven to be a useful tool in closely modeling these realistic conditions. These studies that have focused on high rotation numbers (exceeding 0.40) [46-52] have been successful in showing that there exists a critical rotation number, that once reached, enhances heat transfer on all surfaces. This critical value tends to vary by experiment due to differences in channel shape, and the presence of surface roughness features (ribs). For radially outward flow, at rotation numbers less than this critical value, heat transfer enhancement is focused on the trailing wall. However, once this critical rotation number is breached, enhancement can be observed on all walls of the channel, due to the increased rotation induced mixing.

Combining the effect of rotation with jet impingement has not been as thoroughly investigated as its individual parts. Parsons et al. [53-56] and Akella and Han [57, 58] performed a series of experiments through which they were able to identify the effect of rotation on flat plate impingement with crossflow. It was shown that with the addition of rotation (rotation numbers ranging 0 - 0.003 for Parsons et al. [53-56] and 0 - 0.013 for Akella and Han [57, 58]), the impinging jet would begin to deflect thus decreasing the heat transfer on the target surface (on both the leading and trailing side) relative to the stationary case. Note that the non-dimensional rotating parameter is much smaller for impingement studies due to the fact that the characteristic length used is the hydraulic diameter of the jet rather than that of the channel. More recently, in 2011, Lamont and Ekkad [59] performed a rotating study on flat plate impingement using a transient liquid

crystal technique (TLC) to obtain detailed Nusselt number distributions on the impingement surface. The non-dimensional rotating parameter varied from 0-0.0022. The experiments were performed in a rotating setup with radially outward flow, and the trends observed were consistent with radially outward channel flow under rotation. That is heat transfer is enhanced on the trailing (pressure) surface, and degraded on the leading (suction) surface.

In 2012, Elston and Wright [8] completed a study investigating the effect of rotation on leading edge impingement on a curved target surface under high rotation numbers (Ro = 0 - 0.13). The results published for the supply side of the channel (radially outward flow) supported findings by earlier researchers (increased heat transfer on the trailing side, and decreased heat transfer on the leading side). Moving to the impingement cavity (radially inward crossflow), it was shown that as rotation increased, the flow favored the leading side, and thus heat transfer was enhanced on the leading surface. At the highest rotation numbers investigated, enhancement of approximately 2.3 times the stationary value in that region was observed. This highest enhancement occurred at the impingement location near the blade tip, and diminished quickly as the crossflow developed (flowing radially inward).

Based on this review, it is clear that little work has been performed to examine the effects of varying jet geometries in the leading edge of turbine blades. In an effort to fully identify the heat transfer characteristics associated with leading edge impingement flow and varying jet geometry, this investigation employs shaped jets with varying geometric parameters, and varying inlet supply flow conditions. Circular and racetrack shaped jets with square edges, and edges with various degrees of filleting are used to further

understand the effects on the heat transfer coefficients in the leading edge. Additionally, even fewer studies exist on the subject of rotating impingement flows. This study also investigated the effect of high rotation numbers on impingement heat transfer. A circular and racetrack jet were examined to determine if one provided enhanced heat transfer capabilities over the other. Both studies were conducted using a classic, steady state heat transfer technique to obtain regionally averaged heat transfer coefficients on the curved target surface. An overview of this technique is provided in the following chapter.

CHAPTER THREE

Steady State Copper Plate Technique

This chapter discusses the general theory behind a traditional steady state copper plate heat transfer test. Within the gas turbine research community exist numerous heat transfer problems. The vast majority of these problems center around the interactions between the hot fluids exiting the combustor and the physical parts within the engine that these hot gases must navigate before exiting as exhaust. Convection is the mode of heat transfer responsible for a significant portion of the overall heat transfer for these interactions. Convection on its most basic level is simply the transfer of internal energy into or out of an object by the movement of surrounding fluid. Newton's law of cooling describes this fundamental interaction between the relatively cool components of an engine, and the extremely hot mainstream gases:

$$\dot{Q} = h \cdot A_s \cdot \left(T_\infty - T_w\right) \tag{3.1}$$

where $\dot{Q}$ is the rate of heat transfer, h is the convective heat transfer coefficient, T_∞ is the bulk temperature of them mainstream fluid, and T_w is the wall temperature of the component. The above equation describes the interaction between the hot gases in the engine and the external surfaces of the components; however, this experiment focuses on the exchange of energy between the coolant fluid and the interior wall of the components. Therefore, the temperature difference for this experiment will be taken to be $T_w - T_c$.

Steady state experimental techniques are considered to be the most elementary and intuitive to execute. These methods have withstood the test of time, and are often still preferred over more sophisticated methods, because of their simplicity. In the simplest of terms, a steady state test consists of heating a surface and simultaneously cooling the surface until an equilibrium, or "steady", state is reached. Once this occurs, the temperatures of the surface and the fluid are measured, as well as the power supplied to the surface heater. With this information, the heat transfer coefficient of the system can be obtained. For both experiments discussed in this thesis, a steady state copper plate technique is utilized to obtain regionally averaged heat transfer coefficients.

Like most experimental methods, steady state techniques are not perfect. Due to the nature of these tests, it is common for a single experiment to last for two or three hours at a time. When applying Equation 3.1 it is assumed that one is only transferring heat away from the surface area that is exposed to the cooling fluid. However, this is not the case, as it is impossible to perfectly insulate the backside of the support material that contains the target surface. When conducting such a long experiment, heat has ample time to be conducted through this support material and convected away on the back side. This is commonly referred to as heat loss. In an effort to minimize the heat loss, the back side of the support material is well insulated. Furthermore, to account for the error in the experimental results incurred by the heat loss component, a heat loss calibration was devised.

To perform a heat loss calibration, the apparatus' test section will be filled with a low conductivity insulation. In the case of the two experiments outlined in this thesis, fiberglass insulation was utilized. The purpose of the insulation is to entice the heat

within the surface to conduct backwards, through the support material, rather than into the flow cavity. Once insulated, two data sets will be collected: one at a temperature below that which the actual experimentation will be conducted, and one at a temperature above what is expected during the actual experiment. Additionally, the room temperature at each of the high and low heat loss tests is collected (the room temperature serves as the second temperature for the temperature difference in the heat transfer calculation), as well as, the power input into each surface. By taking heat loss data at a temperature above and below the expected surface temperature, the experimentalist can linearly interpolate between these points to determine the expected heat lost during experimentation by using Equation 3.2:

$$\dot{Q}_{loss} = \frac{\dot{Q}_{high} - \dot{Q}_{low}}{\left(T_{high} - T_{room,high}\right) - \left(T_{low} - T_{room,low}\right)} \cdot \left[\left(T_w - T_{room}\right) - \left(T_{low} - T_{room,low}\right)\right] + \dot{Q}_{low} \quad (3.2)$$

where $\dot{Q}_{loss}$ is the approximated heat loss, $\dot{Q}_{high}$ is the power into the system for the high temperature heat loss case, $\dot{Q}_{low}$ is the power into the system for the low temperature heat loss case, T_{high} is the temperature of the surface for the high temperature heat loss case, T_{low} is the temperature of the surface for the low temperature heat loss case, $T_{room,high}$ is the room temperature for the high temperature heat loss case, $T_{room,low}$ is the room temperature for the low temperature heat loss case, T_w is the surface temperature during experimentation, and T_{room} is the room temperature during experimentation. Once the heat loss approximation is known, the net rate of heat transfer for a specific case can be determined using Equation 3.3:

$$\dot{Q}_{net} = \dot{Q} - \dot{Q}_{loss} \quad (3.3)$$

where $\dot{Q}_{net}$ is simply the difference in the input power for the test case and the expected heat loss. $\dot{Q}_{net}$ represents the amount of heat being convected away from the target surface by the cooling air.

Finally, by rearranging equation 3.1 and substituting in the net power term, the heat transfer coefficient can be calculated directly using Equation 3.4.

$$h = \frac{\dot{Q}_{net}}{A_s \cdot (T_w - T_c)} \tag{3.4}$$

Further, the results that will be outlined later in this thesis will all be in the form of the non-dimensional heat transfer coefficient, the Nusselt number. The Nusselt number is simply a ratio of convective heat transfer to conductive heat transfer. By non-dimensionalizing the results, one-to-one comparisons to other works (Chupp et al. [14] correlation, previous work by Jordan et al. [4]) will be made easier. The Nusselt number is obtained by implementing the following equation:

$$Nu = \frac{h \cdot d_{jet}}{k_{air}} \tag{3.5}$$

where h is the calculated heat transfer coefficient, d_{jet} is the hydraulic diameter of the jet (characteristic length for impingement flow), and k_{air} is the thermal conductivity of air.

In each experiment, the impingement target surface is outfitted with an array of copper plates (aluminum in the case of the Honeywell Aerospace apparatus). A type T thermocouple has been imbedded into the back side of each of these plates in order to record the regional wall temperature (T_w). Because of the high thermal conductivity of the

metals used, it is assumed that there is no temperature gradient through each individual plate. This assumption was validated by spot checking some plates for temperature uniformity. Furthermore, each plate is isolated from the surrounding plates using a low thermal conductivity paste to discourage conduction between plates. The bulk fluid temperature (T_c) is taken to be the coolant temperature at the inlet of the jet. The exposed surface area (A_s) of the plates is known. The power into the plate is easily determined by measuring the resistance of the heater and the voltage.

$$\dot{Q}_{in} = \frac{V^2}{R} \tag{3.6}$$

For the rotating test section (outlined in detail in Chapter 5) each streamwise row of nine plates has a dedicated resistance heater. This results in a uniform heat flux across all nine of the plates for that heater, which allows for the easy calculation of the power in on a per plate basis. The Honeywell Aerospace apparatus utilizes a single heater for the entire surface, and it is assumed that all 133 plates receive a uniform heat flux.

Uncertainty analysis was performed on these two experiments using the traditional Kline and McClintock method [60]. For both studies, the heat loss parameter dominates the uncertainty. For the Honeywell investigation, the heat loss term was very small, due to the large amount of insulation on the backside of the test section. These small values provided an uncertainty in the Nusselt number calculation of approximately 1.5% with only a marginal change between the high and low Reynolds numbers. Compared to the rotating experiment where calculations yielded an uncertainty in the Nusselt number of 9.5% and 7.3% at the low and high Reynolds number, respectively.

This increase in uncertainty is due to the elevated heat loss associated with the forced convection on the outside of the rotating test section removing the heat at a faster rate.

CHAPTER FOUR

Honeywell Aerospace Experimental Facility

Overview of Experimental Facility

The Honeywell experimental impingement facility was designed to model the interior cooling passage in the leading edge of a typical turbine airfoil. In addition to standard impingement supply conditions, the apparatus has the ability to apply radial bypass effects on the supply side of the impinging jets. This is particularly important when modeling impingement flows for airfoils with large crossflow effects on the supply side of the orifice. The curved impingement target surface is outfitted with individual aluminum plates to allow for the collection of regionally averaged heat transfer coefficients by utilizing a classic, steady state heat transfer technique. The heat transfer trends observed throughout the semicircular channel can provide valuable insight to blade designers and allow for a more complete understanding of the complex flow characteristics with varying geometric jet parameters. An overview of the apparatus is shown in Figure 4.1.

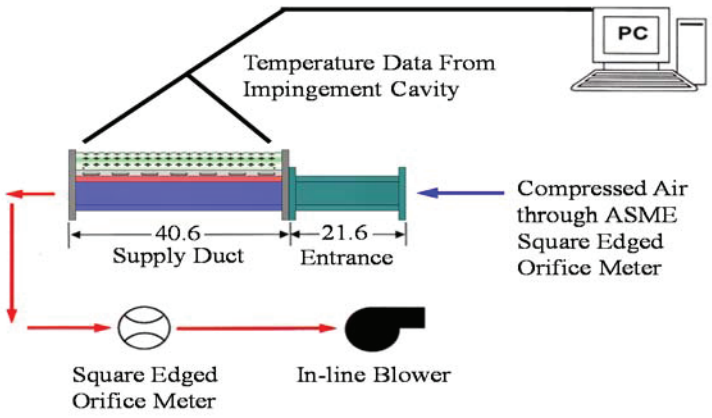

Figure 4.1: Overview of experimental apparatus.

The cooling air is provided by a large compressor, and the mass flow rate is measured using an ASME square edge orifice meter. Upstream of the orifice meter are a pressure regulator and three inline air driers to remove any unwanted moisture in the air supply. Once the cooling air has been used for impingement, it is exhausted into the room. In the case of radial bypass flow, cooling air is pulled from the supply duct prior to impinging and the bypass flow rate is controlled with a second ASME square edged orifice meter and an inline blower. An enlarged view of the test section is shown in Figure 4.2.

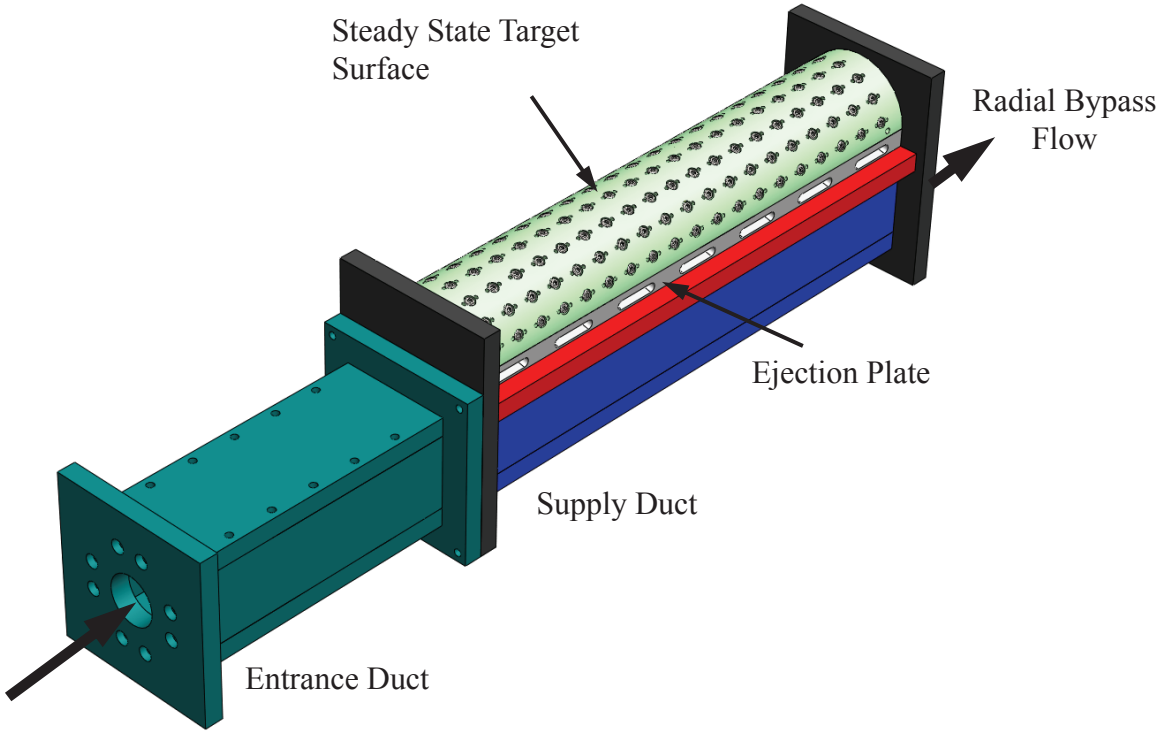

Figure 4.2: Overview of leading edge test section.

Flow Measurements

As mentioned previously, two ASME square edged orifice meters are utilized in this experiment. The first is located upstream of the test section and used to control the total mass flow of supply air entering test apparatus. A regulator is used to control the

pressure upstream of the first orifice plate, and is set to 100 psi. The second orifice meter is used to remove a portion of the impingement supply air to dictate a specific bypass ratio. Employing the Law of Conservation of Mass, a simple mass balance is all that is needed to determine the resultant mass being used for impingement. For cases with no radial bypass, a valve is closed downstream of the second orifice meter to prohibit any bypass flow.

A pressure differential is determined through the use of flange taps on each side of the orifice plate and a 5" Dwyer oil manometer provides the measurement of the pressure drop across the orifice. The total mass flow rate for the cooling air supply can be determined using Equation 4.1 produced by Leary and Tsai [61].

$$w = 0.1145 \cdot D_2^{\,2} \cdot K \cdot Y \cdot \sqrt{\left(\frac{P_1}{T_1}\right) \cdot G \cdot y \cdot \Delta P} \tag{4.1}$$

For the given equation: w is the mass flow rate of air into the system in pounds mass per second, D_2 is the diameter of the orifice plate in inches (1"), K is the discharge coefficient (0.62), Y is the expansion factor (0.98), P_1 is the upstream absolute static pressure in inches of mercury (203.6), T_1 is the temperature at the inlet of the orifice in degrees Rankine (530), G is the specific gravity of the air (0.0013), y is the supercompressability factor (1.0), and ΔP is the pressure drop across the orifice plate in inches of water. The upstream pressure is controlled using an inline regulator from the Wilkerson Corporation, and the upstream pressure readout is monitored using an Ashcroft dial gauge. The manometer can accommodate a maximum pressure differential of five inches and has a resolution of 0.01 inches for a pressure differential of one inch of water or less and 0.1 inches for pressure differential greater than one inch of water. Prior to testing, the

required mass flow rates to attain the desired Reynolds numbers are calculated using Equation 4.1. The impingement cases are run at a duct Reynolds numbers of 10,000, 20,000, and 30,000 for the supply. The duct Reynolds number is calculated using Equation 4.2:

$$\mathrm{Re}_{duct} = \frac{\rho \cdot V_{duct} \cdot d_{h,duct}}{\mu} \tag{4.2}$$

where ρ is the density of the air, V_{duct} is the inlet velocity of the supply flow, $d_{h,\,duct}$ is the hydraulic diameter of the channel, and μ is the dynamic viscosity of the air. The hydraulic diameter of the supply channel, $d_{h,\,duct}$, is defined as:

$$d_{h,duct} = \frac{4 \cdot A_C}{P_{duct}} \tag{4.3}$$

where A_C is the cross-sectional area of the duct, and P_{duct} is the perimeter of the duct.

It is also important to be able to determine the jet Reynolds number for each of the flow scenarios. To do this, the mass flow is assumed to be evenly distributed across the five jets. This assumption was validated by Jordan [4] in previous work using the same base setup. Based on this, the expression for the jet Reynolds number is given as:

$$\mathrm{Re}_{jet} = \left(\frac{1}{5}\right) \cdot \frac{4 \cdot w}{\mu \cdot P_{jet}} \tag{4.4}$$

where w is the total mass flow rate of air in pounds mass per second, μ is the dynamic viscosity of air, and P_{jet} is the perimeter of the jet opening. For cases involving radial bypass the same technique is used to determine what portion of the total mass flow rate should be bypassed. This is controlled using the second 1” orifice meter and measured on a 10” Dwyer manometer. The inline blower and a gate valve just upstream of the blower are used to fine tune the bypassed mass flow rate.

Test Section

The test section used in this study was modified from that used by Jordan et al. [4-7]. The clear target surface previously used for transient TLC measurements was replaced with a stready state target surface. All walls of the supply duct have been fabricated using 1.25 cm plexiglass. Figure 4.3 offers a detailed overview of the test section.

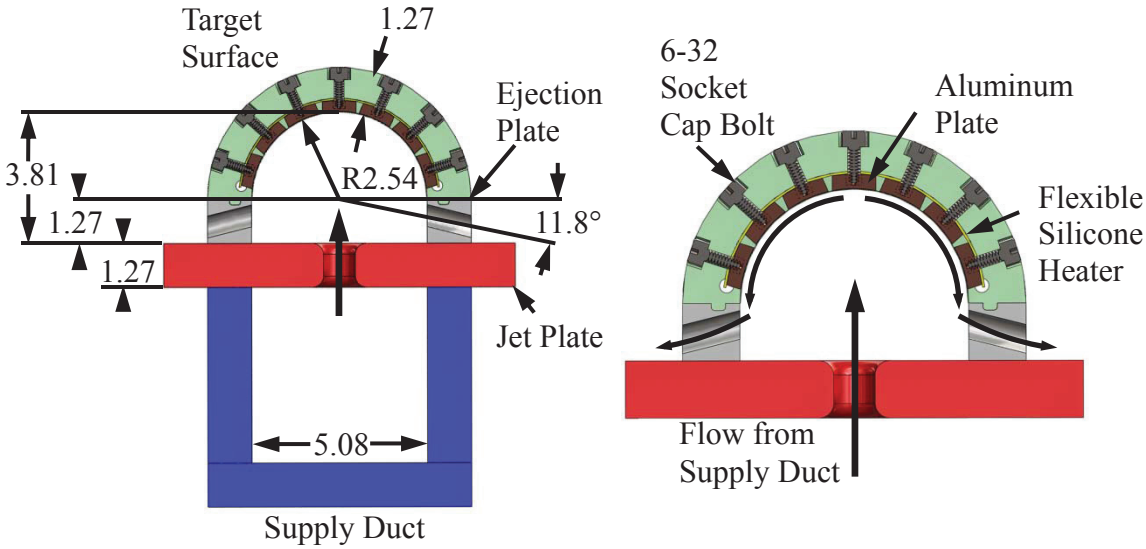

Figure 4.3: Cross-sectional view of leading edge test section (dimensions in cm).

From the first orifice flow meter, cooling air travels through a flexible one inch diameter tube and into the entry duct. The entry duct is a square channel with a width of 5.08 cm providing a flow area of 25.81 cm². This portion of the test section is intended to condition the inlet flow of air, but does not provide the necessary streamwise length to allow the supply flow to develop fully, which is consistent with the non-uniformity expected in actual turbine airfoils.

From the entry duct, cooling air enters the supply duct. The supply duct has the same dimensions and flow area as the entry duct; however, the jet plate makes up the top

wall of the supply channel. The jet plate has a row of five jets arranged in the streamwise direction. By changing the jet plate, the heat transfer characteristics of varying jet shapes with varying edge conditions can be easily investigated. In addition, the test section is capable of accommodating jet plates of varying thickness to isolate the effect of relative jet length. The end of the supply duct provides an exit for the radial bypass flow and just downstream is the second orifice meter used to control the mass flow rate of the radial bypass flow.

Upon entering the square supply duct, cooling air must turn 90° upward to pass though the jet orifice and into the impingement cavity. The impingement cavity consists of the curved target surface and spent air ejection slots on each side. The ejection slots are intended to remove any spent cooling air from the impingement cavity in order to minimize any crossflow effects. The curved target surface support material is made of Glass Filled Nylon 12 and was custom made using a selective laser sintering technique by Harvest Technologies. This serves as the support structure for the heater and individual aluminum plates through which the heat transfer is measured. The support material is designed to accommodate 19 aluminum plates in the streamwise direction, and 7 aluminum plates around the circumference. An overview of the aluminum plates is shown in Figure 4.4.

The plates are made from 6061 aluminum with a 2.54 cm inner radius. The plates are 0.3175 cm thick, 1.75 cm long, and the width spans an arc of 22.0°. This gives an impingement surface area of 0.264 square inches per plate. On the back side of each aluminum plate there are 3 holes. The center hole is tapped to accommodate a 6-32 bolt, and the other two holes are 1/16 inches in diameter and are used to mount a type T

thermocouple to the backside of the plate. A thin film heater was used to heat the back side of the individual aluminum plates.

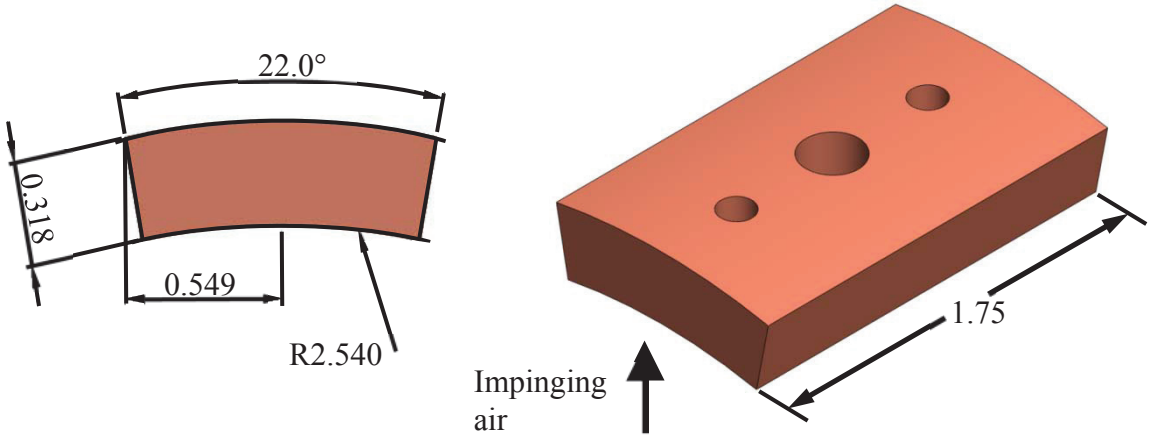

Figure 4.4: Detailed view of aluminum plate (dimensions in cm).

The heater was custom manufactured by AllFlex Inc. and was designed to incorporate the same hole pattern found on the backside of the aluminum plates. For this to work, a total of 399 through holes were placed in the heater. A layout of the heater is shown in Figure 4.5.

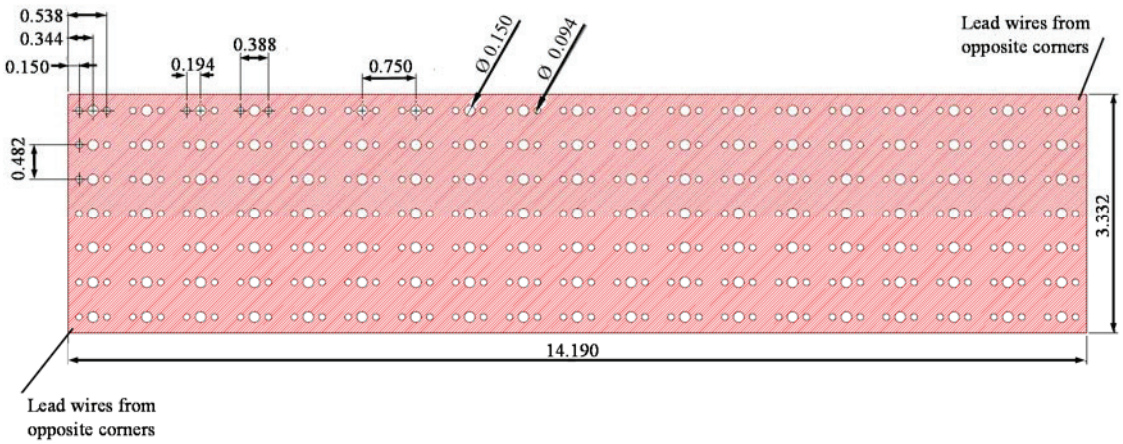

Figure 4.5: Hole layout for custom, flexible, silicone heater.

The heater, once installed was sandwiched between the support material and each aluminum plate. High conductivity thermal paste from Omega Engineering Inc. was used

to minimize any contact resistance between the backs of the aluminum plates and the heater. A 6-32 socket cap bolt passes through the back of the support material, the heater, and into the back of each aluminum plate to hold it snugly in place. Once every aluminum plate is in place there is a small gap between each one so that the local heat transfer can be isolated. In order to provide as smooth of a target surface as possible, and to insulate each aluminum plate, low conductivity silicone paste is used to fill this void. After the silicone paste has cured, the target surface is sanded smooth.

For this experiment, it was crucial that there not be a temperature gradient through the aluminum plate at each location. Typically, for a steady state test such as this, a surface material such as copper would be chosen for its very high thermal conductivity properties. Due to the low availability and high cost of raw copper materials, aluminum was chosen instead. It was then necessary to calculate the Biot number of the aluminum masses, using Equation 4.5, at the expected extremes of the heat transfer test.

$$Bi = \frac{h \cdot L_c}{k_{Al}} \tag{4.5}$$

In this equation, h is the expected rate of heat transfer, L_c is the characteristic length of the mass (defined as the ratio of volume to exposed surface area), and k_{Al} is the thermal conductivity of aluminum. For both the high and low expected rates of heat transfer, the Biot number was well below 0.1 indicating that there should be no significant temperature gradient through the aluminum mass. Despite this, select aluminum plates were instrumented with 2 thermocouples (one in each hole), while others contain only one thermocouple. This was done in an effort to spot check the plates to ensure a uniform temperature throughout. Figure 4.6 highlights which locations on the test section were instrumented with two thermocouples in a single plate. It is worth noting that for all

locations sampled, there were none that had a temperature difference outside that of the uncertainty of the thermocouple.

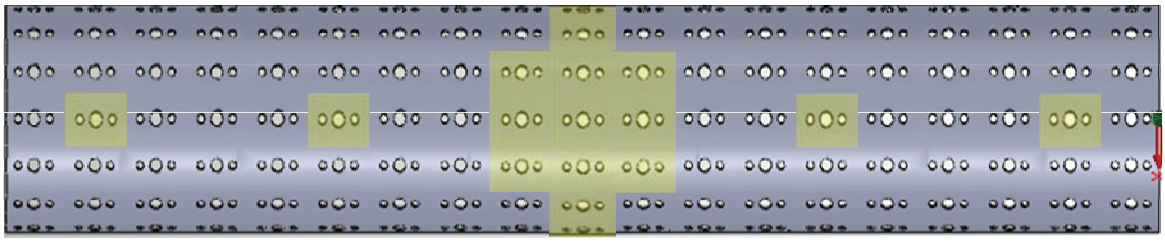

Figure 4.6: Locations containing two thermocouples.

During testing, the mass flow rate of coolant into the test section is varied to achieve the desired jet Reynolds numbers. Additionally, the inlet crossflow effect can be varied by altering the inlet mass flow rate of air as well as the mass flow rate of radial bypass flow out of the supply channel. Duct Reynolds numbers of 10,000, 20,000, and 30,000 are used for the initial supply of coolant. Two jet orifice shapes are investigated in this experiment: circular and racetrack. Each jet shape has unique jet Reynolds numbers corresponding to these supply conditions due to a variation in cross-sectional area through the jet. Even with this variation in flow area, the hydraulic diameter is the same for the two jet shapes at $d_{jet} = 0.953$ cm. For a circular jet, the corresponding jet Reynolds numbers are 14,000, 28,100, and 42,100 respectively. For a racetrack shaped jet, the jet Reynolds numbers are 11,800, 23,600, and 35,400. In the case of radial bypass flow, the inlet supply duct Reynolds number is maintained at 30,000, and coolant is bypassed to obtain the two lower jet Reynolds numbers of 14,000 and 28,100 for a circular jet (11,800 and 23,600 for a racetrack shaped jet). An outline of the tests conducted is presented in Table 4.1.

Table 4.1: Test cases for jet impingement for a circular and racetrack shaped jet

Re_{Duct}	$\frac{\dot{m}_{impinge}}{\dot{m}_{supply}}$	$\frac{R_{Fillet}}{t}$	$\frac{s}{d_{Jet}}$	$\frac{t}{d_{Jet}}$
10000	1	0, 0167, 0.188, 0.267, 0.500	8	1.33, 2.50, 4.00
20000	1	0, 0167, 0.188, 0.267, 0.500	8	1.33, 2.50, 4.00
30000	1	0, 0167, 0.188, 0.267, 0.500	8	1.33, 2.50, 4.00
30000	0.33	0, 0167, 0.188, 0.267, 0.500	8	1.33, 2.50, 4.00
30000	0.67	0, 0167, 0.188, 0.267, 0.500	8	1.33, 2.50, 4.00
10000	1	0, 0.500	4	1.33
20000	1	0, 0.500	4	1.33
30000	1	0, 0.500	4	1.33
30000	0.33	0, 0.500	4	1.33
30000	0.67	0, 0.500	4	1.33

Jet Geometries

As mentioned previously, two different jet shapes will be investigated for this experiment, a traditional cylindrical jet and a racetrack shaped jet. An outline of the varying jet geometries is shown in Figures 4.7 and 4.8. For each jet shape, a varying degree of relative radius (R_{fillet}/t) will be examined. The values for this parameter will range from 0, for a square edge orifice, up to a relative radius of 0.5 for a fully filleted orifice. Historically, most impingement studies have concerned themselves with only square edged orifices. However, these features are impossible to manufacture using modern casting techniques. Instead of a square edge jet, designers are left with a jet with some degree of filleting around the entrance and exit. Additionally, the effect of varying

jet-to-jet spacing (s/d_{jet}) and jet length (t/d_{jet}) will be investigated. The effect of relative jet spacing will be examined at 4 diameters and 8 diameters, and the relative jet length (t/d_{jet}) will be examined at 1.33, 2.5, and 4 diameters. It is important to note that for the aforementioned tests the hydraulic diameter of the jets is held constant at d_{jet} = 0.953 cm, the jet-to-target surface distance is held constant at z/d_{jet} = 4, and the relative curvature of the target surface is maintained at D/d_{jet} = 5.33. Recall that while the jet-to-jet spacing is held at 8 diameters it is expected that there is minimal jet-to-jet interaction, and when the jet-to-target surface distance is less than approximately 6 diameters it is assumed that the potential core has not fully degraded and is still impinging on the target surface.

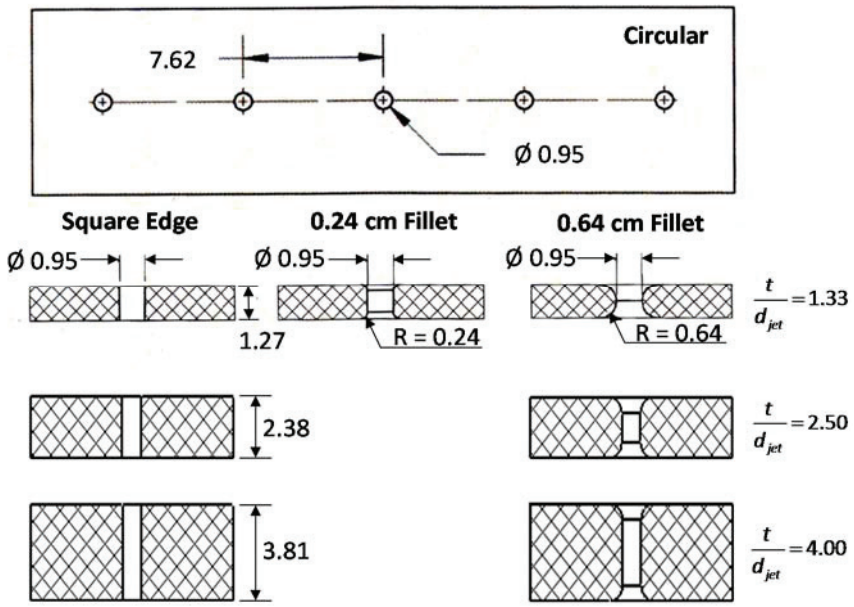

Figure 4.7: Geometrical details of circular jet plates with varying degrees of thickness and filleting (dimensions in cm).

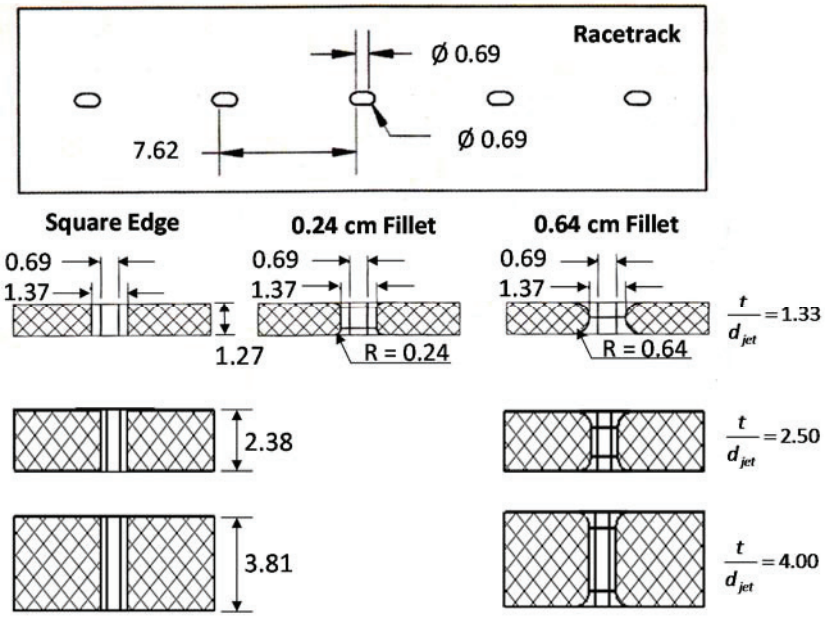

Figure 4.8: Geometrical details of racetrack jet plates with varying degrees of thickness and filleting (dimensions in cm).

CHAPTER FIVE

Rotating Heat Transfer Experimental Facility

Overview of Experimental Facility

The rotating heat transfer impingement facility was designed to model the interior cooling passage in the leading edge of a typical turbine airfoil. The test section features a square supply channel, and a semicircular impingement cavity. The walls of these channels are lined with individual copper plates to allow for the collection of regionally averaged heat transfer coefficients by using a traditional, steady state experimental technique. The heat transfer trends observed within the impingement cavity provide valuable insight into the complex flow characteristics of rotating impingement cooling. Additionally, the rotating test section can accept interchanging jet plates, which allows for the investigation of various jet geometries.

An overview of the rotating facility is shown in Figure 5.1. The cooling air is provided by a large compressor, and the mass flow rate is measured using an ASME square edge orifice meter. Upstream of the orifice meter are a pressure regulator and three inline air driers to remove any unwanted moisture in the air supply. The cooling air then travels through a ¾ inch hose and into a rotary union. The air then travels through a ½ inch hose, through the slip ring, radially outward down the rotating arm, and enters the supply side of the test section. The cool air then makes its way through the entrance of the pressurized test section, turns 90 degrees through the jet plate and impinges on the semicircular target surface. The spent air then travels back radially inward toward the exit. The air now exits the test section via a second ½ inch rubber hose, travels back up

the rotating arm and is exhausted out of a rotary union on the opposite side of the test section. A ball valve just downstream of the exit rotary union is used to regulate the pressure within the test section to 125 psi.

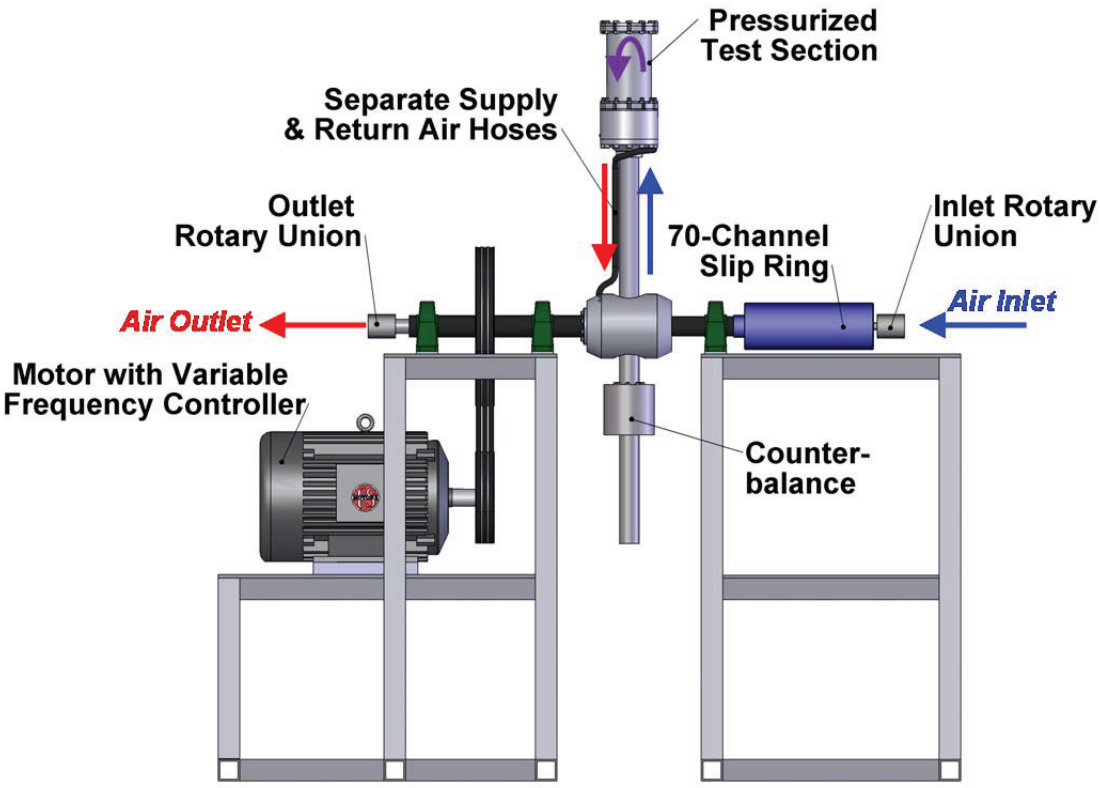

Figure 5.1: Overview of rotating facility.

Flow Measurement and Rotation Parameters

The same supply flow measurement setup is used for this facility as for the Honeywell Aerospace impingement facility, to control the total mass flow of supply air entering the apparatus. A regulator is used to control the pressure upstream of the first orifice plate, and is set to 125 psi. The total mass flow rate for the cooling air supply can be determined using Equation 4.1 produced by Leary and Tsai [61]. The duct Reynolds numbers were initially determined by specifying a mass flow rate to yield the desired jet

Reynolds numbers during testing. The impingement cases are run at jet Reynolds numbers of 15,000 and 25,000 (duct Reynolds numbers of approximately 2,800 and 4,600 respectively). An expression for the jet Reynolds number is given in Equation 4.4.

In addition to the changing flow rates, the rotational speed of the test section was also varied to achieve a diverse range of rotation and buoyancy numbers for the impinging jet. The rotation number, shown in Equation 5.1, is a dimensionless velocity ratio used to quantify the effect of rotation on fluid flow. For an impinging jet, the characteristic length used is the jet diameter.

$$Ro = \frac{\Omega \cdot d_{jet}}{V_{jet}} \tag{5.1}$$

In this equation for the jet rotation number; Ω is the rotational speed of the test section, d_{jet} is the hydraulic diameter of the jet, and V_{jet} is the fluid velocity through the jet. From this equation it becomes clear that there are two ways the rotation number (effect of rotation) can be increased. The first of these would be the intuitive option of simply increasing the rotational speed. The second option would be to decrease the fluid velocity through the jet. Additionally, it is difficult to achieve high rotation numbers that model realistic conditions in an experimental setting. The purpose of the test section being pressurized to 125 psi is to attain these high rotation numbers. By operating at an elevated pressure, the density of the cooling air is increased. Hidden in the velocity term of the rotation number definition is the density of the impinging fluid, and by increasing the density of the fluid, the rotation number is also increased. Specific details of all test cases investigated are shown in Table 5.1.

Table 5.1: Summary of test cases (cylindrical and racetrack jets).

Re_{jet}	Ω (RPM)	Ro_{jet}
15,000	0	0
	200	0.031
	300	0.046
	500	0.076
25,000	0	0
	200	0.018
	300	0.027
	500	0.046

While the rotation number is intended to provide a quantitative approach to the degree to which a fluid flow is being affected by rotation, some researchers argue that a more appropriate measure is the buoyancy number. The buoyancy number is most often discussed in the context of mixed convection (a combination of natural and forced convection). However, the buoyancy number definition can be modified to include the applied acceleration due to rotation instead of the acceleration due to gravity. The definition of the buoyancy number is given in Equation 5.2.

$$Bo = \left(\frac{T_w - T_{jet}}{T_w} \right) \cdot Ro_{jet}^{\ 2} \cdot \left(\frac{\overline{R}}{d_{jet}} \right) \tag{5.2}$$

In the simplest of terms, the buoyancy number is simply a ratio of forced convection to buoyancy driven convection, and provides a numerical gauge as to which is dominating. For channel flow, if the buoyancy number is less than unity, the flow is

being dominated by forced convective heat transfer. On the other hand, if the buoyancy number is greater than unity, the flow is being governed by the buoyant forces induced by rotation.

Pressurized Test Section

The test section used in this study is similar to the test section used in a previous study [62], and is designed to model the internal geometry of a modern, actively cooled, turbine airfoil. Figure 5.2 provides a cross-sectional view of the pressurized test section with flow lines. Cooling air flows radially outward through the square supply channel, turns through the jet orifice and impinges on the curved target surface. The spent air then travels back radially inward and exits the test section. By utilizing a single jet, the full effect of rotation on an impinging jet can be realized as the effects of crossflow and jet-to-jet interaction have been minimized. In a production turbine blade, crossflow is minimized through the use of showerhead film cooling techniques.

The walls of the test section are lined with individual copper plates, and are insulated from one another using a low conductivity silicone. Each copper plate on the walls of the square supply duct is 2.38 cm x 2.38 cm and has a thickness of 0.38 cm. For the supply duct, the three exterior walls (the fourth interior wall is made up by the jet plate) are instrumented with copper plates, and are designated leading, side, or trailing. Additionally, the plates are numbered one through nine in the streamwise direction. In the semicircular impingement cavity, the walls are lined with curved copper plates. These plates are 2.38 cm in the streamwise direction, have an inner radius of 2.03 cm, have a thickness of 0.38 cm, and span an arc of 2.13 cm which is approximately one third of the

total arc length of the surface. Again, the plates are designated leading, stagnation, or trailing, and are numbered nine through one in the streamwise direction. On the backside of each copper plate, a blind hole is drilled in order to instrument the plate with a type T thermocouple. High conductivity epoxy is used to hold the thermocouple in place and minimize any contact resistance.

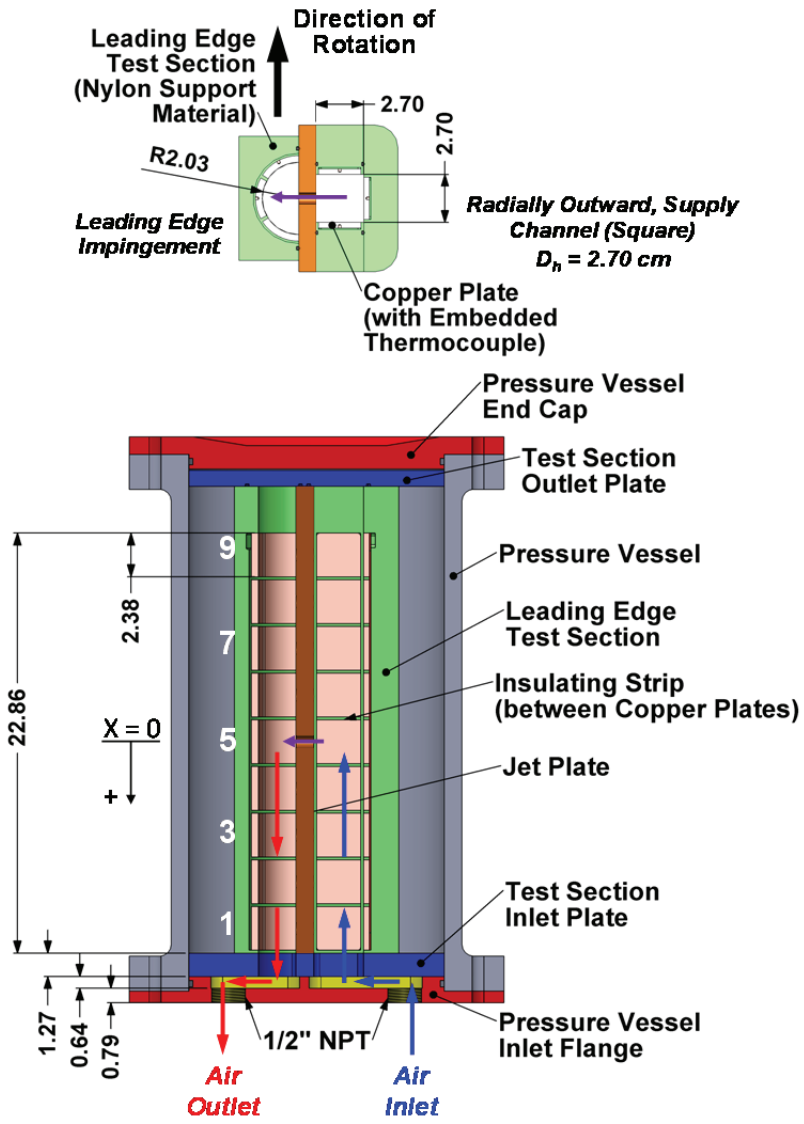

Figure 5.2: Cross-section of pressurized impingement test section.

All power and signal wires entering or leaving the test section must pass through a large slip ring that contains seventy channels. Only plates three, four, five and six on each of the walls (side wall of square supply duct excluded) are instrumented. The lone impinging jet is centered on plate five; therefore, $x/d_{jet} = 0$ corresponds to the center of copper plate number five. Once the cooling air strikes the curved impingement surface, the spent air travels radially outward (in regards to the jet orifice, not the rotating arm) away from the jet center. To maintain the elevated pressure within the test section, spent air must travel back radially inward through the impingement cavity toward the exit.

Each wall of the test section is outfitted with a dedicated silicone rubber resistance heater. Each heater is controlled via its own variable transformer. This arrangement of heaters means that there is a uniform heat flux for each wall of nine plates. However, while the heat flux is constant for a given wall of the test section, the streamwise temperature distribution will vary depending on the amount of heat transfer encountered at that location. While testing, plate five ($x/d_{jet} = 0$) is held at a constant temperature of approximately 66°C to ensure that the buoyancy number is known at that location.

Jet Geometries

The baseline jet geometry is a circular, square edged jet with a diameter of $d_{jet} = 0.64$ cm. The performance of a square edged, 2:1 racetrack shaped jet will be compared to that of a circular jet. Maintaining the same hydraulic diameter for both jets provides consistent geometric parameters for ease of comparison. Because there is only a single jet, the jet-to-jet spacing parameter is not germane to this discussion. The jet-to-target

surface spacing of $z/d_{jet} = 3.2$ would lend itself to the existence of the potential core when the jet strikes the target surface. Further, with a relative jet thickness of 1.5 jet diameters, the flow is still well below the threshold of being fully developed (typically assumed to be fully developed after ten diameters). Table 5.2 outlines these geometric parameters for convenience, and Figure 5.3 provides the geometric details of the impingement jet plates.

Table 5.2: Rotating leading edge impingement geometry.

d_{jet} (cm)	$\frac{s}{d_{jet}}$	$\frac{z}{d_{jet}}$	$\frac{t}{d_{jet}}$	$\frac{D}{d_{jet}}$
0.64	-	3.2	1.5	6.3

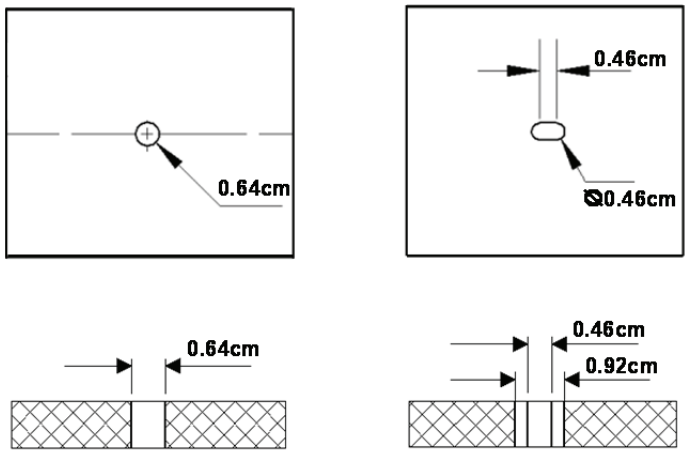

Figure 5.3: Impingement orifice details.

CHAPTER SIX

Honeywell Aerospace Impingement Results

This chapter presents the experimental results obtained using the Honeywell Aerospace experimental facility. Included is a discussion of the heat transfer characteristics associated with varying Reynolds number, jet shapes, edge conditions, jet-to-jet spacing, jet length, and supply flow conditions. Seeing as the initial objective of this research was to validate the transient liquid crystal impingement investigation conducted by Jordan et al. [4-7], it seems appropriate that the discussion start there. Direct comparisons will be made to the correlation developed by Chupp et al. [14] as well as the work produced by Jordan et al. [4-7] for the common test cases. Following, will be a discussion of the varying impingement geometries unique to this investigation. Experimental results from test cases with no radial bypass will be presented first to establish a baseline so that the effect of radial bypass can be clearly identified.

Validation of TLC Impingement Work

For the validation of the transient TLC investigation, four common geometries between the two studies are directly compared. These geometries all share the same hydraulic diameter of the jet (d_{jet} = 0.95 cm), jet-to-jet spacing (s/d_{jet} = 8), jet-to-target surface spacing (z/d_{jet} = 4), and relative jet length (t/d_{jet} = 1.33). The cases were all run at the same schedule of mass flow rates and bypass ratios for ease of comparison.

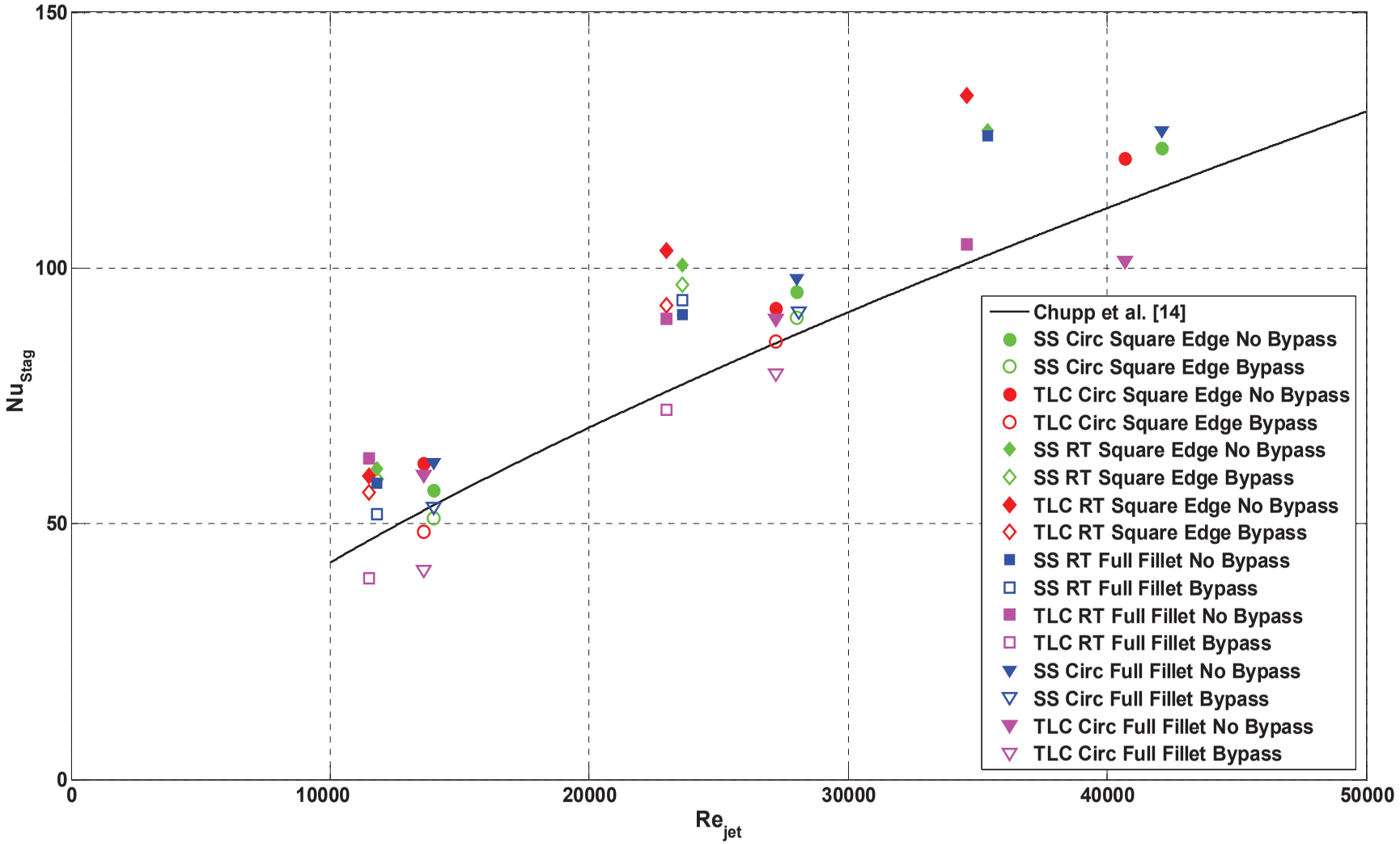

Figure 6.1: Comprehensive plot of TLC validation.

The unique jet shapes are a circular square edged jet, a circular fully filleted jet, a racetrack square edged jet, and a racetrack fully filleted jet. The details of these jets can be found in Figure 4.6 and 4.7. Figure 6.1 provides a comprehensive plot of the common test cases.

It must be noted that the Chupp et al. [14] correlation only applies to a circular, square edge jet; however, it is still interesting to see how the heat transfer afforded by shaped or filleted jets compare to what is predicted by the correlation. The data shown is a single period average of the stagnation region. This single period encompasses a streamwise distance of eight diameters ($-4 \leq x/d_{jet} \leq 4$ with $x/d_{jet} = 0$ centered on the centermost jet). For the circular, square edge jets, there is generally good agreement between the two experimental techniques. The results from the circular square edge jet are isolated in Figure 6.2.

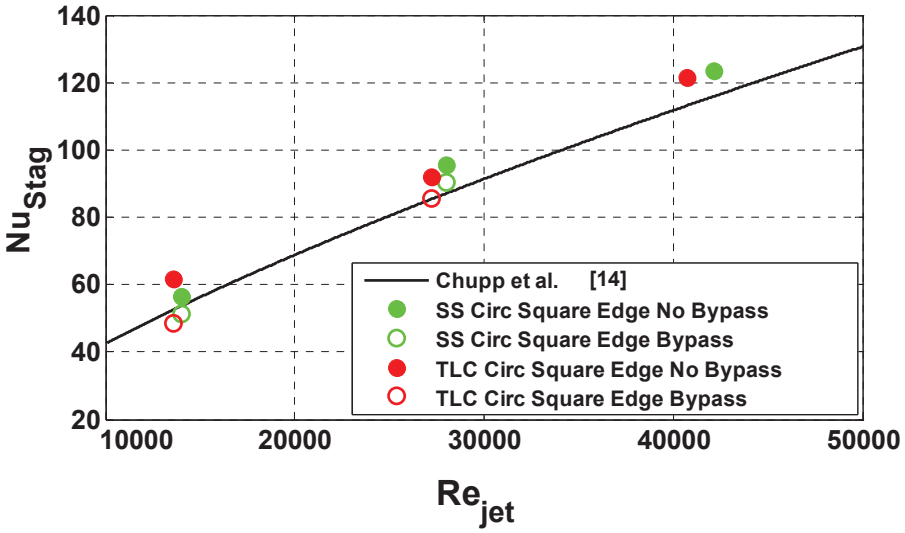

Figure 6.2: Isolated heat transfer results for a circular, square edge impinging jet.

Of the four jet geometries being compared in this section, the circular, square edge jet shows the most agreement between the steady state and TLC techniques.

Additionally, the Chupp et al. [14] correlation also agrees well with the experimental data, with all data points being within approximately 10% of the predicted heat transfer. As is expected, heat transfer increases with increasing Reynolds number. The reader should note the slight variation in Reynolds number between the two experimental techniques. This difference can be attributed to differences in air density between the two tests. For the TLC test, the working fluid was heated and impinged on a cool surface, while for the steady state test; the surface was heated rather than the impinging fluid. Furthermore, the circular, square edge jet is rather insensitive to the addition of radial bypass.

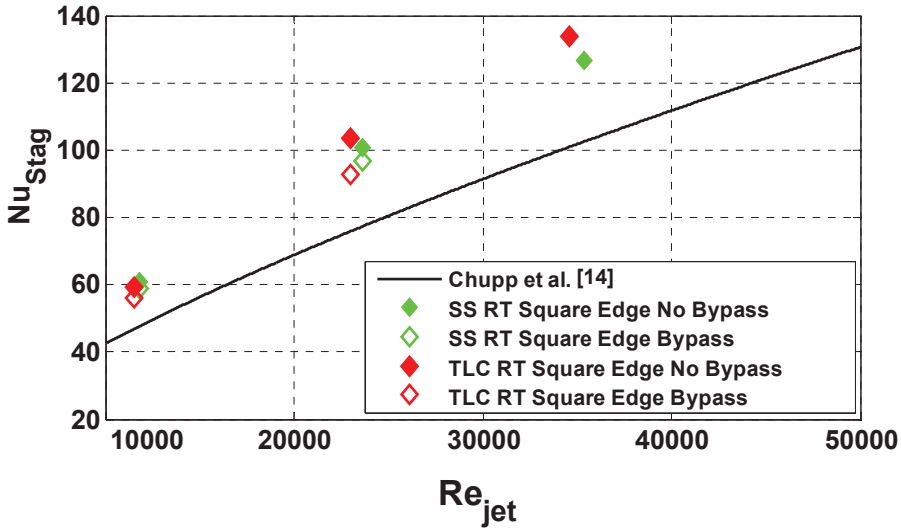

Figure 6.3: Isolated heat transfer results for a racetrack, square edge impinging jet.

The results of the racetrack shaped jet are shown in Figure 6.3. Again, there is very good agreement between the two experimental techniques used. The racetrack shaped jet does appear to outperform what is predicted by the correlation [14] indicating that the racetrack jet is providing increased heat transfer to the target surface. Referring back to Figure 6.1, the increased heat transfer offered by the racetrack jet for a given

mass flow rate is easily seen. The racetrack jet consistently provides enhanced performance over the circular jet in the stagnation region. Because the data reported is a stagnation strip average, the racetrack jet benefits greatly from the spreading associated with the impingement flow. The racetrack jet is simply able to provide high heat transfer over a larger area, thus not allowing its stagnation strip average to suffer as much from areas of lower heat transfer adjacent to the stagnation region. This would prove to be a benefit as thermal strains would be reduced in the leading edge by reducing the large temperature gradients. There is again, only slight degradation with the addition of radial bypass flow, indicating that square edge orifices are relatively insensitive to radial bypass conditions. Further, heat transfer continues to increase with increasing Reynolds number, but at an elevated rate compared to what was observed for the circular jet. The heat transfer performance offered by the circular jet appears to increase at the same rate as predicted in the correlation [14]. The racetrack jet, on the other hand, appears be increasing at a rate faster than the Chupp et al. correlation [14] predicts, hinting at slightly improved performance over the circular jet.

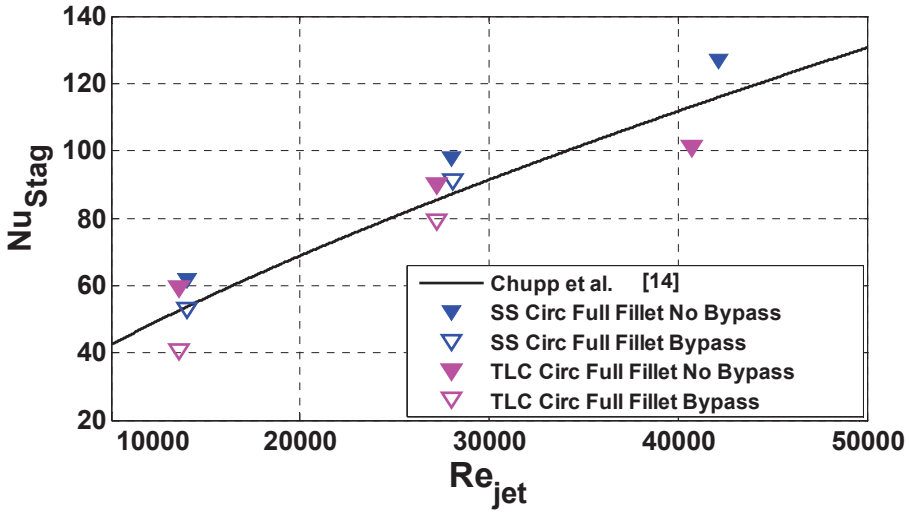

Figure 6.4: Isolated heat transfer results for a circular, fully filleted impinging jet.

Introducing a fully filleted edge on the circular jet (Figure 6.4) increased the heat transfer capabilities of the jet slightly over the square edge geometry. There is again very good agreement with the Chupp et al. [14] correlation, but we begin to see a decline in agreement between the independent experimental techniques as the Reynolds number increases. The steady state test results increase at approximately the same rate as predicted by the correlation, with increasing Reynolds number. However, the TLC results would indicate that the heat transfer is increasing at a slower rate than predicted by Chupp et al. [14] as the Reynolds number increases. Further, as it is shown here, the addition of the fully filleted edge makes the jet far more sensitive to the imposed radial bypass supply conditions. Additionally, the results obtained using the TLC experimental technique appear to suffer more from the radial bypass flow, than the steady state results.

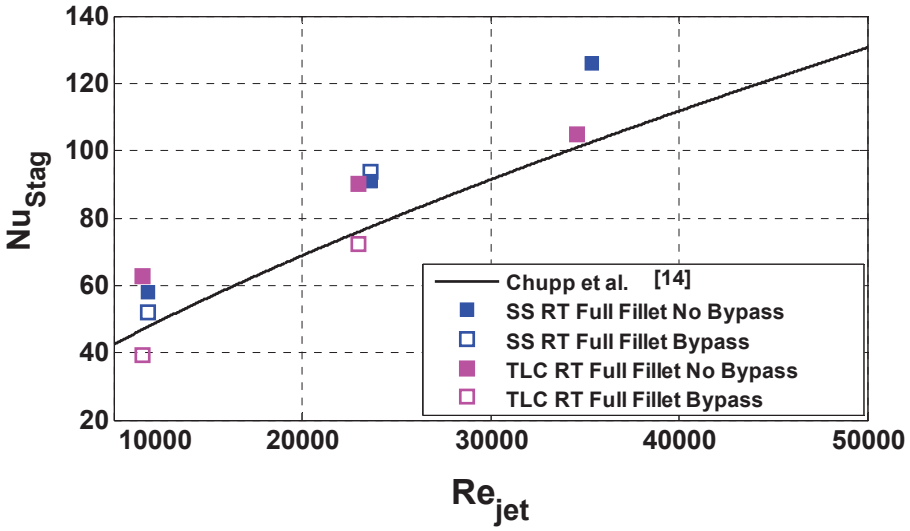

Figure 6.5: Isolated heat transfer results for a racetrack, fully filleted impinging jet.

Moving to a fully filleted racetrack shaped jet, much of the already discussed trends are observed. Heat transfer increases with increasing Reynolds number. The steady state heat transfer results increase at a slightly elevated rate with increasing Reynolds

number over what Chupp et al. [14] predicts for a circular, square edge orifice. The TLC data, on the other hand, reacts similar to what was shown for a circular, fully filleted jet. Showing that the heat transfer afforded by the fully filleted racetrack jet is increasing at a slower rate than predicted by Chupp et al. [14], as the Reynolds number increases. With the addition of radial bypass flow, the TLC data, again, indicates a sensitivity associated with the filleted jets, however, this is not wholly supported by the steady state results.

Effect of Jet Length

A significant portion of the current study was expanding the jet geometries to take into account longer jets. All geometric characteristics of the baseline jet plates were maintained with the exception of the thickness. Additional thicknesses of 2.5 and 4.0 diameters were produced and tested. At each of these additional thicknesses both a square edge and filleted jet were examined. The fillet radius was held constant at 0.635 cm for the thicker plates although this no longer constitutes a "fully filleted" jet. Further, a "partially filleted" jet is introduced at the 1.33 diameter thickness to round out the test cases. Figure 6.6 and 6.7 present the steady state Nusselt number results as a function of jet Reynolds number for both a circular jet and racetrack jet, respectively.

From these figures, there is no identifiable trend to be seen. However, these results are not unreasonable, or unexpected. Each of the jet lengths examined in this study are all relatively short. Typically, flow through a pipe is said to be fully developed after ten diameters, but all of the lengths tested are well below that. Therefore, it is reasonable to say that the flow exiting the jets is extremely underdeveloped for all of the jets tested, resulting in only moderate changes in heat transfer.

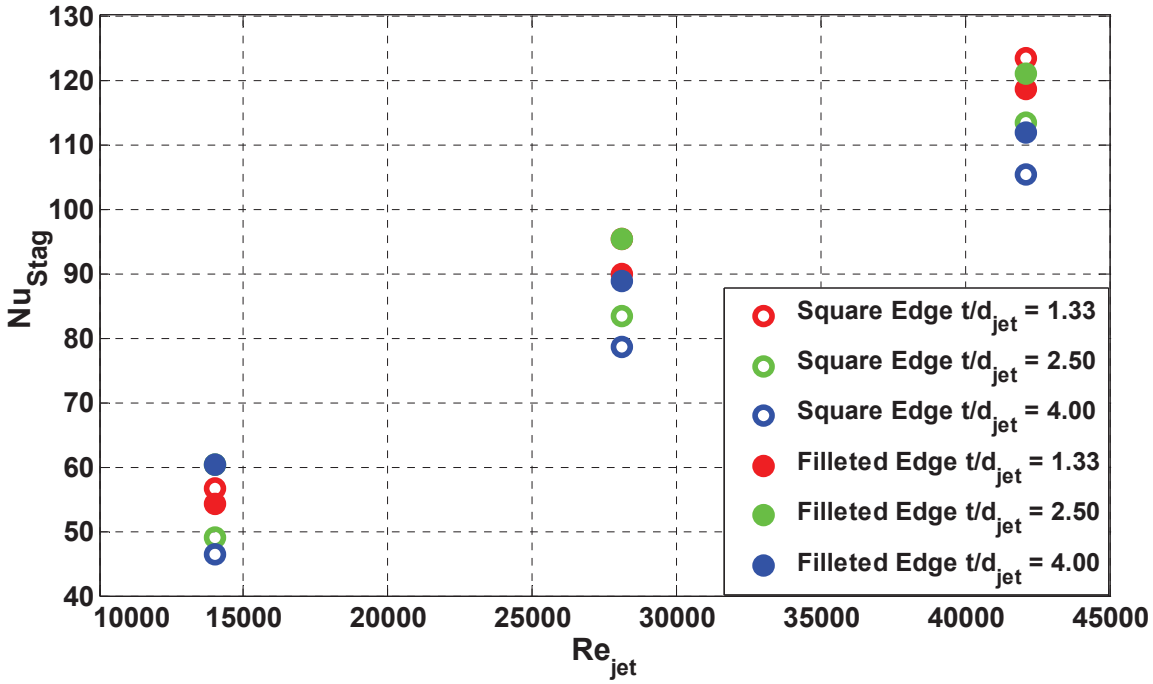

Figure 6.6: Stagnation strip heat transfer distribution: edge condition comparison for a circular jet.

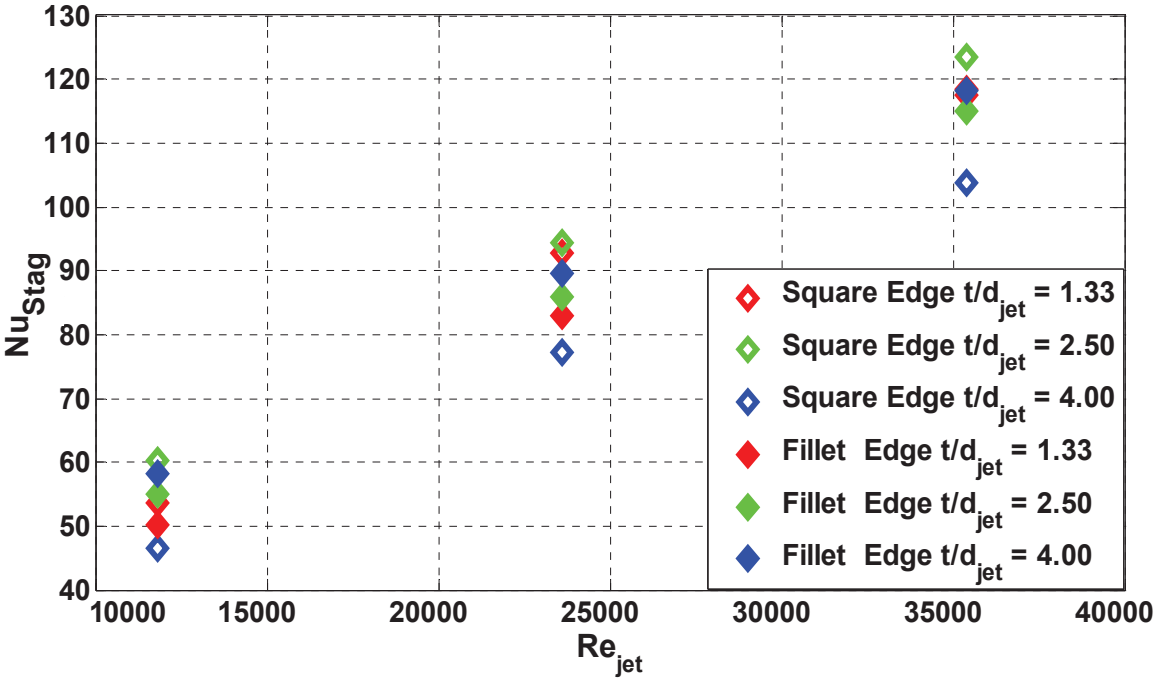

Figure 6.7: Stagnation strip heat transfer distribution: edge condition comparison for a racetrack jet.

Effect of Jet Edge Condition

An artifact of the jet length study, there were now several new jet geometries with varying degrees of filleting relative to the length of the jet. Seeing as there was not an identifiable trend to be seen previously, a different way to represent the data was sought out. It was then that the relative filleting radius of the jet was examined. Figure 6.8 gives the stagnation average Nusselt numbers as a function of varying degrees of filleting (R_{fillet}/t) for a circular jet.

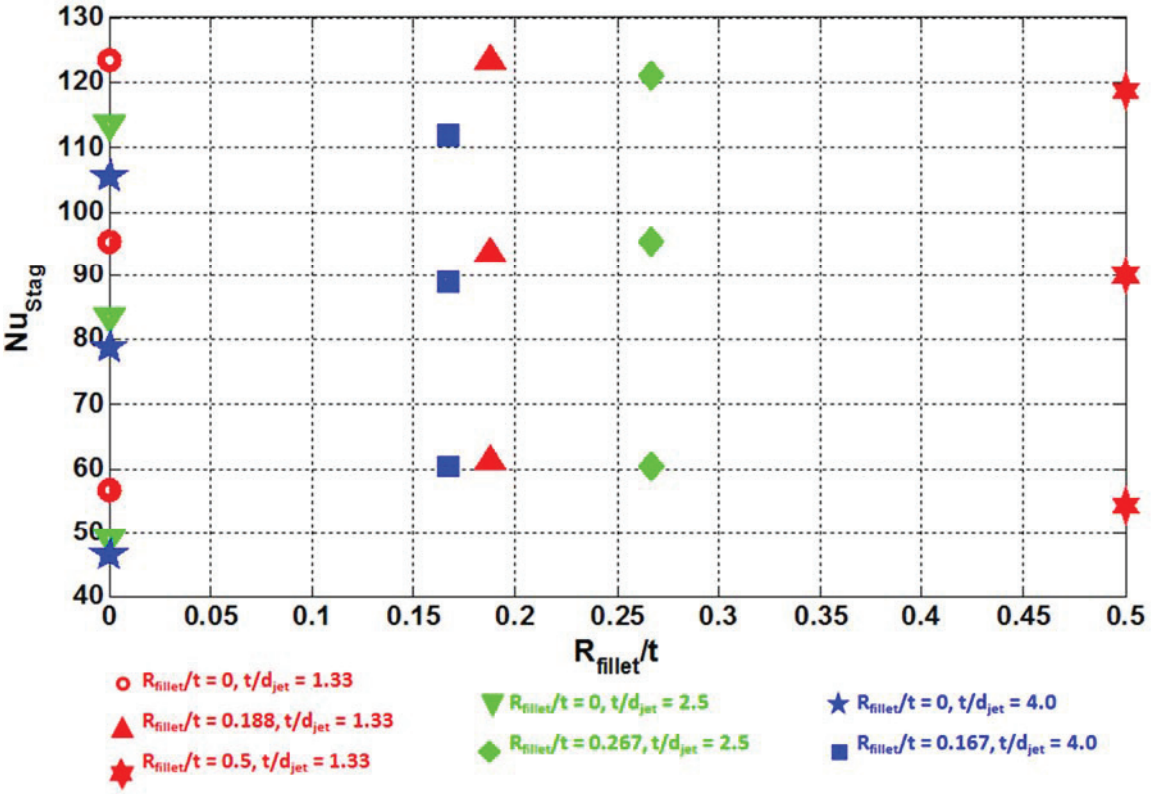

Figure 6.8: Stagnation average Nusselt numbers as a function of relative fillet radius for a circular jet.

For the circular jet, there is some variation in the level of heat transfer being imposed by the square edge jets ($R_{fillet}/t = 0$) of varying length, however there is much more uniformity at values of $R_{fillet}/t > 0$. The square edge jet is the most susceptible to

separation along the upstream wall of the jet. This separation creates a vena contracta effect that, for the shorter jet, would increase the jet velocity on the target surface due to the reduced flow area. This vena contraca effect would explain why the square edge jet with a $t/d_{jet} = 1.33$ would exhibit higher Nusselt numbers. The longer jets on the other hand provide enough length to recover from the separation at the inlet of the orifice, and thus do not benefit from the increased jet velocity. At higher Reynolds numbers, the shorter jets generally perform better, most likely due to the exaggerated separation at the jet inlet and the vena contracta effect. The longer jets ($t/d_{jet} = 4$) suffer as the Reynolds number increases. One important take away from this figure is that there is little change in the heat transfer provided by the shorter jets (red icons), regardless of the filleting condition. This would mean blade designers need not worry so much about the filleting of the cast impingement orifices, but only that the length of the orifice remains very short as it enters the leading edge. Figure 6.9 presents the relative filleting results for a racetrack shaped jet.

For the racetrack shaped jet, there is still the relatively wide variation in heat transfer for the square edge jets. Similar to the circular jet, the racetrack jet with a t/djet = 4 exhibit the lowest Nusselt numbers of those with a square edge ($R_{fillet}/t = 0$). However, unlike the circular jet, the middle length jet demonstrates the best performance at a given Reynolds number. The racetrack jet seems to provide even more uniformity across the spectrum of varying relative fillets than its circular counterpart. The longer jets do not appear to suffer like they did for the circular jet, with the only instance being the square edge jet with a $t/d_{jet} = 4$. If anything could be said about the heat transfer trends for

the racetrack jet, it would be that the heat transfer seems to peak at lower values of relative filleting; however, this is not consistent among the square edge jets.

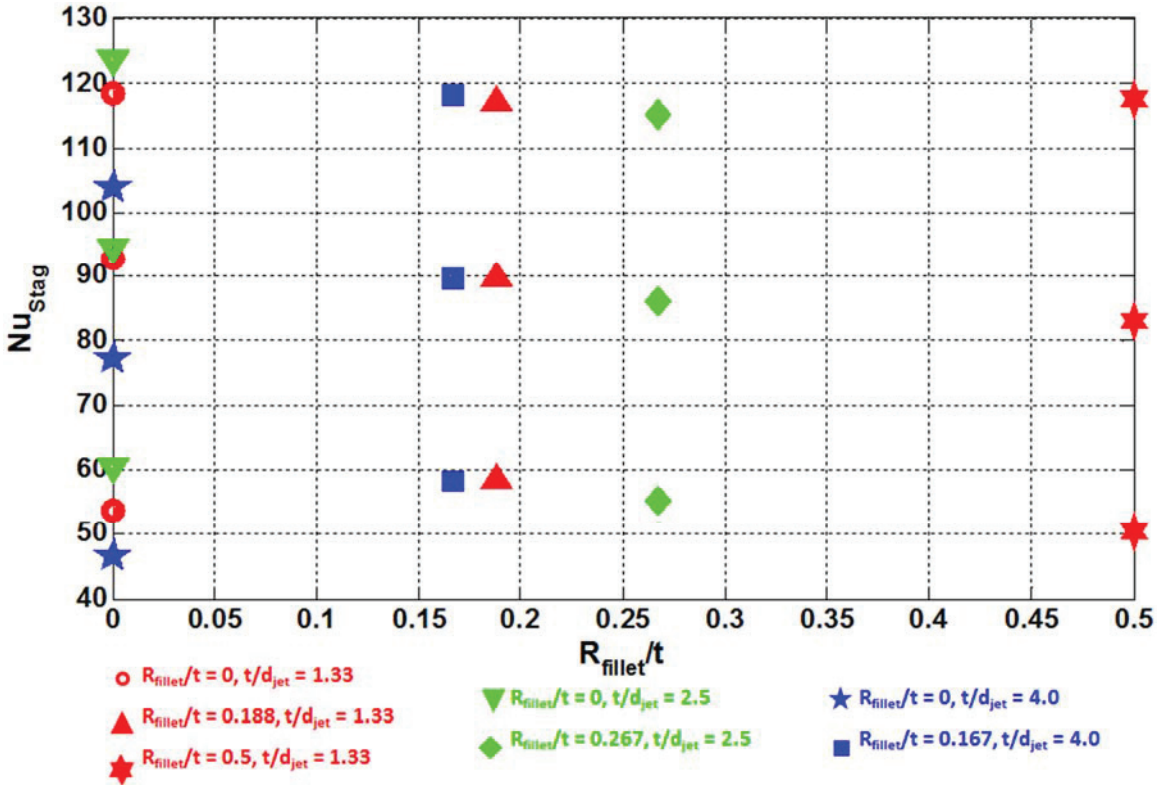

Figure 6.9: Stagnation average Nusselt numbers as a function of relative fillet radius for a racetrack jet.

Effect of Varying Jet-to-Jet Spacing

Figure 6.10 presents a side by side comparison to the Chupp et al. [14] correlation for a circular, square edge jet at jet-to-jet spacings of four and eight diameters. This plot is intended to validate the experimental setup for the new jet-to-jet spacing. For the jet spacing portion of this study, only a circular square edged jet, a circular fully filleted jet, a racetrack square edged jet, and a racetrack fully filleted jet were investigated.

Just as was seen with the jet-to-jet spacing of eight diameters, the smaller jet spacing also shows good agreement with what is predicted by the Chupp et al. [14]

correlation (within approximately 10%). However, the correlation for the jet-to-jet spacing of eight tended to under predict the heat transfer, while the heat transfer for a jet spacing of four diameters is over predicted, indicating that perhaps the Chupp et al. [14] correlation weighs too heavily the jet-to-jet spacing parameter.

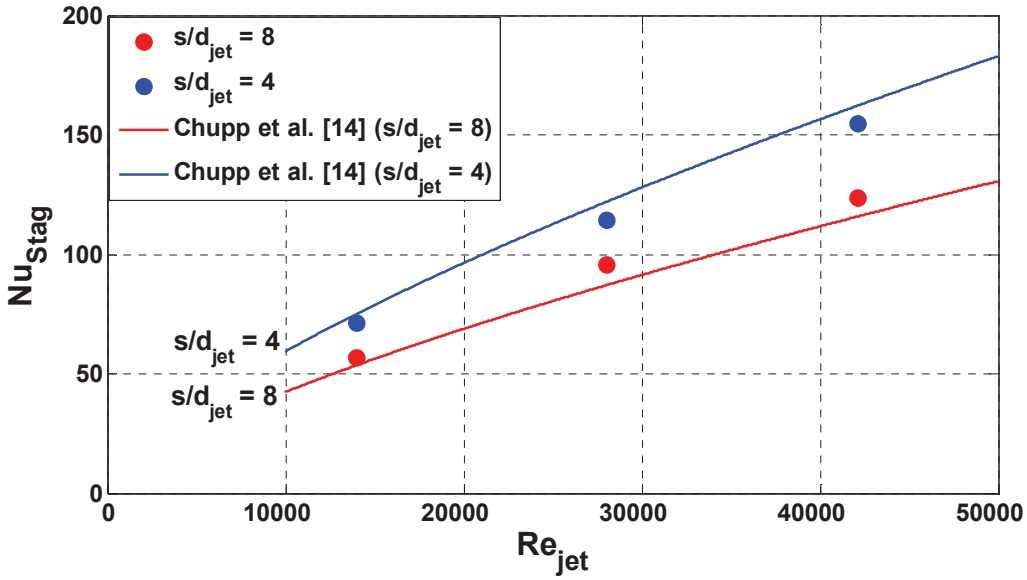

Figure 6.10: Heat transfer trends for varying jet-to-jet spacings for a circular, square edge jet.

Again, the Chupp et al. [14] correlation only applies to a circular, square edge orifice, but it is still interesting to see how the other jet geometries stack up to what is predicted. Figure 6.11 shows the stagnation average heat transfer at various jet shapes, for both no bypass and bypass flow compared to the Chupp et al. [14] correlation.

For nearly every jet geometry represented in this figure, the racetrack shaped jets generally outperform the circular jets with the same edge condition. Contrary to how the correlation is over predicting heat transfer trends for the circular, square edged jet for a jet spacing of four diameters, the racetrack jet is consistently under predicted for the no radial bypass cases. The increased coverage offered by the racetrack jet, again, allows for

higher stagnation region average Nusselt numbers. Furthermore, the racetrack shaped jets generally all fall within ten percent of the Chupp et al. [14] correlation, with there being more deviation seen from the circular jets.

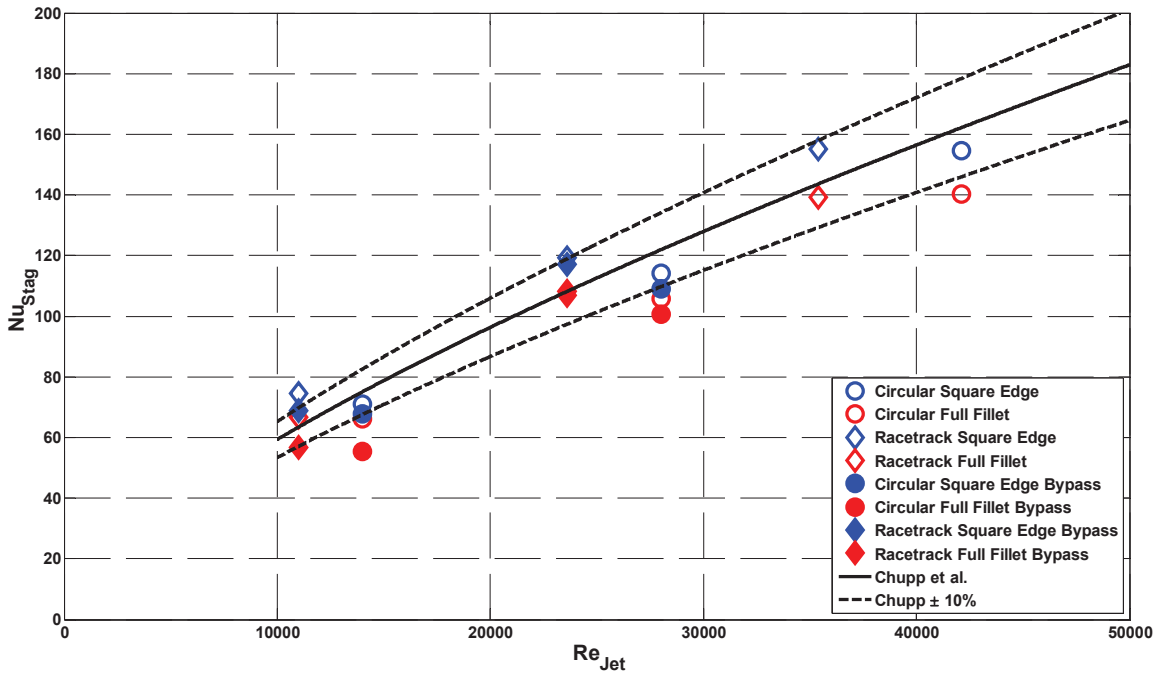

Figure 6.11: Comparison of varying impinging jet shapes to Chupp et al. [14] correlation ($s/d_{jet} = 4$).

Effect of Radial Bypass Flow

Radial bypass flow has been discussed in passing in previous sections of this chapter. Many of the figures shown have included data for test cases that contained bypass conditions. All radial bypass cases were conducted with a supply duct Reynolds number of 30,000. Then a fraction of the supply mass flow rate was siphoned off using the inline blower to provide matching mass flow rates through the jets that match the lower Reynolds numbers cases. Unless otherwise noted the discussion will be dealing with the centermost jet ($x/d_{jet} = 0$) as this is where the stagnation strip average was taken. Additionally, there should be no effects from the ends of the test section. The consensus

among these results is that cases with a radial bypass supply flow conditions suffer from decreased target surface Nusselt numbers. The square edge jets generally do a good job of redirecting the flow back perpendicular to the target surface. The filleted jets, however, allow the flow through the jet to maintain some of its streamwise momentum. This streamwise momentum is then carried over to the impingement cavity, and results in deflection of the jet. By deflecting, the jet-to-target surface is slightly lengthened, and the velocity perpendicular to the surface is decreased, thus providing degraded heat transfer performance compared to the square edged jet.

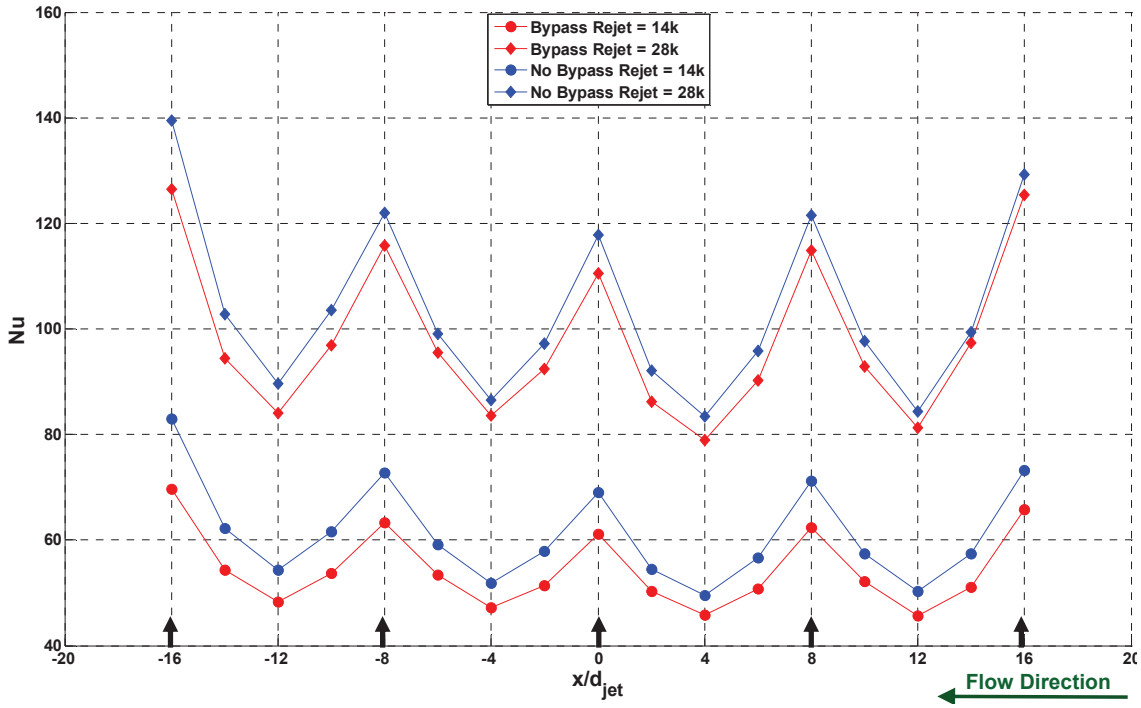

Figure 6.12: Streamwise heat transfer distribution for a circular, square edge jet with radial bypass flow.

Figure 6.12 provides a streamwise distribution for a circular square edged jet. The radial bypass cases, shown in red, are both slightly degraded compared to the no bypass case. Furthermore, there is more degradation at the higher bypass ratio. Not seen here is

the deflection of the jet. While the square edge orifice does mitigate jet deflection to an extent, it is hypothesized that the jet is still deflecting slightly (this was demonstrated by Jordan [4]); however, due to the limited resolution of the steady state test section, this small amount of deflection is not measurable.

Moving to the circular fully filleted jet, Figure 6.13, there is clear deflection of the jet, particularly at the lower Reynolds number (higher bypass ratio). It would appear that if there was better resolution on the target surface the Nusselt number distribution would peak one diameter downstream of the impingement location (x/d_{jet} = -1). There is dramatic degradation of the target surface heat transfer coefficients. This is due to the fact that the filleted orifice does not have substantial enough length through the jet to reorient the flow back perpendicular to the target surface. The streamwise momentum continues to push the core of the jet further downstream resulting in dramatically reduced Nusselt numbers along the entire target surface.

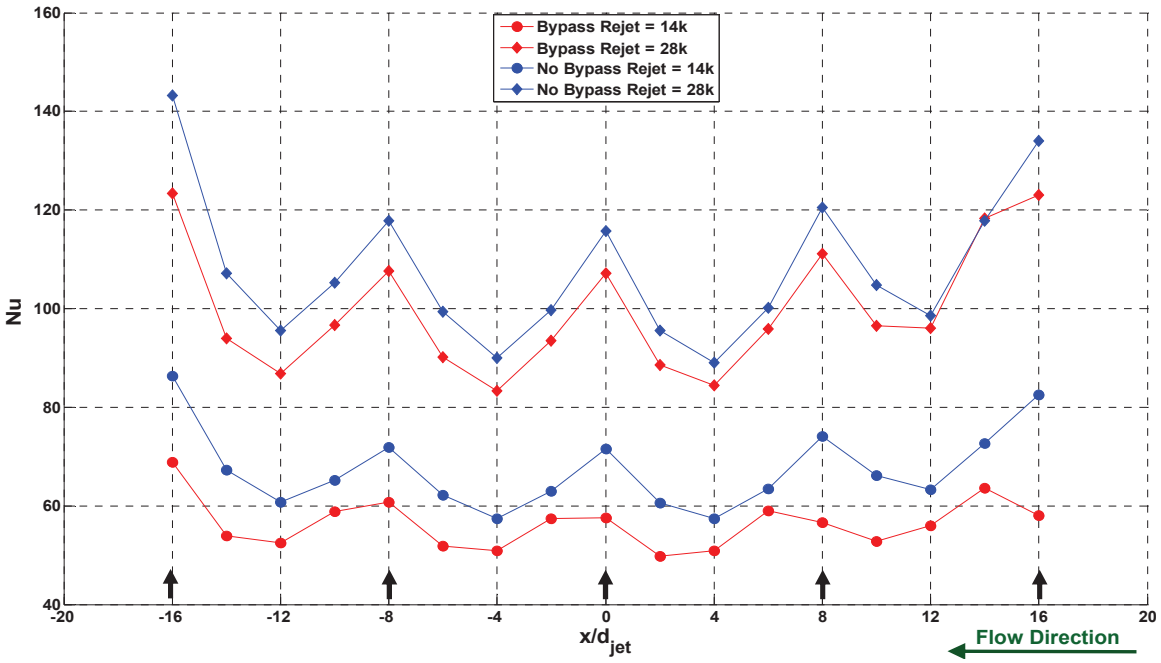

Figure 6.13: Streamwise heat transfer distribution for a circular, fully filleted jet with radial bypass flow.

The racetrack shaped jet shows much of the same trends as the circular jet, however, due to its elongated shape, is more susceptible to deflection of the jet. Figure 6.14 shows the performance of a racetrack, square edge jet. Notice, that even for a square edge jet, at the higher bypass ratio (lower Reynolds number), there is some degree of jet deflection as a result of the addition of radial bypass supply flow.

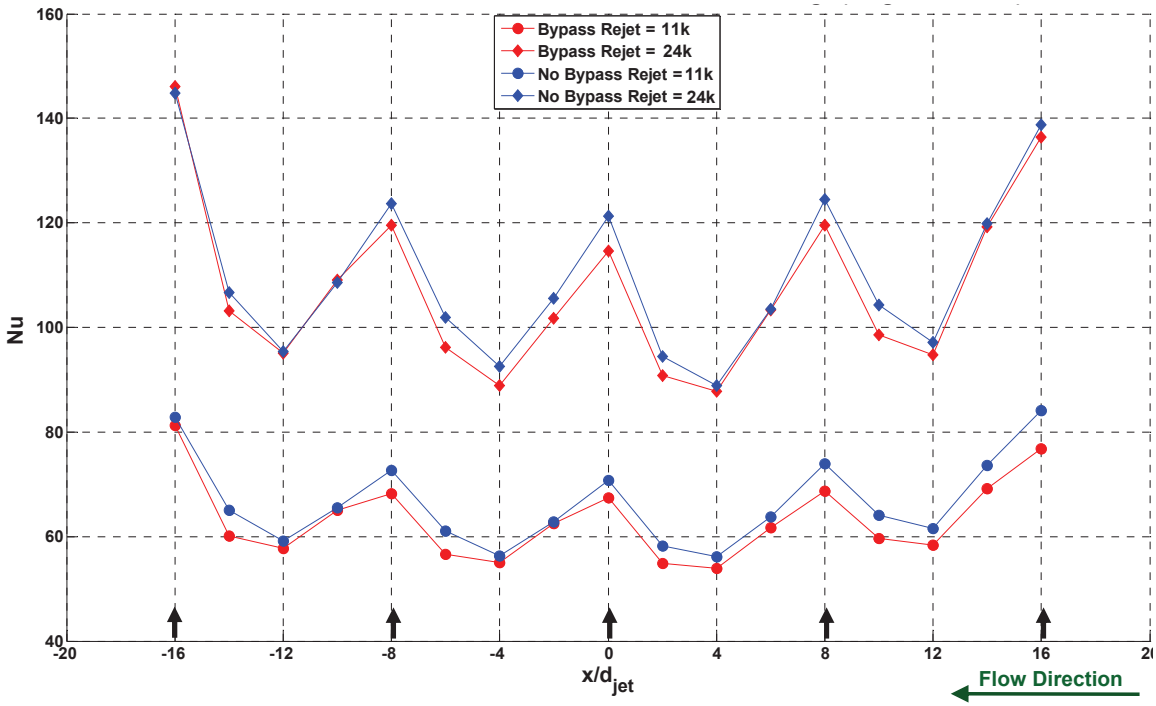

Figure 6.14: Streamwise heat transfer distribution for a racetrack, square edge jet with radial bypass flow.

It would stand to reason that the addition of a full fillet to the racetrack would further degrade the performance of the jet. Shown in Figure 6.15 is the streamwise distribution for the fully filleted, racetrack shaped jet. Just as was seen with the addition of the full fillet for the circular jet, the racetrack jet degradation is dramatically reduced at the lower Reynolds number. The Nusselt number peaks are shifted a full two jet diameters downstream of the intended impingement location.

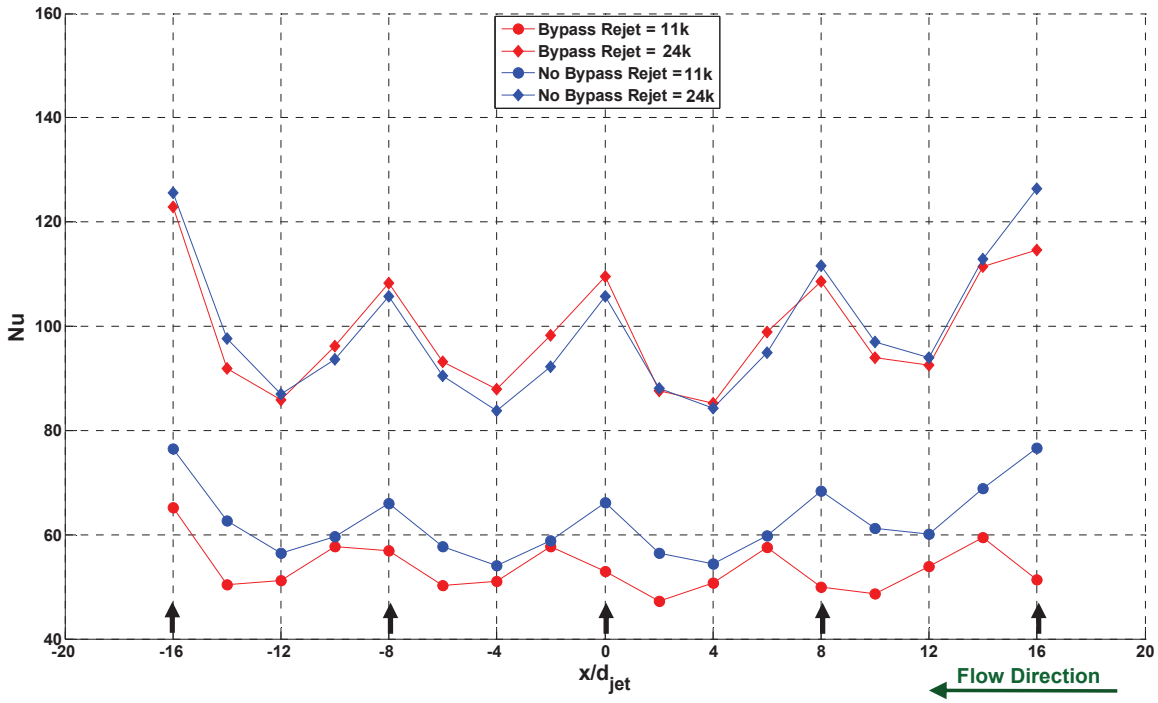

Figure 6.15: Streamwise heat transfer distribution for a racetrack, fully filleted jet with radial bypass flow.

The longer jets ($t/d_{jet} > 1.33$) behave very similarly to the square edged jets. The additional length allows the flow to orient itself perpendicular to the target surface before exiting, and mitigates any deflection due to radial bypass conditions. Therefore, no measurable deflection of the jet was observed for these test cases with or without filleting. Figure 6.16 provides the streamwise heat transfer distributions for a circular and racetrack shaped jet with a high bypass ratio. All of the streamwise distributions here are under radial bypass conditions. As discussed previously, the square edge jets are able to reorient the flow back perpendicular to the target surface. This is why for the top row of subfigures there is little to no noticeable deflection of the jet. However, moving to the bottom row, significant deflection is observed for the jets with a thickness of 1.33 diameters. The fully filleted, racetrack is degraded most among the jets tested and this drastic decrease in target surface heat transfer is apparent from the figure.

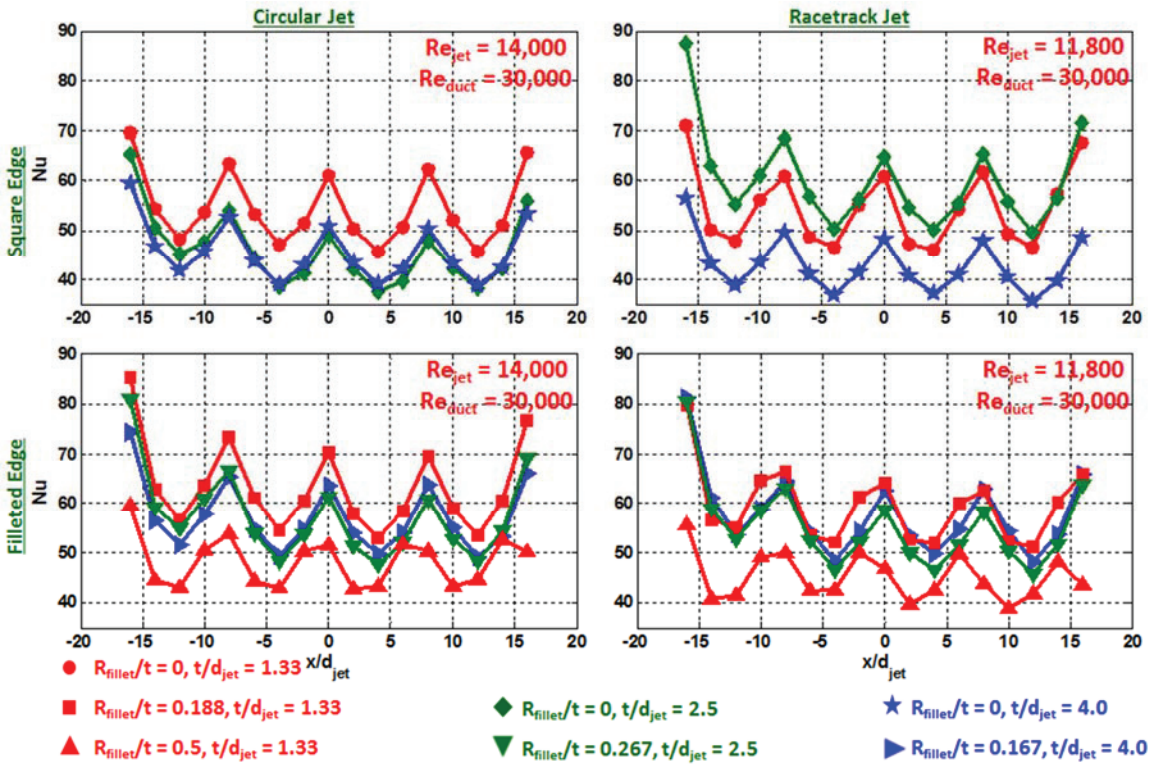

Figure 6.16: Streamwise heat transfer distribution for various jet geometries with radial bypass flow.

Figures 6.17 and 6.18 show the stagnation strip average Nusselt numbers for a circular and racetrack shaped jet with (red) and without (blue) bypass. In general, the radial bypass supply condition degrades the target surface heat transfer regardless of the jet shape, length, or edge condition. These results support the findings of Jordan [4] who also showed radial bypass flow to have a negative impact on target surface Nusselt numbers. In addition to the streamwise momentum being carried over into the impingent cavity and deflecting the jets, the increased streamwise velocity component induces stronger separation along the edges of the jet. This separation can, in turn, induce strong vorticies within the jet which interact with the spent air within the impingement cavity. The spent air is entrained by these vorticies, and can lead to premature diminishment of the potential core of the jet, which considerably degrades the target surface heat transfer.

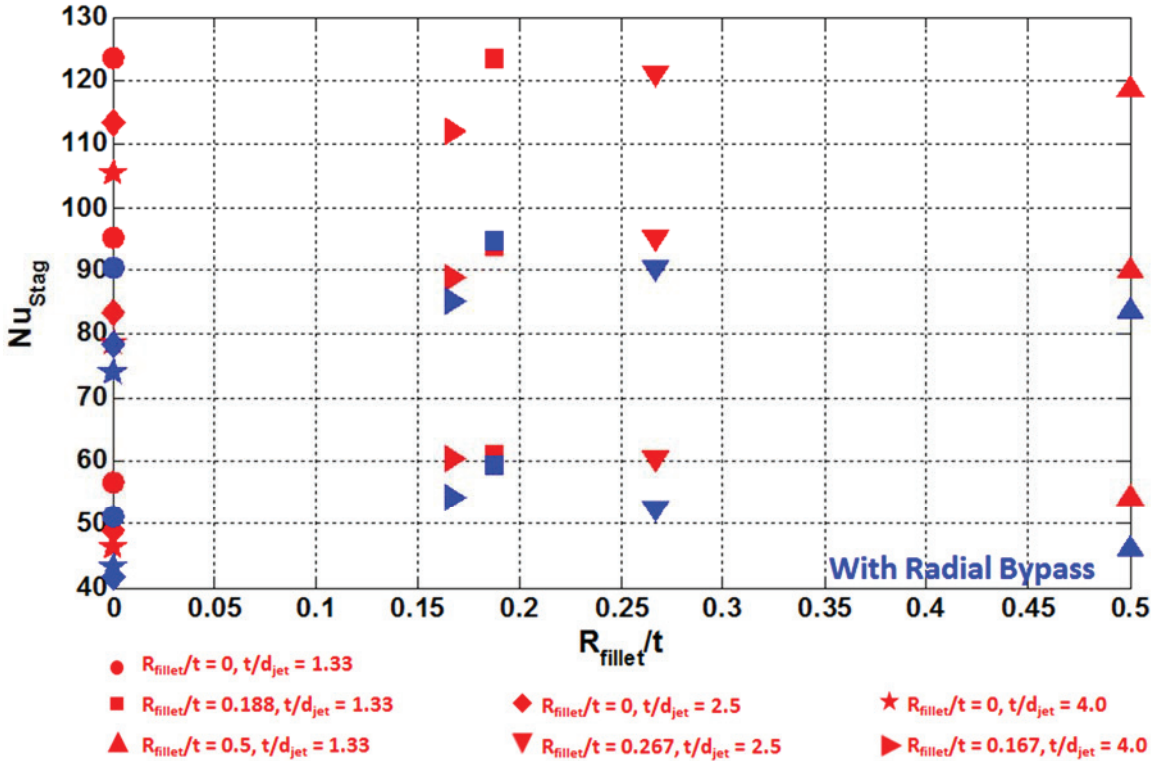

Figure 6.17: Radial bypass effect for a circular jet with varying length and edge condition.

In summary, the baseline steady state experimental results compare well to the heat transfer trends predicted by Chupp et al. [14]. Further, the experimental results obtained by Jordan et al. [4-7] using a transient TLC technique are validated using the steady state method. It was again shown that a racetrack jet does provide slight improvements in target surface heat transfer over its circular counterpart, at a given mass flow rate. The addition of filleting helps to reduce the vena contracta effect within the jet orifice; however, filleted jets are also more prone to degradation when radial bypass flow is present. Thinner jets have the potential to offer the highest levels of heat transfer, but are also more susceptible to jet deflection under bypass flow conditions. By lengthening the jet, there is a marginal decrease in target surface heat transfer, however, a longer jet would appear to be more robust in managing varying supply conditions.

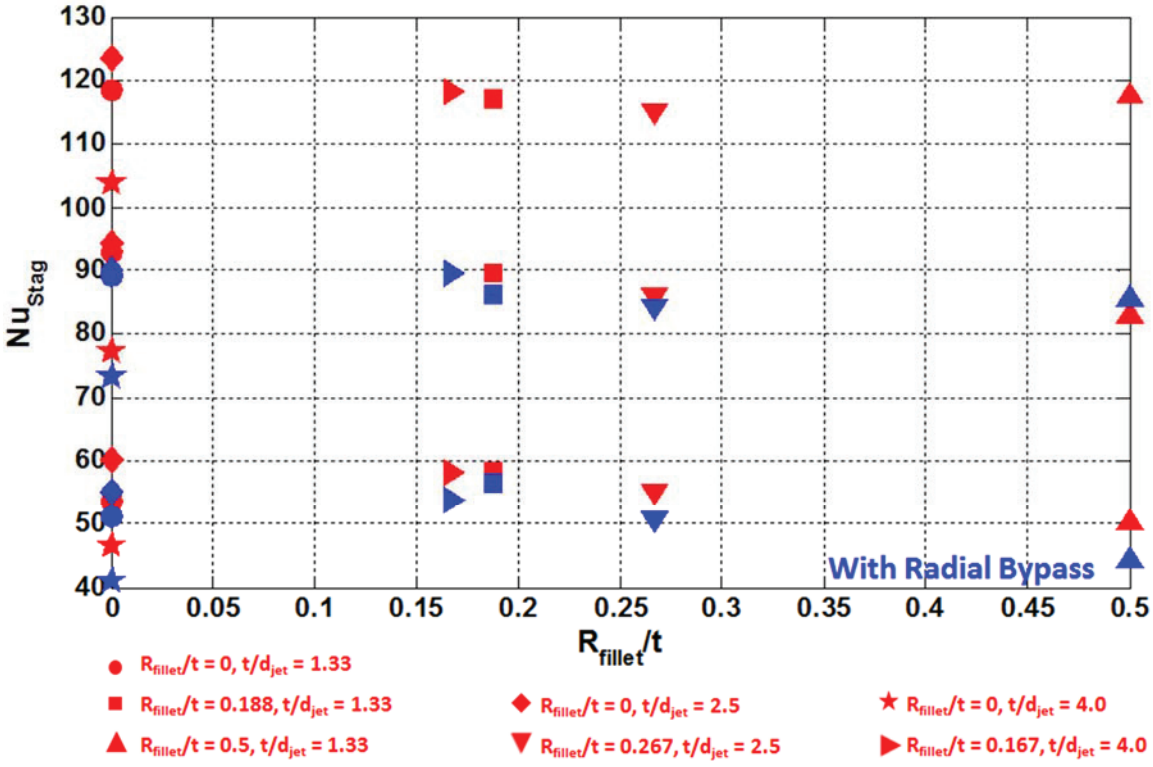

Figure 6.18: Radial bypass effect for a racetrack jet with varying length and edge condition.

CHAPTER SEVEN

Rotating Heat Transfer Results and Discussion

Before discussing the results of rotating heat transfer, it is imperative that the results obtained while the test section was stationary be discussed first. Stationary tests were conducted in an effort to establish a baseline quantity of heat transfer so that the enhancement resulting from rotation is more easily identifiable. For the stationary tests conducted, comparisons will be made to Chupp et al. [14] for stagnation average Nusselt numbers. Additionally, the surface averaged heat transfer will be shown. Regionally averaged Nusselt numbers will be presented as a function of streamwise location, rotation number, and buoyancy number. Furthermore, direct comparisons will be made to identify the effect of jet shape on target surface heat transfer.

Stationary Heat Transfer

The streamwise Nusselt number distribution obtained from a circular, square edged jet at jet Reynolds numbers of 15,000 and 25,000 is shown in Figure 7.1. Recall that an $x/d_{jet} = 0$ corresponds to the stagnation location of the impinging jet, and positive x/d_{jet} values increase moving downstream (radially inward) toward the exit of the channel. From the figure, it is evident that all regional heat transfer measurements are higher at a Reynolds number of 25,000 than at a Reynolds number of 15,000. This is consistent with findings in other research: that heat transfer increases with increasing Reynolds number. It is also important to note that heat transfer is highest at the point of stagnation. From the stagnation point the Nusselt numbers decrease as the spent air

travels away from the center of the jet (in both the streamwise and circumferential direction). This decrease can be attributed to the thickening of the wall jet boundary layer as the jet dissipates across the target surface. To either side of the jet in the streamwise direction ($x/d_{jet} = \pm 4$), there is a relatively uniform decrease in the target surface Nusselt numbers. This trend is indicative of the absence of a crossflow effect; however, the flow does seem to marginally prefer the plate in the downstream direction toward the outlet of the test section. Provided in Figure 7.2 are the stationary results for a square edged, racetrack shaped jet. The results shown indicate slightly higher levels of heat transfer than that offered by the circular jet. With the exception of the slight increase in the streamwise Nusselt numbers, both jet shapes provide a similar overall heat transfer trend for a stationary channel.

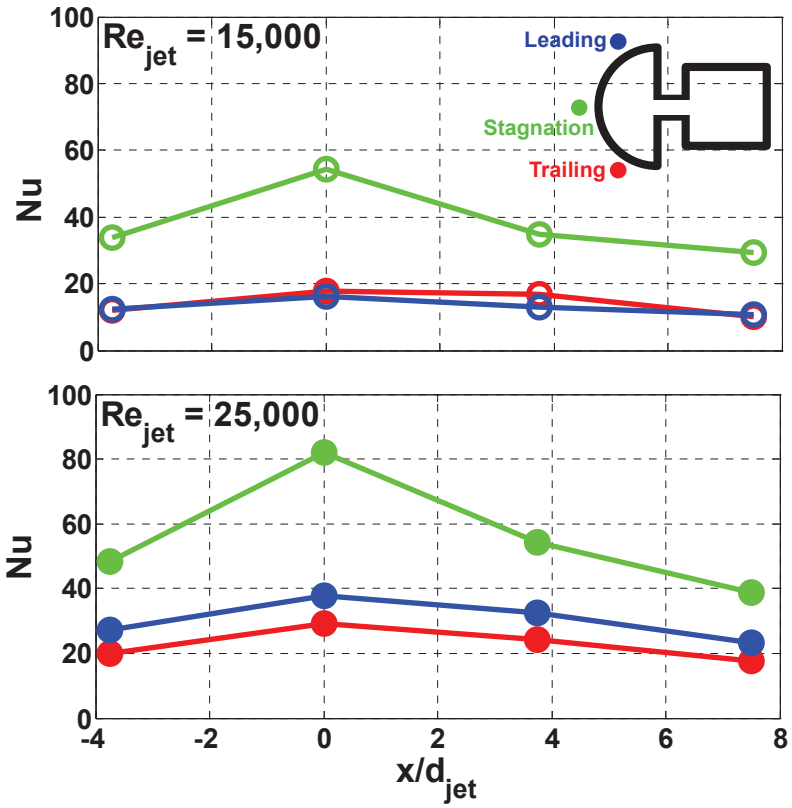

Figure 7.1: Streamwise Nusselt number distribution in a stationary channel with a circular jet.

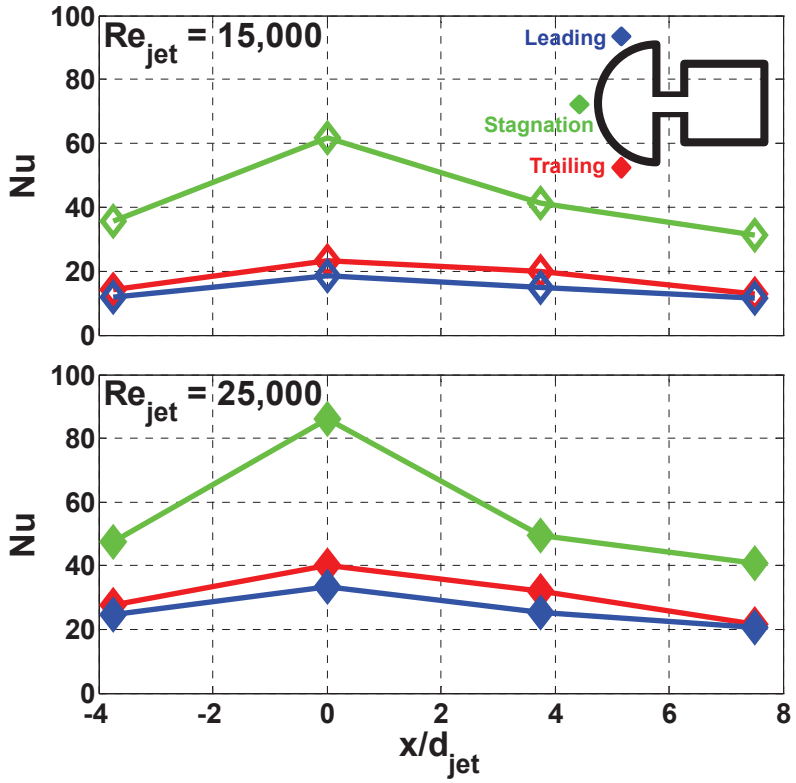

Figure 7.2: Streamwise Nusselt number distribution in a stationary channel with a racetrack jet.

In an effort to benchmark the stationary channel impingement results, Figure 7.3 provides a direct comparison of stagnation region Nusselt numbers obtained with the current experimental setup to those predicted by the correlation developed by Chupp et al. [14]. Because the current investigation uses only a single jet, the jet-to-jet spacing used in the correlation is twelve diameters. This is because the total streamwise length of the three plates being averaged spans twelve jet diameters. Generally, a jet-to-jet spacing of eight diameters in said to have no jet-to-jet interaction. Although the Chupp et al. [14] correlation only accounts for a circular jet, it is interesting to see how a racetrack jet compares in performance. It is important to point out that the values presented in Figure 7.3 are a stagnation region average ($x/d_{jet} = \pm 6$ (plates 4, 5, and 6)). Both jet shapes, at both Reynolds numbers are within 10% of the heat transfer predicted by Chupp et al.

[14]. At the lower Reynolds number the heat transfer provided by the circular jet is less than that predicted by the correlation; however, the racetrack jet provides a significant increase in heat transfer. At the higher of the two Reynolds numbers, both jets perform similarly.

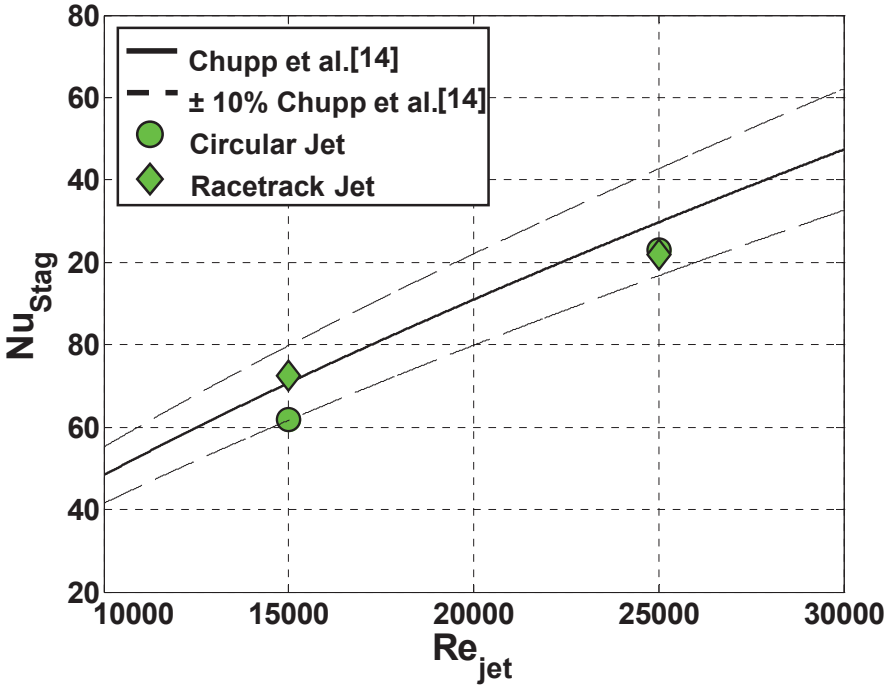

Figure 7.3: Stagnation region average Nusselt numbers compared to Chupp et al. [14].

Previously, both Taslim et al. [30, 31] and Jordan et al. [5] have made known the improved cooling performance afforded by racetrack shaped impinging jets. With the investigations performed by Taslim et al. [30, 31], the jet Reynolds number was maintained for both the circular and racetrack shaped jets. Much like was done with the present study; the mass flow rate through the jet orifice was increased for the racetrack shaped jet to maintain a constant Reynolds number. Because of this, the improved performance from the racetrack shaped jet is attributed to the increased mass flow rate of coolant. In the investigation performed by Jordan et al. [5], the mass flow rate through the

jets was conserved between the circular and racetrack shaped jet. Due to this, a slight decrease in the jet Reynolds number was observed for the racetrack shaped jet. In their investigation, Jordan et al. [5] observed enhanced performance from a 2:1 racetrack shaped jet over a circular jet (at a constant mass flow rate). While the flow conditions of the current study certainly vary from that of these previous studies, the general trend of racetrack jets offering increased heat transfer over circular jets is confirmed.

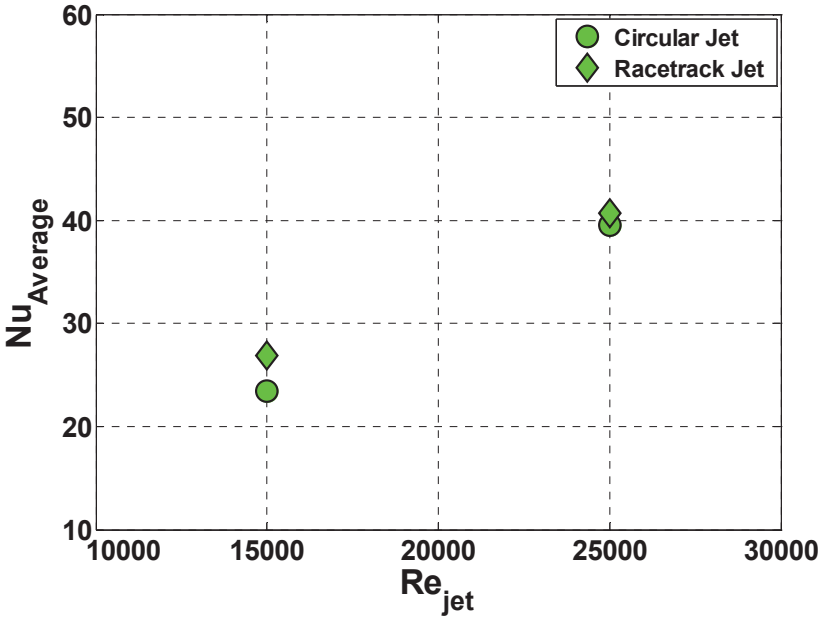

Figure 7.4: Surface averaged Nusselt number comparison.

In addition to comparing the stagnation region heat transfer, the overall surface average heat transfer was also examined. The overall surface average heat transfer for both a round and racetrack shaped jet is shown in Figure 7.4. The surface average is defined as the average heat transfer on all walls of the impingement surface (leading, stagnation, trailing) for a streamwise span of $x/d_{jet} = \pm 6$. Using this criterion, it is easily seen that racetrack shaped jets offer increased target surface heat transfer, in a surface averaged sense, at both Reynolds numbers investigated. This enhancement is a result of

the increased cross sectional area of the jet orifice, which offers better coverage of the target surface, as well as, provides a higher mass flow rate at a matching Reynolds number.

Rotating Heat Transfer

Now that the stationary results have been discussed, and a baseline established, the rotating impingement heat transfer trends can be presented. It must be noted that for all of the rotating results presented here, the regional Nusselt numbers are normalized by those obtained from the stationary cases. By normalizing the data, the enhancement due to rotation will be highlighted. The discussion will once again begin with the performance of a circular, square edged orifice. Figure 7.5 shows the performance of a circular jet at a jet Reynolds number of 15,000. Generally, it can be seen that as the rotation number increases, the heat transfer enhancement also increases. Per previous rotating investigations [35-37], one would expect that for radially inward flow, the leading wall of the impingement surface would experience the highest level of enhancement. However, this is not the trend being observed for these rotating cases. Instead, the opposite is true: the trailing wall of the impingement surface is receiving the highest enhancement, similar to what one would expect for radially outward rotating flows. One thing to keep in consideration is that even though, in this case, the trailing wall is seeing the greatest enhancement due to rotation, the actual Nusselt numbers in the stagnation region are greater than those seen on either the leading or trailing walls. Because the stagnation region Nusselt numbers are already very high due to the impinging jet, the additional mixing induced by rotational forces provides only marginal enhancement in these already elevated Nusselt numbers.

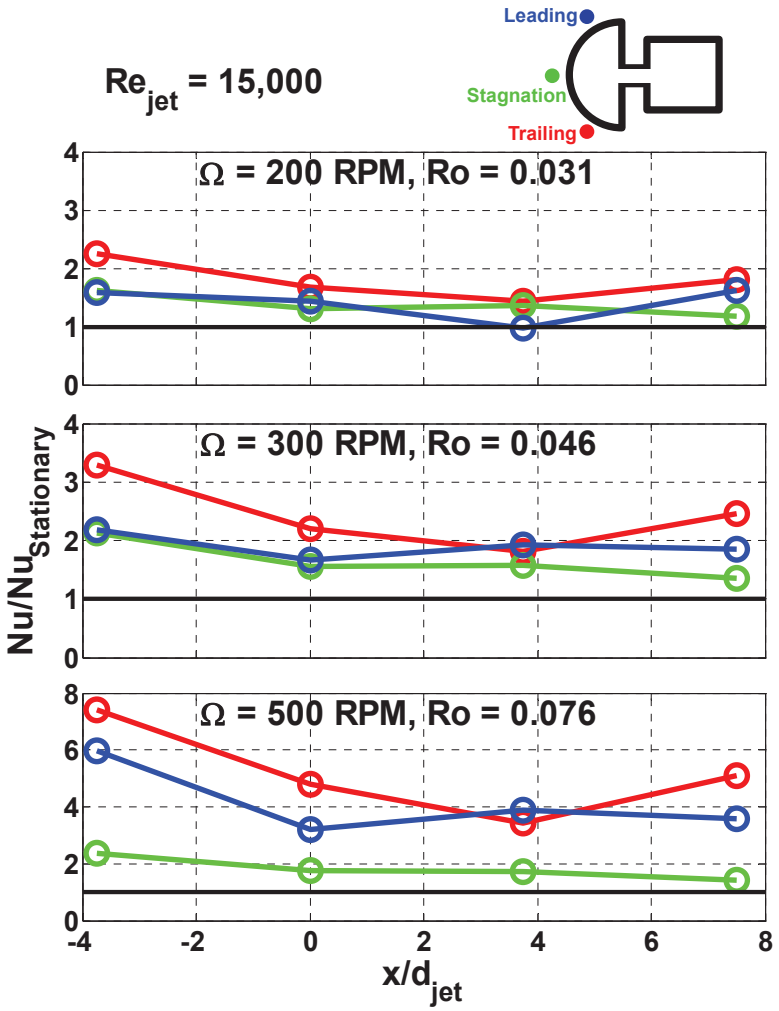

Figure 7.5: Streamwise Nusselt number enhancement at various rotational speeds with a circular jet (Re_{jet} = 15,000).

In an effort to explain the trend reversal (from what is expected based on rotating channel flow) observed in Figure 7.5, it is thought that the rotational effects from the supply channel, where the rotation numbers are much greater (varying from approximately 3 - 7.5, based on the supply channel fluid velocity and hydraulic diameter), are being carried through the jet orifice and continuing to enhance the trailing wall of the impingement surface. A critical distinction, however, is that instead of suffering from destructive performance on one wall of the impingement surface, heat transfer is being enhanced on all walls with the addition of rotation. Recall that the

purpose of using a single jet was to eliminate the effect of crossflow within the impingement cavity. If this is accomplished the bulk motion of the fluid cannot be considered to be radially inward. Due to this, it can be expected that a different heat transfer trend would be observed than for radially inward channel flow. It is hypothesized that the rotational effects seen by the fluid for the square supply channel (radially outward flow favoring the trailing wall) are being carried over through the jet to the impingement channel, due to the strong rotation effects on the supply side and relatively short jet length.

For the circular jet at a jet Reynolds number of 15,000, the trailing wall sees the highest enhancement at all rotation numbers. For the two slowest rotational speeds (Ro_{jet} = 0.031, 0.046), both the stagnation and leading walls feel approximately the same heat transfer enhancement upstream of the stagnation location: $-4 \leq x/d_{jet} \leq 0$. Downstream of the impingement location, the leading wall edges out an advantage over the stagnation region as the flow begins to flow more radially inward and the Coriolis forces begin to dominate. At the highest rotation number case (Ro_{jet} = 0.076), all walls of the impingement surface experience significant enhancement with the leading and trailing surfaces receiving the highest enhancement. At the location of impingement ($x/d_{jet} = 0$), for all rotational speeds, the trailing wall sees the highest enhancement followed by the leading and stagnation walls, respectively. In the region upstream of the jet ($-4 \leq x/d_{jet} \leq 0$), even higher levels of heat transfer enhancement are witnessed, up to approximately 7.5 times the level of heat transfer observed in the stationary channel for the trailing surface. It is conjectured that this increase is caused by increased mixing due to the higher rotation numbers. Within the test section, a "dead zone" exists upstream of the

impinging jet. In the stationary tests, the coolant becomes stagnant in this region, and heat transfer performance is severely restricted. However, under rotating conditions, mixing currents are induced, and the previously trapped, stagnant coolant begins to move and improve the heat transfer characteristics in this region. Therefore, the Nusselt numbers in this region are greatly enhanced over what was observed in the stationary channel.

The effect of a circular jet at the higher jet Reynolds number of 25,000 is shown in Figure 7.6. The effect of rotation in these tests is limited due to the increased fluid velocity through the test section. The same rotational speeds are tested, however, lower rotation numbers are obtained as a result of the increased flow velocity. Thus, as one would expect, the effect of rotation is diminished. For the rotation numbers of 0.018 and 0.027, it is clear that the level of enhancement encountered is reduced compared to what was seen for the same rotational speeds for the lower Reynolds number. For the stagnation and trailing surfaces, the enhancement falls between approximately one and two. The leading surface, however, holds around one, and begins to show a destructive interaction along the stagnation region. This could be due to the jet deflecting away from the stagnation surface and toward the trailing wall of the impingement cavity. Enhancement is not seen in the stagnation region until the rotation number increases further, providing more rotation induced mixing. At this higher Reynolds number, for a rotation number of 0.046 there is significant enhancement to the heat transfer, compared to that offered at the two lower rotation numbers.

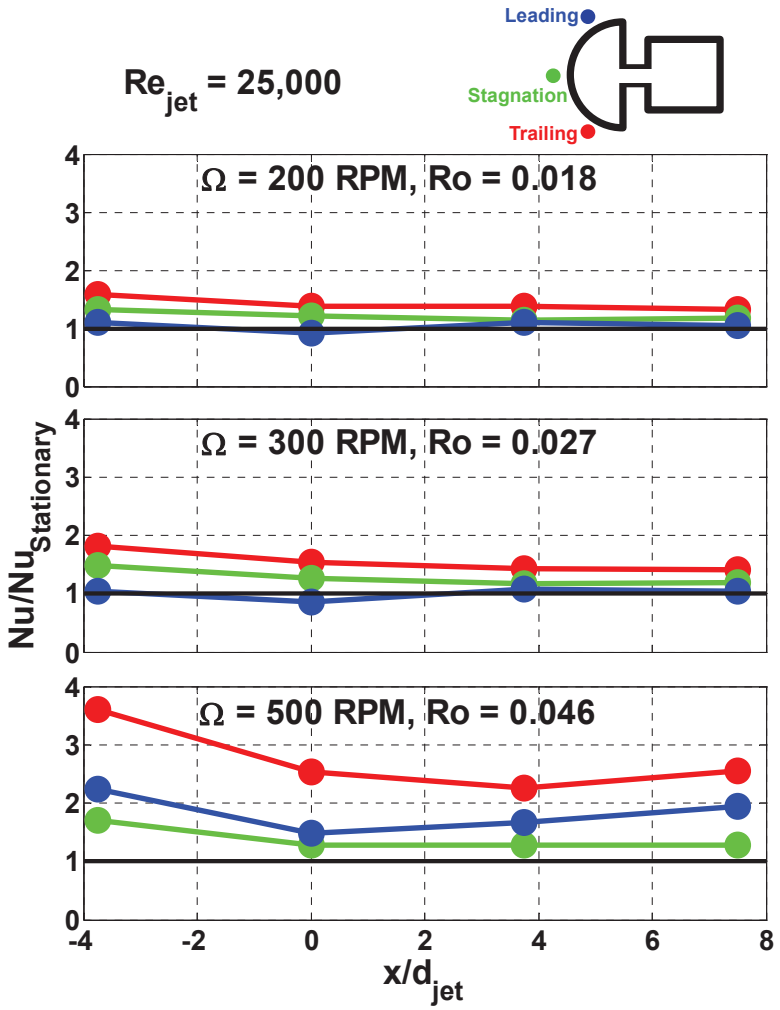

Figure 7.6: Streamwise Nusselt number enhancement at various rotational speeds with a circular jet (Re_{jet} = 25,000).

This sudden jump in the enhancement could be indicative that a critical rotation number has been breached, where significant heat transfer enhancement is observed on all surfaces of the impingement cavity. For all cases, plate 6 (x/d_{jet} = -4, on each respective wall) upstream of the impinging jet, experiences the greatest enhancement. This is particularly evident as the rotation number increases beyond a value of 0.030. Once the rotation number increases beyond this value, the buoyancy driven secondary flows begin to dominate. The region upstream of the jet (previously referred to as the "dead zone") greatly benefits from the increased buoyancy driven flows. These buoyancy

driven flows prevent the spend impingement air from stagnating in this dead region and limiting the heat transfer. Additionally, it is interesting to compare the two cases with identical rotation numbers. For a rotation number of 0.046 a similar trend is observed at both Reynolds numbers. Further, the level of heat transfer enhancement at each streamwise location is nearly identical in the two cases. These results suggest a direct correlation between the rotation number and heat transfer enhancement due to rotation.

Figures 7.7 and 7.8 provide streamwise Nusselt number ratio distributions for the racetrack shaped jets. From the streamwise regional Nusselt number ratios, it is clear enhancement when moving to the racetrack jet from the circular jet. For the racetrack jet, at a Reynolds number of 15,000, heat transfer enhancement occurs on all walls of the impingement surface, and continues to increase with increasing rotation number. At the highest rotation number tested (Ro_{jet} = 0.076), there is tremendous enhancement present upstream of the impinging jet (x/d_{jet} = -4). The leading and trailing walls both provide nearly seven times the heat transfer that was seen for the stationary channel. Furthermore, for all rotation numbers, the enhancement observed on the leading and trailing surfaces is very similar for a racetrack jet, whereas, for a circular jet, the trailing wall always experienced the highest level of enhancement. This indicates that the racetrack shaped jet is providing more uniform coverage of the target surface, and is resisting any buoyancy driven forces from deflecting the jet. Due to this improved coverage, the racetrack jet tends to provide higher average enhancement than the circular jet.

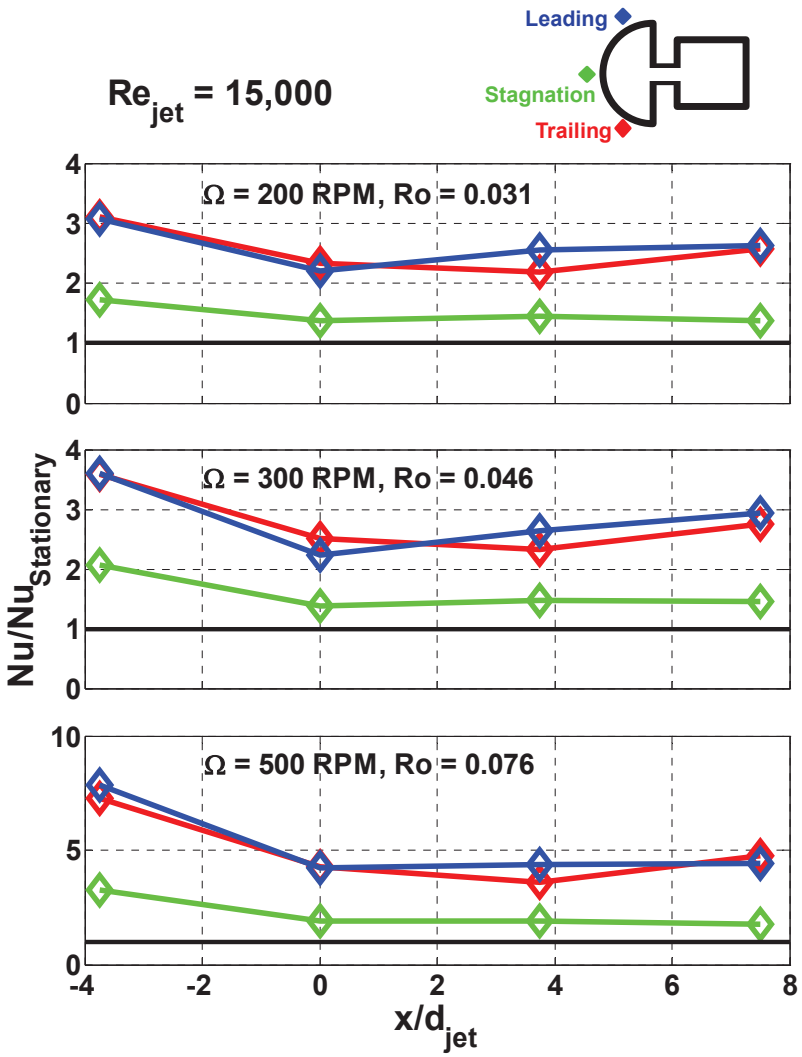

Figure 7.7: Streamwise Nusselt number enhancement at various rotational speeds with a racetrack jet (Re_{jet} = 15,000).

Moving to the higher Reynolds number for the racetrack jet, there is again enhancement on all surfaces. There is still decreased enhancement compared to the lower Reynolds numbers cases at the same rotational speeds. Recall that, at a specified rotational speed, increasing the Reynolds number decreases the effect of rotation. Referring back to Equation 5.1, if the velocity of the fluid increases and the rotational speed remains constant, the effect of rotation will be lessened due to this decreased relative rotational speed. The trend previously observed with the racetrack shaped jet of

increasing enhancement on the leading wall downstream of the impingement location is once again seen here at the higher Reynolds number of 25,000.

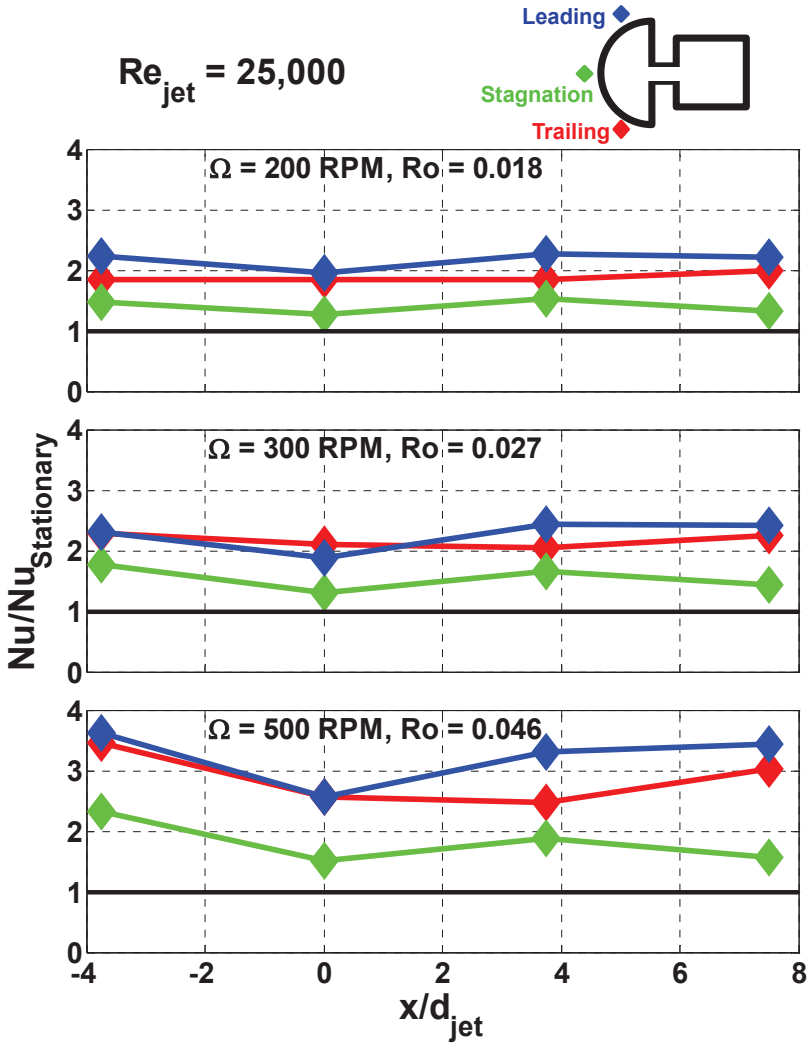

Figure 7.8: Streamwise Nusselt number enhancement at various rotational speeds with a racetrack jet (Re_{jet} = 25,000).

It is also necessary to discuss the heat transfer enhancement trends as a function of rotation number. This relative velocity parameter can provide valuable insight into how the coolant behaves under various levels of rotational persuasion. Figures 7.9 and 7.10 show the heat transfer enhancement results as a function of the rotation number for a circular jet and racetrack jet, respectively. The values presented in these figures are taken

from the stagnation region copper plates (x/d_{jet} = 0) for each respective wall in the impingement channel. Starting with the circular jet, at rotation numbers below the critical value of 0.030, the trailing wall sees the greatest heat transfer enhancement followed by the stagnation surface. Heat transfer on the leading wall, at these low rotation numbers, is not enhanced, but rather, is degraded. As the rotation parameter increases beyond 0.030, enhancement on the leading surface surpasses that seen on the stagnation surface due to increased mixing within the impingement cavity. The strength of the rotation induced mixing vortices continues to increase with increased rotation. As a result, the heat transfer enhancement on the leading and trailing impingement surfaces will also continue to increase, although at different rates. It is worth noting that at a rotation number of 0.046, values at two separate Reynolds numbers are represented: Re_{jet} = 15,000, Ω = 300 RPM and Re_{jet} = 25,000, Ω = 500 RPM.

Similar to what was seen for the circular jet, the racetrack jet demonstrates the same spreading pattern with increasing rotation. However, one key difference is that, for a racetrack jet, the leading and trailing walls experience approximately the same level of enhancement at a given rotation number. This trend would prove to be tremendously beneficial in the leading edge of a turbine blade, as any temperature gradients would be minimized. The improved performance of the racetrack jet is further demonstrated in Figure 7.11. The increased enhancement offered by the racetrack jet is highlighted using a circumferential average of the leading, stagnation and trailing walls at the stagnation point (x/d_{jet} = 0). At every rotation number, the racetrack jet provides a significant advantage over its circular counterpart.

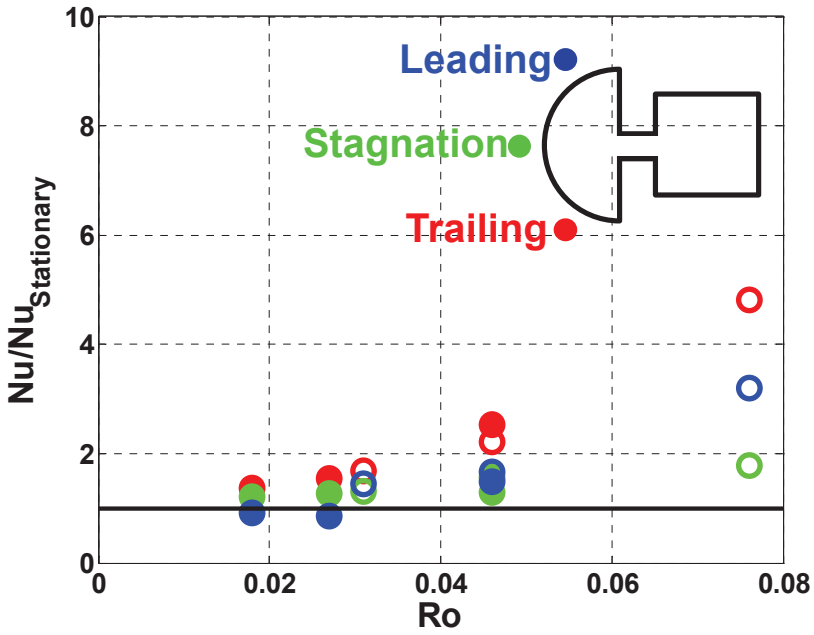

Figure 7.9: Stagnation point ($x/d_{jet} = 0$), Nusselt number enhancement for the circular jet as a function of rotation number.

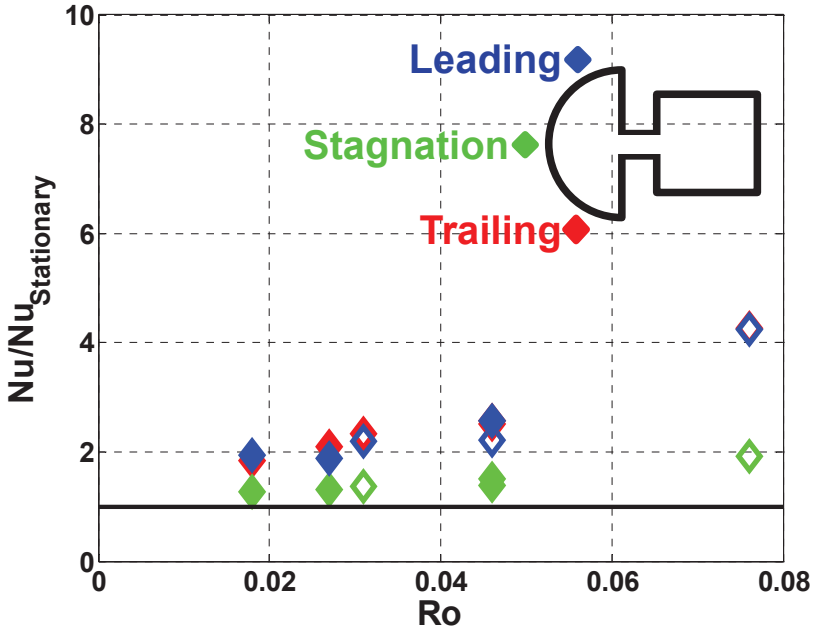

Figure 7.10: Stagnation point ($x/d_{jet} = 0$), Nusselt number enhancement for the racetrack jet as a function of rotation number.

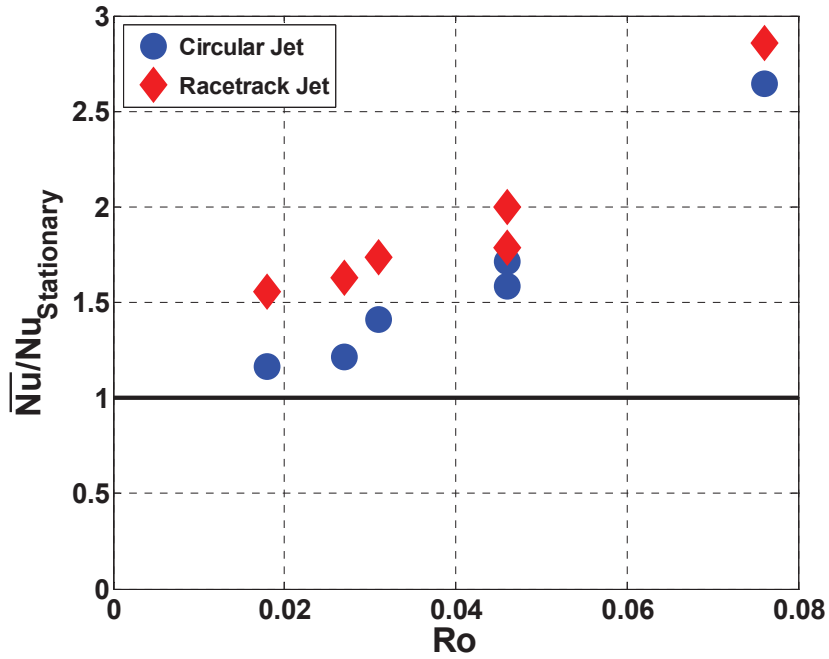

Figure 7.11: Comparison of the circumferential averaged Nusselt number ratios (leading, stagnation, and trailing) at $x/d_{jet} = 0$ for the circular and racetrack jets.

Figure 7.12 and Figure 7.13 present the Nusselt number ratios as a function of the buoyancy number instead of the rotation number. The trend observed is very similar to that seen for the rotation number figures. As the buoyancy number increases, heat transfer is enhanced on all surfaces for both jet shapes. This is good news for engine designers to see enhancement on all surfaces at high rotation and buoyancy numbers. With the current study considering rotation and buoyancy number much higher than those currently available in open literature, the enhancement due to high rotation effects is clearly seen. Previous works by Parsons and Han [53] and Lamont and Ekkad [59] show rotation to be destructive to an impinging jet on the leading or trailing surface, and in some cases both (depending on the orientation of the jet in relation to the direction of rotation). However, these studies only considered rotation numbers up to 0.01, which is well below the critical value of 0.030 observed in this study. Parsons and Han [53]

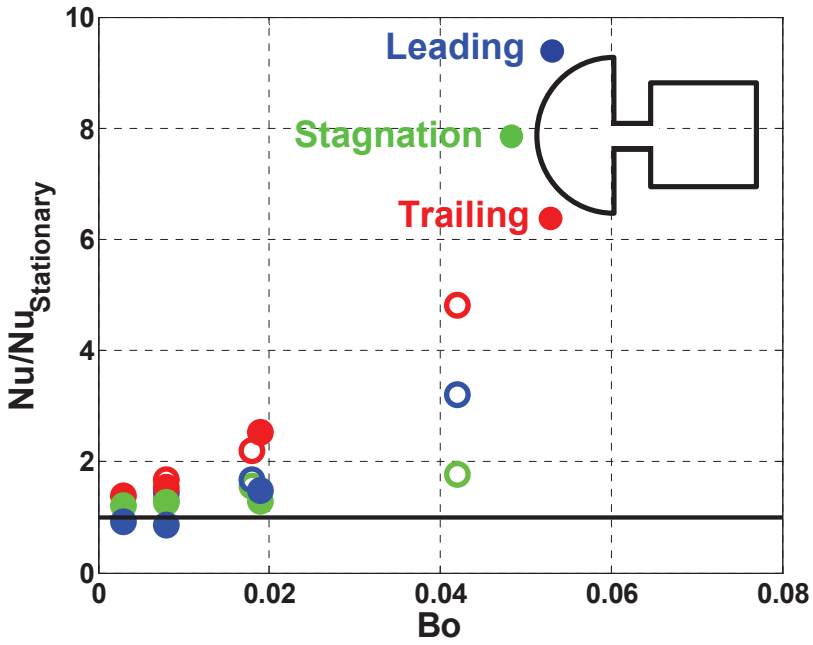

Figure 7.12: Stagnation point ($x/d_{jet} = 0$), Nusselt number enhancement for the circular jet as a function of buoyancy number.

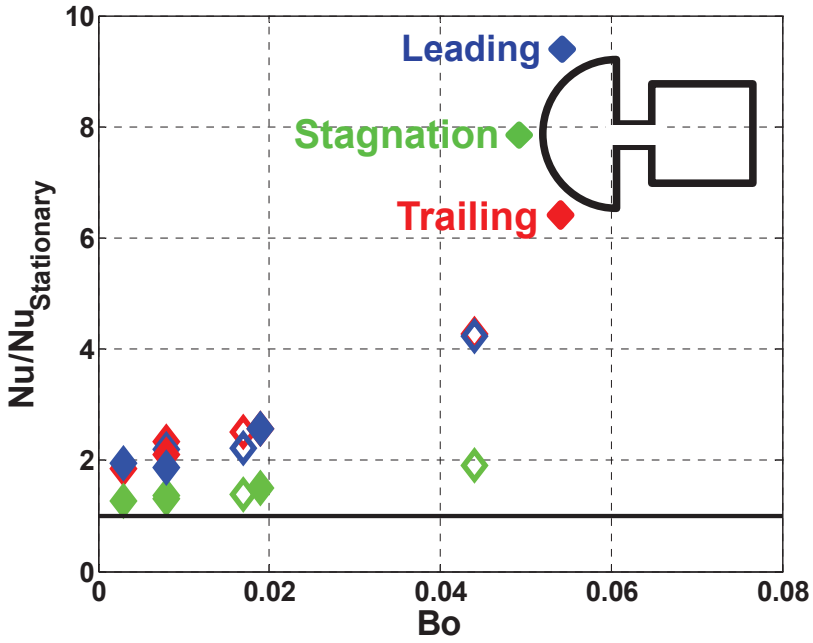

Figure 7.13: Stagnation point ($x/d_{jet} = 0$), Nusselt number enhancement for the racetrack jet as a function of buoyancy number.

showed an increase in the Nusselt numbers on the leading surface at rotation numbers up to 0.003. Compared to these studies, the current investigation examined significantly higher rotation and buoyancy numbers, and heat transfer enhancement is encountered on all impingement surfaces once the critical rotation number of 0.030 is surpassed.

CHAPTER EIGHT

Conclusions

Stationary Heat Transfer

This investigation observed the heat transfer trends associated with leading edge jet impingement were impacted under varying jet shape, jet edge condition, jet-to-jet spacing, jet length, and supply flow conditions. Using a classic, steady state copper plate technique, regionally averaged Nusselt numbers were obtained for the curved target surface. Many of these varying parameters were chosen to model imperfections in parts due to manufacturing limitations to determine the effect of elongated impingement jets and jets without square edge orifices. In this study, circular, square edge orifices were used to establish a baseline for comparison of the new geometries. Further, the effect of radial bypass flow was investigated to determine the impingement characteristics under high inlet crossflow velocities.

In general, for jets with a thickness of 1.33 diameters, the racetrack shaped jet just slightly outperforms the circular jet at a given mass flow rate for no radial bypass cases. Of these, the square edge, racetrack jet provides the highest stagnation average heat transfer. However, once filleted edges are introduced, the racetrack jet is challenged by a circular fully filleted jet at the lowest Reynolds number. This is somewhat surprising, as the addition of filleted edges typically has a negative effect on the target surface heat transfer. With the addition of radial bypass supply conditions, the square edge jets perform far better, as they possess the ability to reorient the jet flow back perpendicular to the target surface. The filleted jets, on the other hand, suffer greatly under bypass

conditions, in some cases allowing the jet to deflect a full two diameters downstream of the intended impingement location. By introducing jets 2.5 diameters in length, the deflection of the jet was eliminated; however, this came at a cost of slightly reduced target surface heat transfer. Further, jets with a length of four diameters generally saw further reduced target surface Nusselt numbers than the shorter jets, particularly at the higher Reynolds numbers. Little time was spent investigating the effect of jet-to-jet spacing; however, it was enough to show the increased heat transfer performance associated with moving the jets closer together. Though this improved performance comes at a cost of using the same mass flow rate to cool an area half of the size.

Rotating Heat Transfer

The rotating heat transfer study set out to determine the effect of rotation, and jet shape on leading edge impingement heat transfer. For all cases shown here, the addition of rotation further enhanced the heat transfer on all walls of the rotating impingement channel. Furthermore, as rotation increased, so did the heat transfer within the channel due to the increased mixing induced by rotation. It was also shown that the use of racetrack shaped jets provides increased enhancement at all rotation numbers. In addition, the racetrack shaped jet provided more uniform enhancement of the heat transfer which would lead to reduced thermal stresses within the leading edge of the turbine blade by reducing the formation of large temperature gradients.

Future Recommendations

The current investigations, on several occasions made direct comparisons to Chupp et al. [14]; however, based on the unique geometries currently being investigated there is a great need for a correlation that accounts for conditions such as edge filleting and aspect ratio. Elston [62] developed such a correlation using computational data, and this correlation should be supplemented with the experimental data presented here. Additional work is also necessary to shed light on the effects of decreased jet-to-jet spacing at the various jet length and relative fillet radii.

The rotating study would benefit from introducing additional jets into the impingement cavity to determine the effect of jet to jet interaction under rotating conditions. The groundwork has been laid by investigating the simplest case possible, in a single jet, and now that can be built on by investigating multiple jets. Further, a scheme needs to be developed to monitor all copper plates within the rotating test section. Increasing the number of data points may be the first step in obtaining more meaningful data from the apparatus.

APPENDICES

APPENDIX A

Jet Plate Drawings

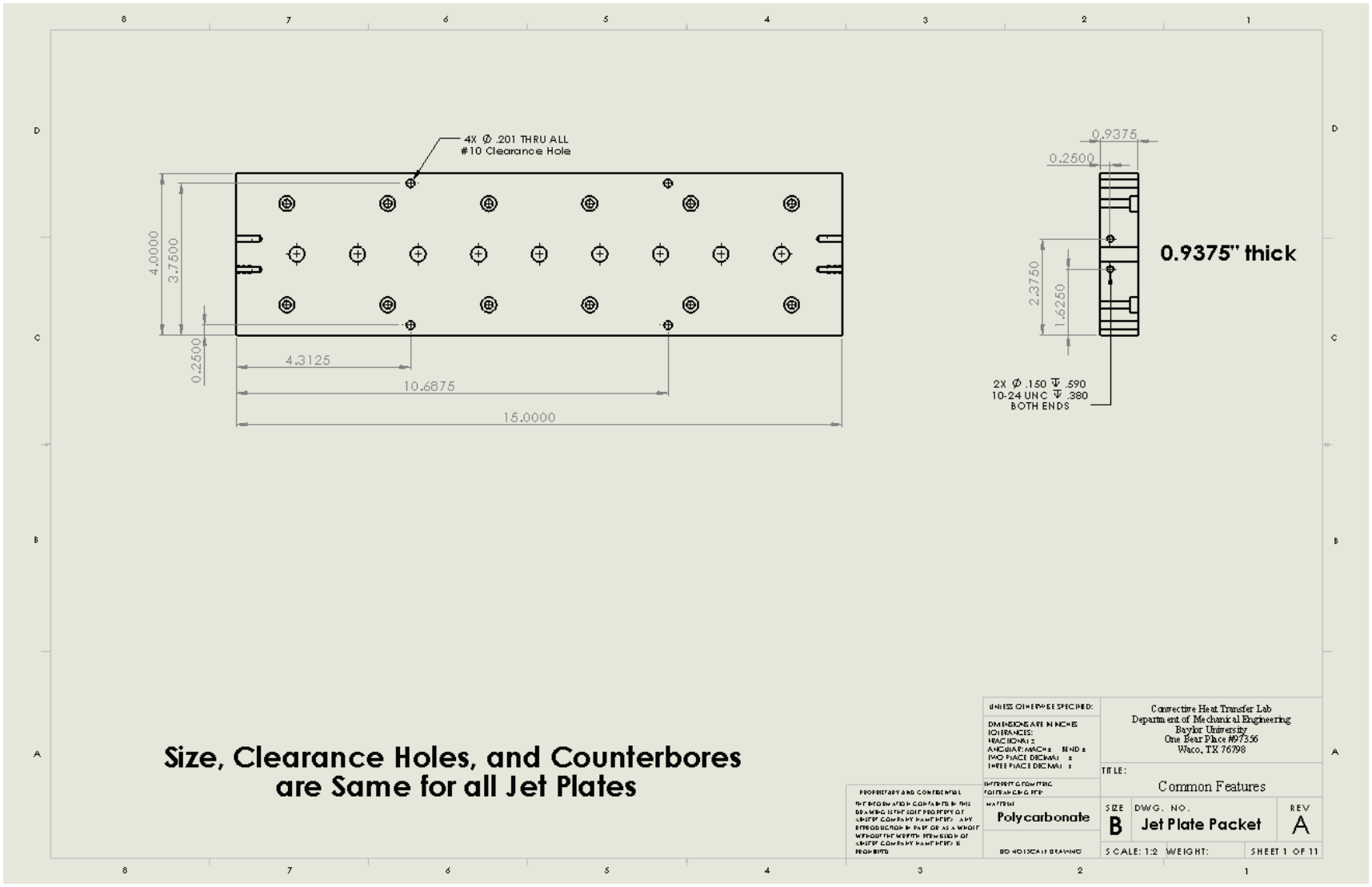
4X Ø .201 THRU ALL
#10 Clearance Hole
4.0000
3.7500
0.2500
4.3125
10.6875
15.0000
0.9375
0.2500
2.3750
1.6250
0.9375" thick
2X Ø .150 ↧ .590
10-24 UNC ↧ .380
BOTH ENDS
Size, Clearance Holes, and Counterbores
are Same for all Jet Plates
UNLESS OTHERWISE SPECIFIED:
DIMENSIONS ARE IN INCHES
TOLERANCES:
FRACTIONAL ±
ANGULAR: MACH ± BEND ±
TWO PLACE DECIMAL ±
THREE PLACE DECIMAL ±
INTERPRET GEOMETRIC
TOLERANCING PER:
MATERIAL
Polycarbonate
DO NOT SCALE DRAWING
PROPRIETARY AND CONFIDENTIAL
THE INFORMATION CONTAINED IN THIS DRAWING IS THE SOLE PROPERTY OF <INSERT COMPANY NAME HERE>. ANY REPRODUCTION IN PART OR AS A WHOLE WITHOUT THE WRITTEN PERMISSION OF <INSERT COMPANY NAME HERE> IS PROHIBITED
Convective Heat Transfer Lab
Department of Mechanical Engineering
Baylor University
One Bear Place #97356
Waco, TX 76798
TITLE:
Common Features
SIZE
B
DWG. NO.
Jet Plate Packet
REV
A
SCALE: 1:2
WEIGHT:
SHEET 1 OF 11

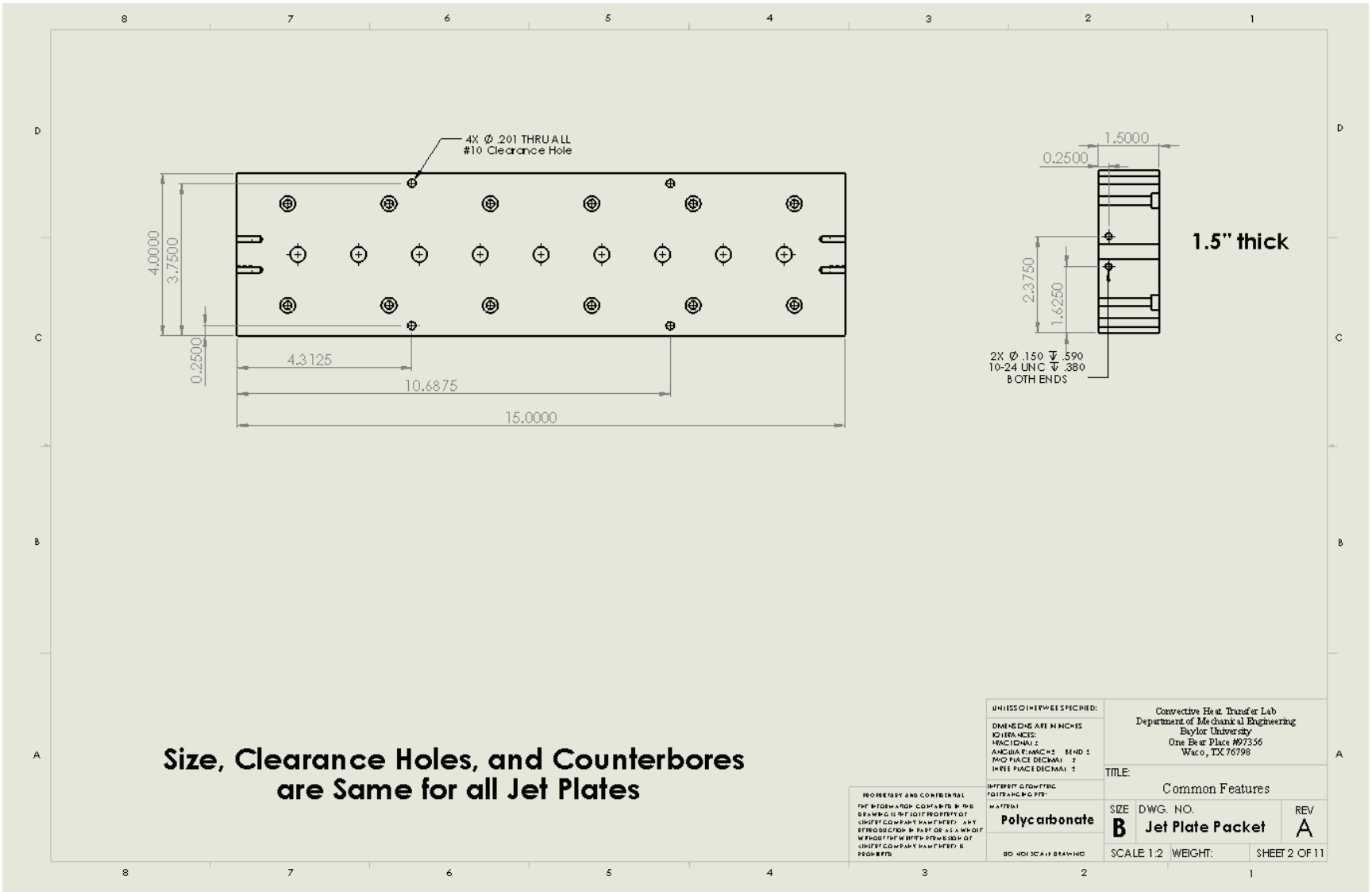
4X Ø .201 THRU ALL
#10 Clearance Hole
4.0000
3.7500
0.2500
4.3125
10.6875
15.0000
1.5000
0.2500
2.3750
1.6250
2X Ø .150 ↧ .590
10-24 UNC ↧ .380
BOTH ENDS
1.5" thick
Size, Clearance Holes, and Counterbores are Same for all Jet Plates
UNLESS OTHERWISE SPECIFIED:
DIMENSIONS ARE IN INCHES
TOLERANCES:
FRACTIONAL ±
ANGULAR: MACH ± BEND ±
TWO PLACE DECIMAL ±
THREE PLACE DECIMAL ±
INTERPRET GEOMETRIC TOLERANCING PER:
MATERIAL
Polycarbonate
DO NOT SCALE DRAWING
PROPRIETARY AND CONFIDENTIAL
THE INFORMATION CONTAINED IN THIS DRAWING IS THE SOLE PROPERTY OF <INSERT COMPANY NAME HERE>. ANY REPRODUCTION IN PART OR AS A WHOLE WITHOUT THE WRITTEN PERMISSION OF <INSERT COMPANY NAME HERE> IS PROHIBITED.
Convective Heat Transfer Lab
Department of Mechanical Engineering
Baylor University
One Bear Place #97356
Waco, TX 76798
TITLE:
Common Features
SIZE B
DWG. NO. Jet Plate Packet
REV A
SCALE 1:2
WEIGHT:
SHEET 2 OF 11

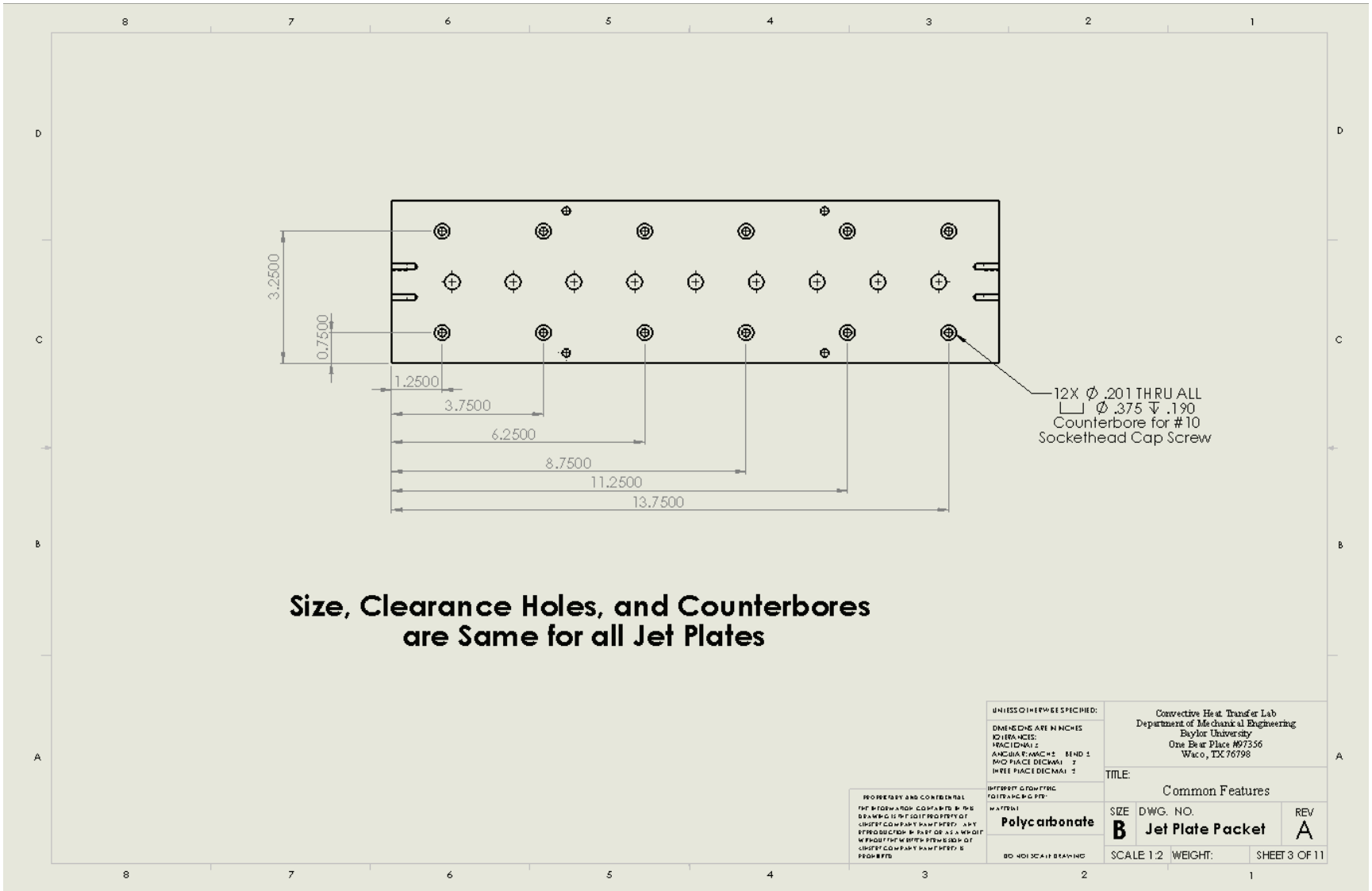
3.2500
0.7500
1.2500
3.7500
6.2500
8.7500
11.2500
13.7500
12X Ø .201 THRU ALL
⌴ Ø .375 ↧ .190
Counterbore for #10
Sockethead Cap Screw
Size, Clearance Holes, and Counterbores
are Same for all Jet Plates
UNLESS OTHERWISE SPECIFIED:
DIMENSIONS ARE IN INCHES
TOLERANCES:
FRACTIONAL ±
ANGULAR: MACH ± BEND ±
TWO PLACE DECIMAL ±
THREE PLACE DECIMAL ±
INTERPRET GEOMETRIC TOLERANCING PER:
MATERIAL
Polycarbonate
DO NOT SCALE DRAWING
PROPRIETARY AND CONFIDENTIAL
THE INFORMATION CONTAINED IN THIS DRAWING IS THE SOLE PROPERTY OF <INSERT COMPANY NAME HERE>. ANY REPRODUCTION IN PART OR AS A WHOLE WITHOUT THE WRITTEN PERMISSION OF <INSERT COMPANY NAME HERE> IS PROHIBITED
Convective Heat Transfer Lab
Department of Mechanical Engineering
Baylor University
One Bear Place #97356
Waco, TX 76798
TITLE:
Common Features
SIZE B
DWG. NO. Jet Plate Packet
REV A
SCALE 1:2
WEIGHT:
SHEET 3 OF 11

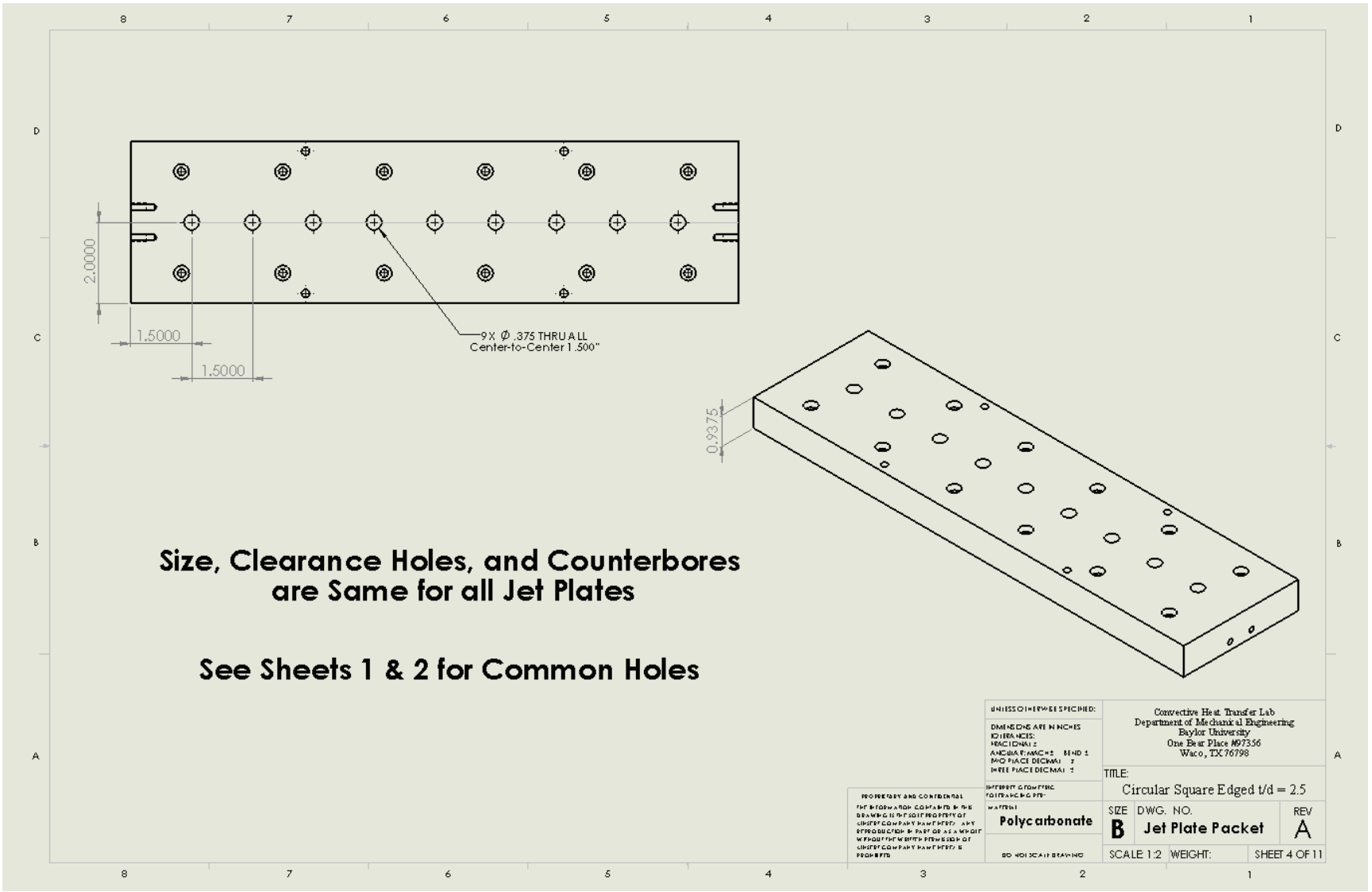
2.0000
1.5000
1.5000
9X Ø .375 THRU ALL
Center-to-Center 1.500"
0.9375
Size, Clearance Holes, and Counterbores
are Same for all Jet Plates
See Sheets 1 & 2 for Common Holes
UNLESS OTHERWISE SPECIFIED:
DIMENSIONS ARE IN INCHES
TOLERANCES:
FRACTIONAL ±
ANGULAR: MACH ± BEND ±
TWO PLACE DECIMAL ±
THREE PLACE DECIMAL ±
INTERPRET GEOMETRIC TOLERANCING PER:
MATERIAL
Polycarbonate
DO NOT SCALE DRAWING
PROPRIETARY AND CONFIDENTIAL
THE INFORMATION CONTAINED IN THIS DRAWING IS THE SOLE PROPERTY OF <INSERT COMPANY NAME HERE>. ANY REPRODUCTION IN PART OR AS A WHOLE WITHOUT THE WRITTEN PERMISSION OF <INSERT COMPANY NAME HERE> IS PROHIBITED.
Convective Heat Transfer Lab
Department of Mechanical Engineering
Baylor University
One Bear Place #97356
Waco, TX 76798
TITLE:
Circular Square Edged t/d = 2.5
SIZE
B
DWG. NO.
Jet Plate Packet
REV
A
SCALE 1:2
WEIGHT:
SHEET 4 OF 11

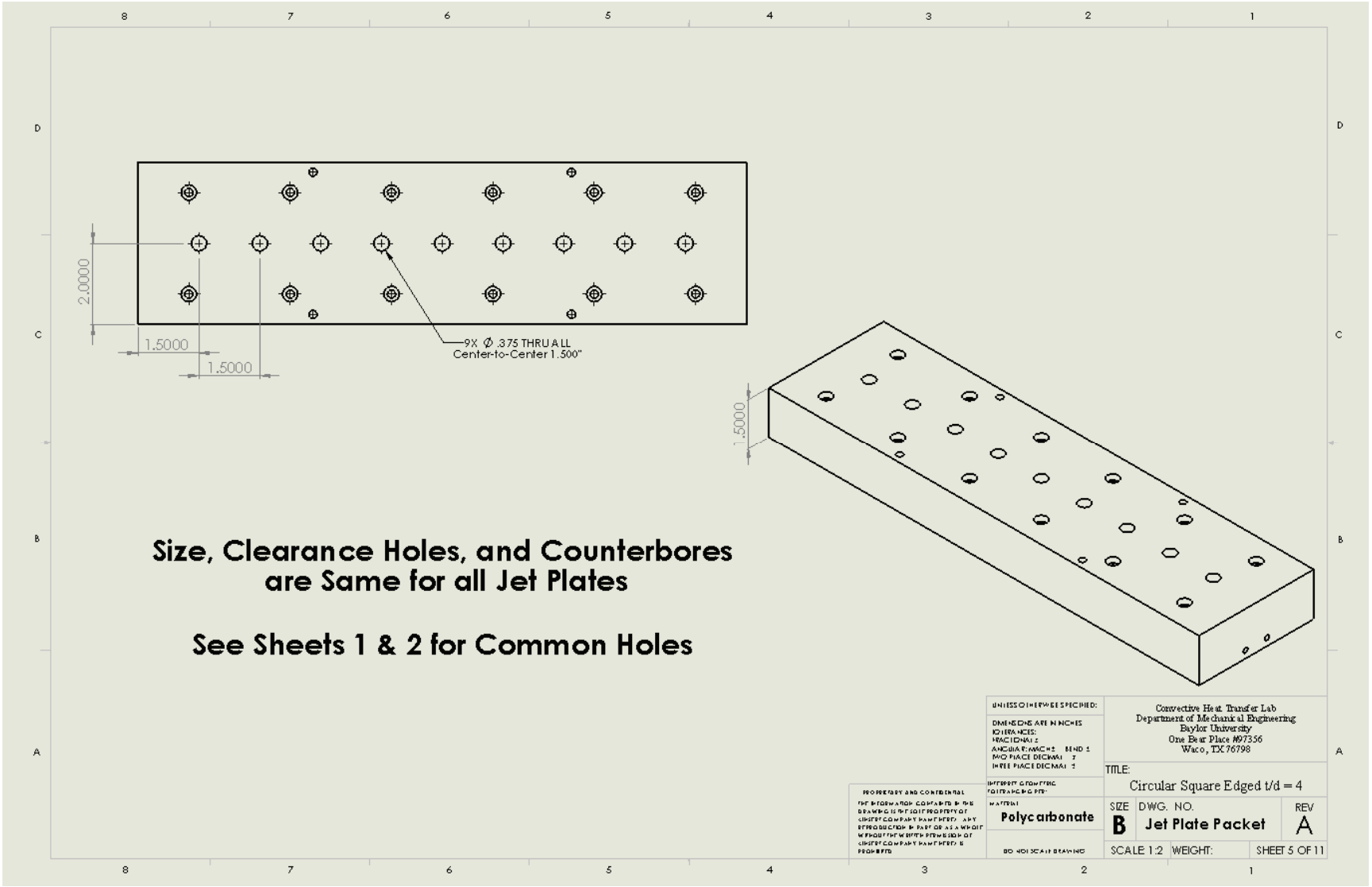
2.0000
1.5000
1.5000
9X Ø .375 THRU ALL
Center-to-Center 1.500"
1.5000
Size, Clearance Holes, and Counterbores
are Same for all Jet Plates
See Sheets 1 & 2 for Common Holes
UNLESS OTHERWISE SPECIFIED:
DIMENSIONS ARE IN INCHES
TOLERANCES:
FRACTIONAL ±
ANGULAR: MACH ± BEND ±
TWO PLACE DECIMAL ±
THREE PLACE DECIMAL ±
INTERPRET GEOMETRIC TOLERANCING PER:
MATERIAL
Polycarbonate
DO NOT SCALE DRAWING
PROPRIETARY AND CONFIDENTIAL
THE INFORMATION CONTAINED IN THIS DRAWING IS THE SOLE PROPERTY OF <INSERT COMPANY NAME HERE>. ANY REPRODUCTION IN PART OR AS A WHOLE WITHOUT THE WRITTEN PERMISSION OF <INSERT COMPANY NAME HERE> IS PROHIBITED.
Convective Heat Transfer Lab
Department of Mechanical Engineering
Baylor University
One Bear Place #97356
Waco, TX 76798
TITLE:
Circular Square Edged t/d = 4
SIZE
B
DWG. NO.
Jet Plate Packet
REV
A
SCALE 1:2
WEIGHT:
SHEET 5 OF 11

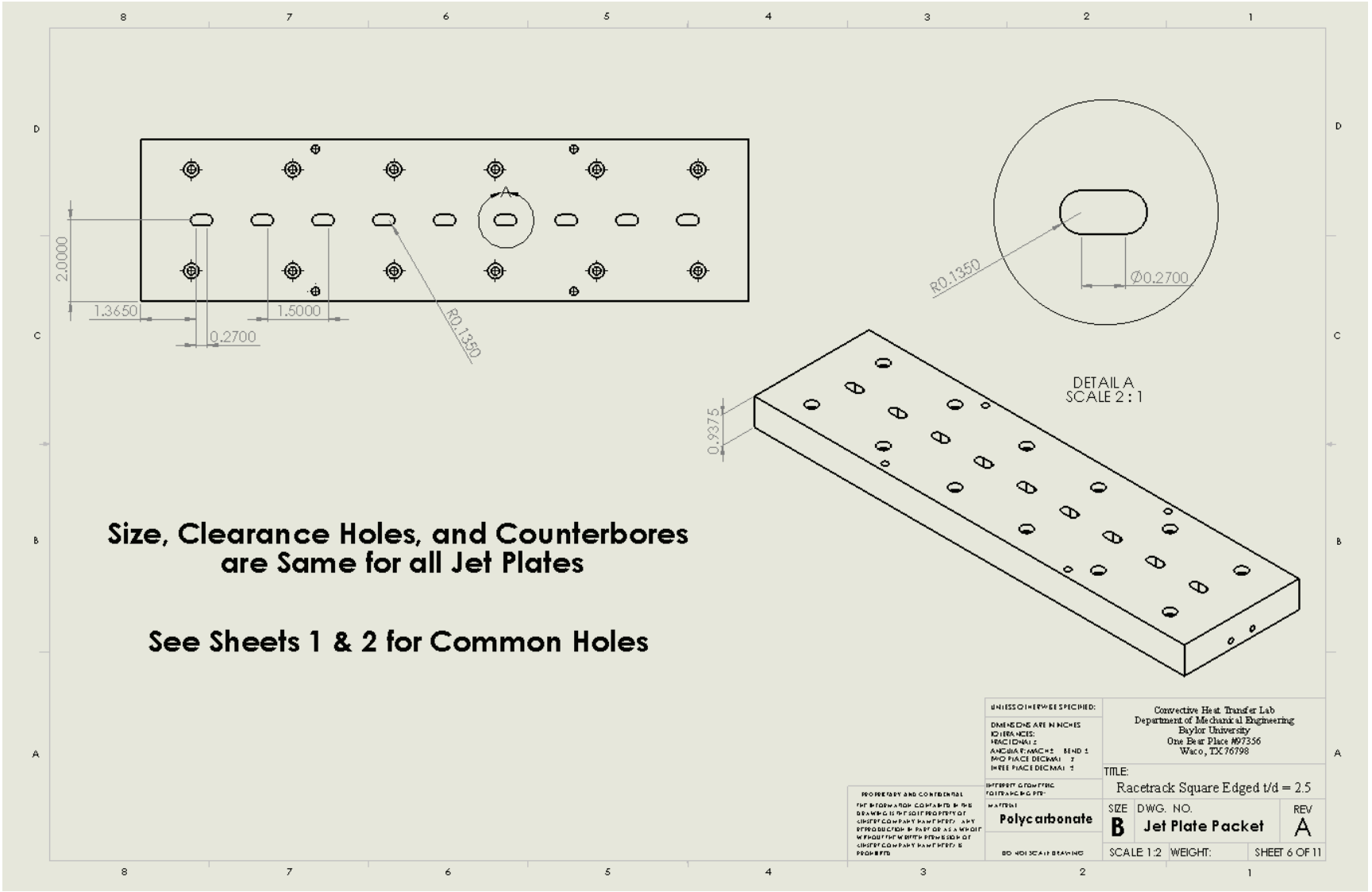
2.0000
1.3650
1.5000
0.2700
R0.1350
R0.1350
Ø0.2700
DETAIL A
SCALE 2 : 1
0.9375
Size, Clearance Holes, and Counterbores
are Same for all Jet Plates
See Sheets 1 & 2 for Common Holes
UNLESS OTHERWISE SPECIFIED:
DIMENSIONS ARE IN INCHES
TOLERANCES:
FRACTIONAL ±
ANGULAR: MACH ± BEND ±
TWO PLACE DECIMAL ±
THREE PLACE DECIMAL ±
INTERPRET GEOMETRIC TOLERANCING PER:
MATERIAL
Polycarbonate
DO NOT SCALE DRAWING
PROPRIETARY AND CONFIDENTIAL
THE INFORMATION CONTAINED IN THIS DRAWING IS THE SOLE PROPERTY OF <INSERT COMPANY NAME HERE>. ANY REPRODUCTION IN PART OR AS A WHOLE WITHOUT THE WRITTEN PERMISSION OF <INSERT COMPANY NAME HERE> IS PROHIBITED.
Convective Heat Transfer Lab
Department of Mechanical Engineering
Baylor University
One Bear Place #97356
Waco, TX 76798
TITLE:
Racetrack Square Edged t/d = 2.5
SIZE
B
DWG. NO.
Jet Plate Packet
REV
A
SCALE: 1:2
WEIGHT:
SHEET 6 OF 11

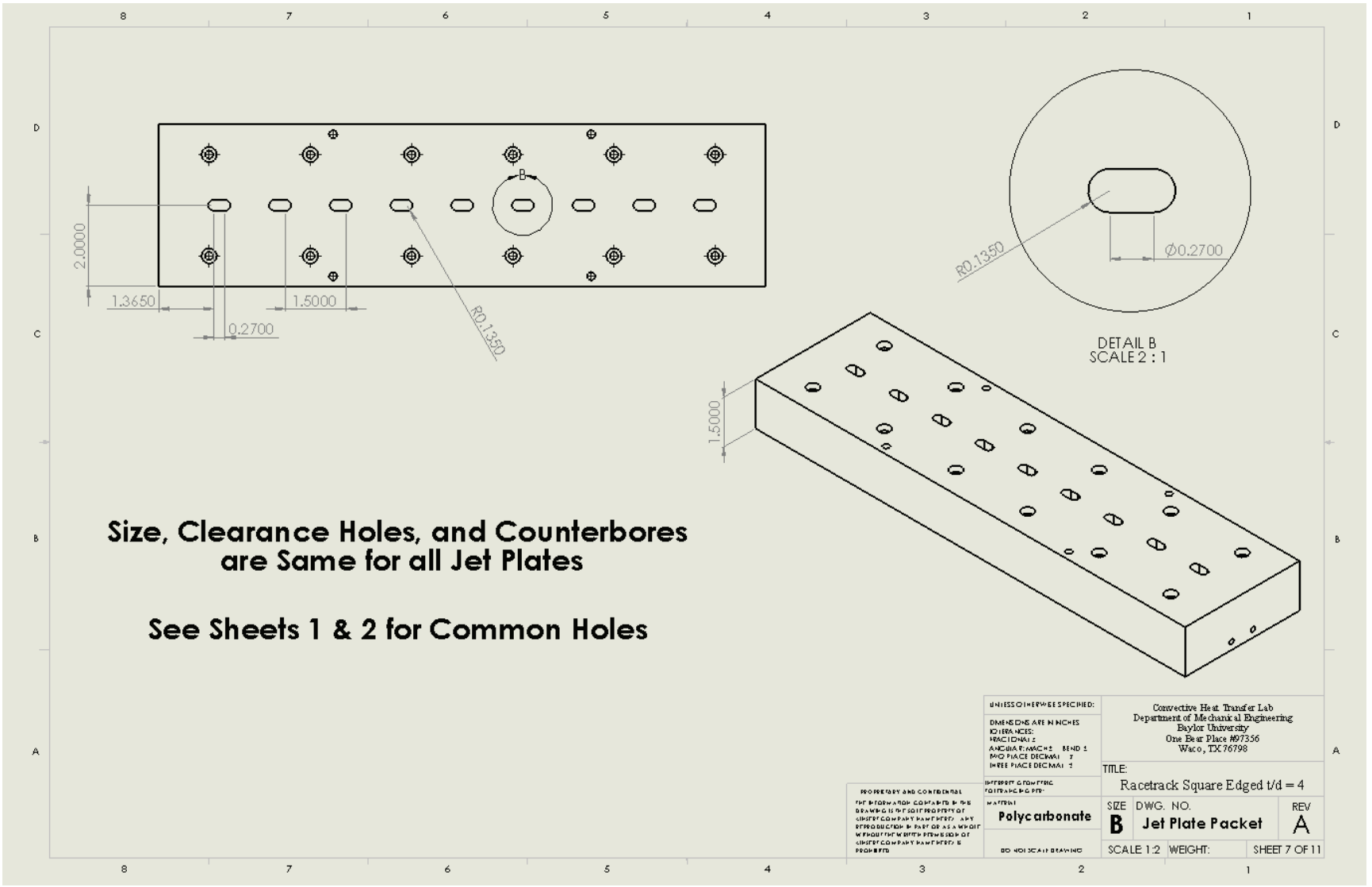
2.0000
1.3650
1.5000
0.2700
R0.1350
B
R0.1350
Ø0.2700
DETAIL B
SCALE 2 : 1
1.5000
Size, Clearance Holes, and Counterbores
are Same for all Jet Plates
See Sheets 1 & 2 for Common Holes
UNLESS OTHERWISE SPECIFIED:
DIMENSIONS ARE IN INCHES
TOLERANCES:
FRACTIONAL ±
ANGULAR: MACH ± BEND ±
TWO PLACE DECIMAL ±
THREE PLACE DECIMAL ±
INTERPRET GEOMETRIC TOLERANCING PER:
MATERIAL
Polycarbonate
DO NOT SCALE DRAWING
PROPRIETARY AND CONFIDENTIAL
THE INFORMATION CONTAINED IN THIS DRAWING IS THE SOLE PROPERTY OF <INSERT COMPANY NAME HERE>. ANY REPRODUCTION IN PART OR AS A WHOLE WITHOUT THE WRITTEN PERMISSION OF <INSERT COMPANY NAME HERE> IS PROHIBITED.
Convective Heat Transfer Lab
Department of Mechanical Engineering
Baylor University
One Bear Place #97356
Waco, TX 76798
TITLE:
Racetrack Square Edged t/d = 4
SIZE
B
DWG. NO.
Jet Plate Packet
REV
A
SCALE: 1:2
WEIGHT:
SHEET 7 OF 11

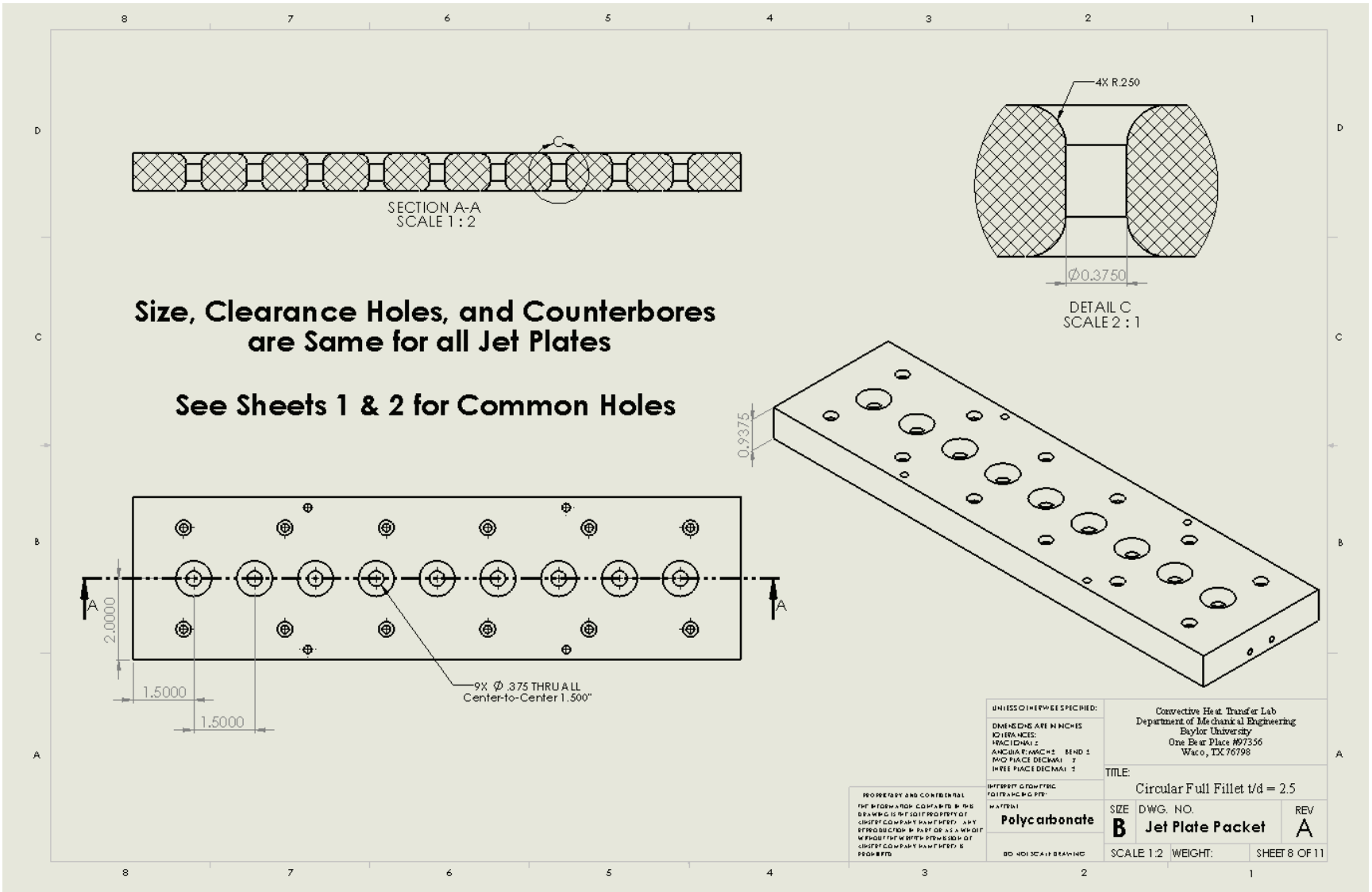
SECTION A-A
SCALE 1 : 2
4X R.250
Ø0.3750
DETAIL C
SCALE 2 : 1
Size, Clearance Holes, and Counterbores
are Same for all Jet Plates
See Sheets 1 & 2 for Common Holes
0.9375
2.0000
1.5000
1.5000
9X Ø .375 THRU ALL
Center-to-Center 1.500"
A
A
UNLESS OTHERWISE SPECIFIED:
DIMENSIONS ARE IN INCHES
TOLERANCES:
FRACTIONAL ±
ANGULAR: MACH ± BEND ±
TWO PLACE DECIMAL ±
THREE PLACE DECIMAL ±
INTERPRET GEOMETRIC TOLERANCING PER:
MATERIAL
Polycarbonate
DO NOT SCALE DRAWING
PROPRIETARY AND CONFIDENTIAL
THE INFORMATION CONTAINED IN THIS DRAWING IS THE SOLE PROPERTY OF <INSERT COMPANY NAME HERE>. ANY REPRODUCTION IN PART OR AS A WHOLE WITHOUT THE WRITTEN PERMISSION OF <INSERT COMPANY NAME HERE> IS PROHIBITED.
Convective Heat Transfer Lab
Department of Mechanical Engineering
Baylor University
One Bear Place #97356
Waco, TX 76798
TITLE:
Circular Full Fillet t/d = 2.5
SIZE
B
DWG. NO.
Jet Plate Packet
REV
A
SCALE 1:2
WEIGHT:
SHEET 8 OF 11

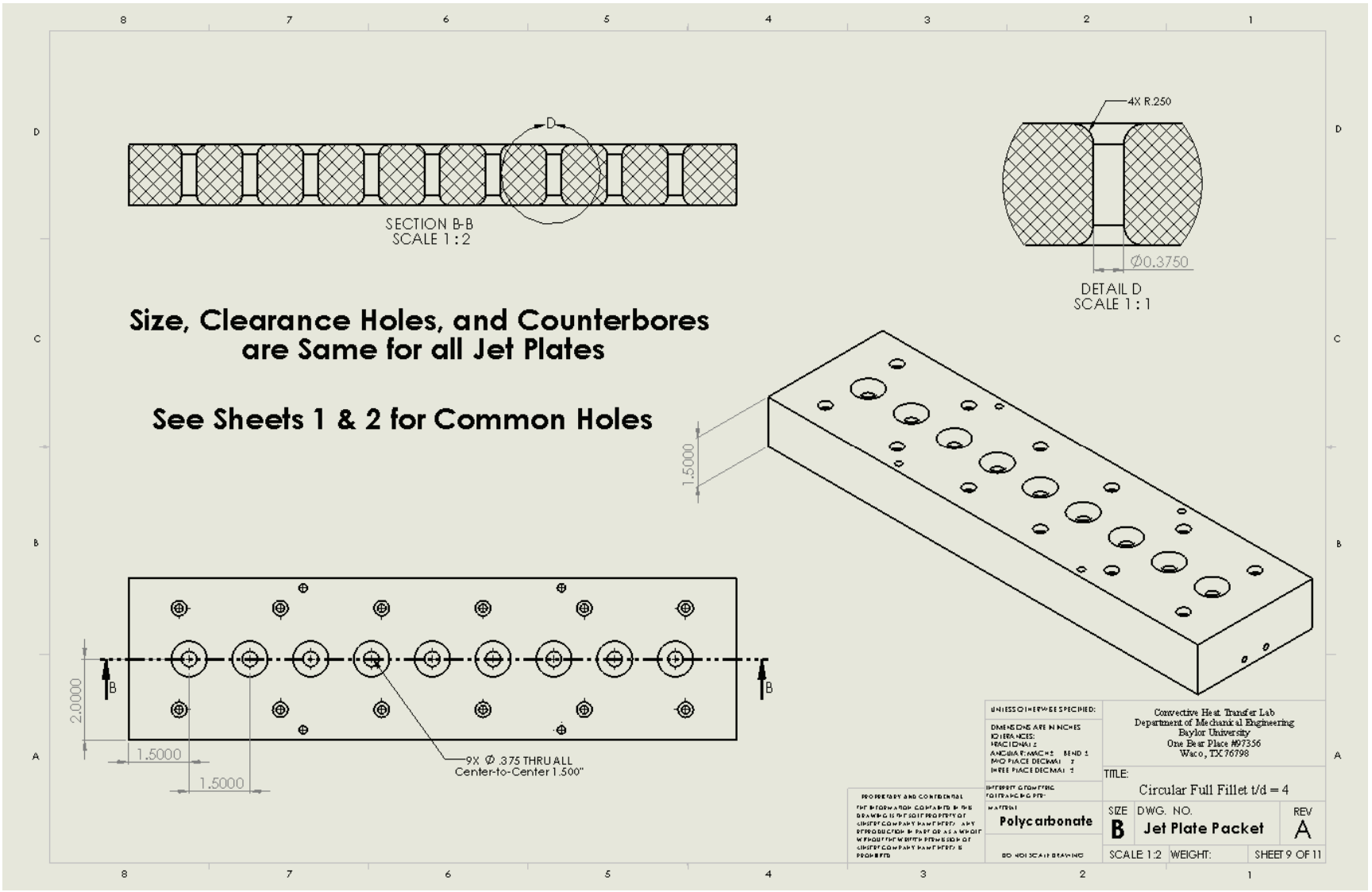
SECTION B-B
SCALE 1 : 2
4X R.250
Ø0.3750
DETAIL D
SCALE 1 : 1
Size, Clearance Holes, and Counterbores
are Same for all Jet Plates
See Sheets 1 & 2 for Common Holes
1.5000
2.0000
1.5000
1.5000
9X Ø .375 THRU ALL
Center-to-Center 1.500"
UNLESS OTHERWISE SPECIFIED:
DIMENSIONS ARE IN INCHES
TOLERANCES:
FRACTIONAL ±
ANGULAR: MACH ± BEND ±
TWO PLACE DECIMAL ±
THREE PLACE DECIMAL ±
INTERPRET GEOMETRIC TOLERANCING PER:
MATERIAL
Polycarbonate
DO NOT SCALE DRAWING
Convective Heat Transfer Lab
Department of Mechanical Engineering
Baylor University
One Bear Place #97356
Waco, TX 76798
TITLE:
Circular Full Fillet t/d = 4
SIZE
B
DWG. NO.
Jet Plate Packet
REV
A
SCALE 1:2
WEIGHT:
SHEET 9 OF 11

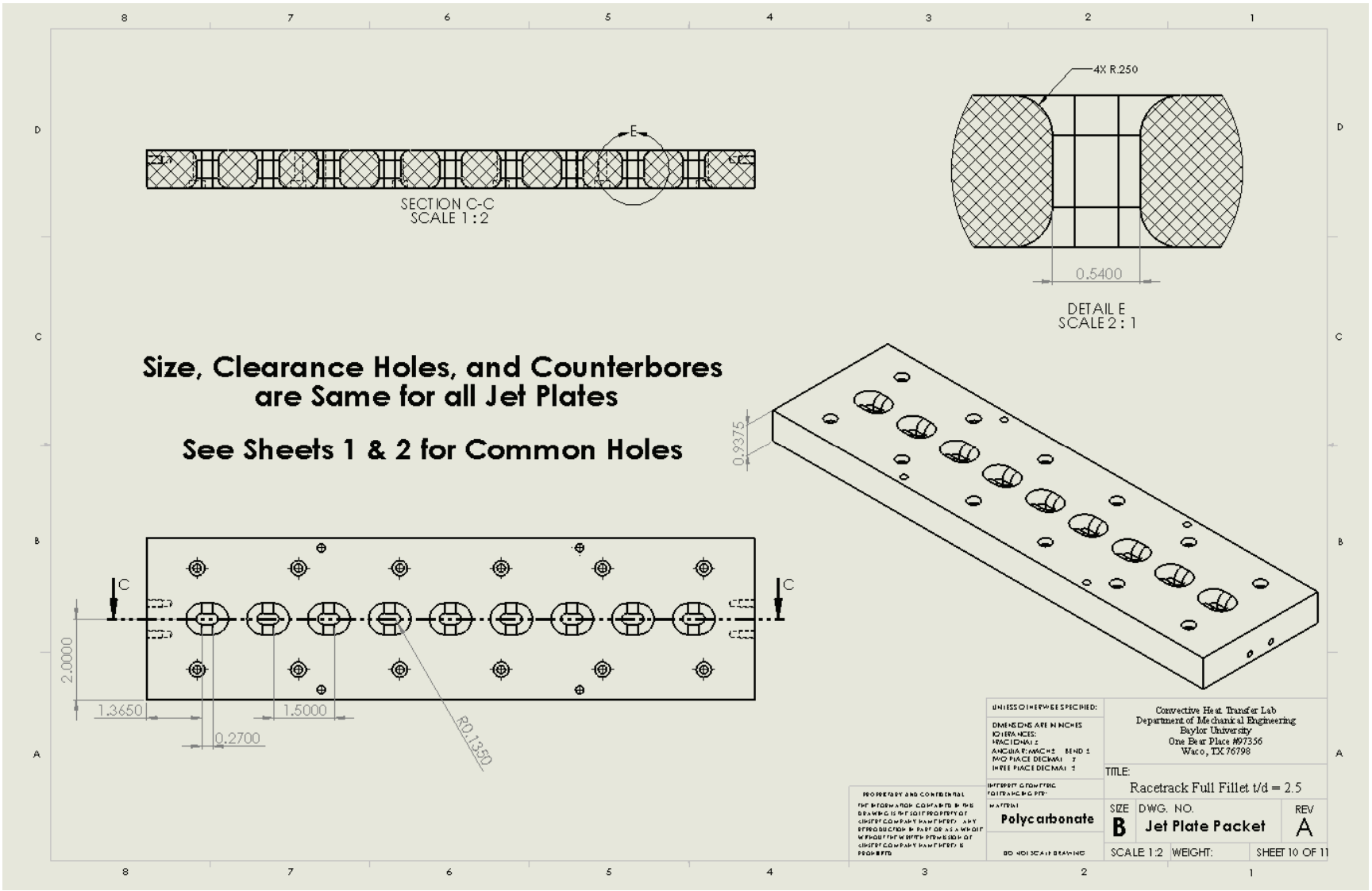
4X R.250
E
SECTION C-C
SCALE 1 : 2
0.5400
DETAIL E
SCALE 2 : 1
Size, Clearance Holes, and Counterbores
are Same for all Jet Plates
See Sheets 1 & 2 for Common Holes
0.9375
C
C
2.0000
1.3650
1.5000
0.2700
R0.1350
UNLESS OTHERWISE SPECIFIED:
DIMENSIONS ARE IN INCHES
TOLERANCES:
FRACTIONAL ±
ANGULAR: MACH ± BEND ±
TWO PLACE DECIMAL ±
THREE PLACE DECIMAL ±
INTERPRET GEOMETRIC TOLERANCING PER:
MATERIAL
Polycarbonate
DO NOT SCALE DRAWING
PROPRIETARY AND CONFIDENTIAL
THE INFORMATION CONTAINED IN THIS DRAWING IS THE SOLE PROPERTY OF <INSERT COMPANY NAME HERE>. ANY REPRODUCTION IN PART OR AS A WHOLE WITHOUT THE WRITTEN PERMISSION OF <INSERT COMPANY NAME HERE> IS PROHIBITED.
Convective Heat Transfer Lab
Department of Mechanical Engineering
Baylor University
One Bear Place #97356
Waco, TX 76798
TITLE:
Racetrack Full Fillet t/d = 2.5
SIZE
B
DWG. NO.
Jet Plate Packet
REV
A
SCALE 1:2
WEIGHT:
SHEET 10 OF 11

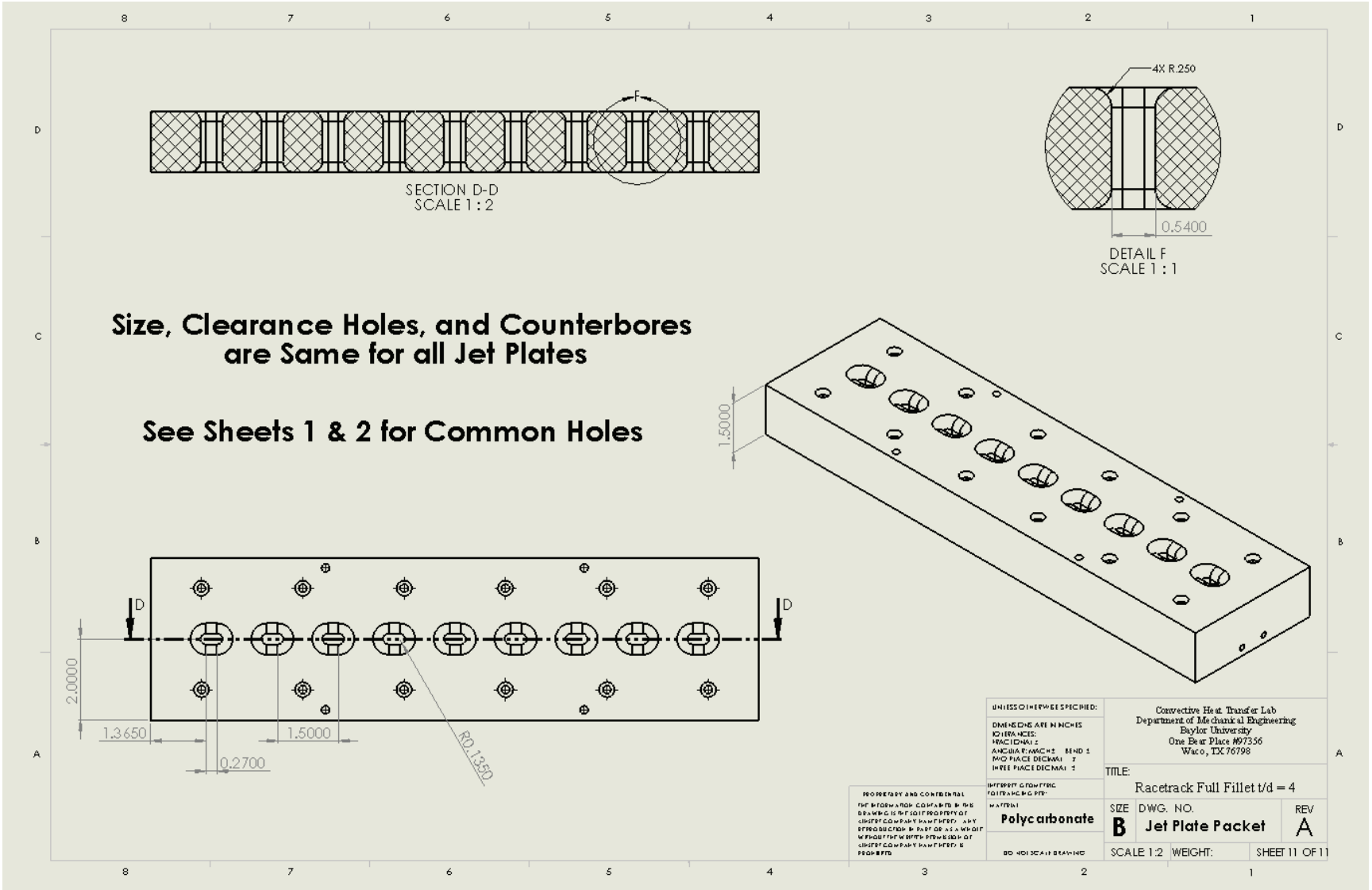
SECTION D-D
SCALE 1 : 2
4X R.250
0.5400
DETAIL F
SCALE 1 : 1
Size, Clearance Holes, and Counterbores are Same for all Jet Plates
See Sheets 1 & 2 for Common Holes
1.5000
2.0000
1.3650
1.5000
0.2700
R0.1350
Convective Heat Transfer Lab
Department of Mechanical Engineering
Baylor University
One Bear Place #97356
Waco, TX 76798
TITLE:
Racetrack Full Fillet t/d = 4
Polycarbonate
SIZE B
DWG. NO. Jet Plate Packet
REV A
SCALE 1:2
WEIGHT:
SHEET 11 OF 11

APPENDIX B

Uncertainty Analysis

```
clear all
close all
clc
%uncertainty analysis - aluminum plates

%% values

% % %Reynolds=10000
% W=0.009753; %m
% L=0.0175; %m
% P=(2*L)+(2*W); %m
% Ac=L*W; %m^2
% V=59.5; %V
% R=28.25; %ohms
% Vlow=8.14; %V
% Rlow=25.81; %ohms
% Vhigh=18.20; %V
% Rhigh=29.81; %ohms
% deltaT_low=13.9; %celcius
% deltaT_test=34.13; %celcius
% deltaT_high=53.96; %celcius
% Qhigh=0.0835; %W
% Qlow=0.0192; %W
% As=W*L; %m^2
% Qnet=0.88263; %W
% Dh=(4*Ac)/P;
% k=0.0262; %at 80 deg F (W/mK)
% h=144.52; %W/m2K
% Nu=48.9895;

% %Reynolds=30000
W=0.009753; %m
L=0.0175; %m
P=(2*L)+(2*W); %m
Ac=L*W; %m^2
V=80.9; %V
R=27.64; %ohms
Vlow=8.14; %V
Rlow=25.81; %ohms
Vhigh=18.20; %V
Rhigh=29.81; %ohms
deltaT_low=13.9; %celcius
deltaT_test=30.7; %celcius
deltaT_high=53.96; %celcius
Qhigh=0.0835; %W
Qlow=0.0192; %W
```

```
As=W*L; %m^2
Qnet=1.734; %W
Dh=(4*Ac)/P;
k=0.0262; %at 80 deg F (W/mK)
h=331.81; %W/m2K
Nu=112.47;


%% given uncertainties
w_L=0.0005*0.0254; %m
w_W=0.0005*0.0254; %m
w_P=0.0005*0.0254; %m
w_Lplate=0.0005*0.0254; %m
w_Wplate=0.0005*0.0254; %m
w_V=0.1; %V
w_R=0.1; %ohm
w_Vlow=0.1; %V
w_Rlow=0.1; %ohm
w_Vhigh=0.1; %V
w_Rhigh=0.1; %ohm
w_deltaT_high=0.3; %degrees celcius
w_deltaT_low=0.3; %degrees celcius
w_deltaT_test=0.3; %degrees celcius


%% calculated uncertainties

%Passage Entrance Area, Ac=L*W
w_Ac=((W*w_L)^2+(L*w_W)^2)^.5

%Perimeter, P=2L+2W
w_P=((2*w_L)^2+(2*w_W)^2)^.5

%Hydraulic Diameter, Dh=(4*Ac)/P
w_Dh=(((4/P)*w_Ac)^2+(((-4*Ac)/(P^2))*w_P)^2)^.5

%surface area of plate
w_As=((W*w_L)^2+(L*w_W)^2)^.5

%Energy in (test), Qin=V^2/R
w_Qin=(((((2*V)/R)*w_V)^2+(((-V^2)/R^2)*w_R)^2)^.5)/133

%heat in (low), Qlow=(Vlow^2)/Rlow
w_Qlow=(((((2*Vlow)/Rlow)*w_Vlow)^2+(((-Vlow^2)/Rlow^2)*w_Rlow)^2)^.5)/133

%heat in (high), Qhigh=(Vhigh^2)/Rhigh
```

```
w_Qhigh=(((((2*Vhigh)/Rhigh)*w_Vhigh)^2+(((-
Vhigh^2)/Rhigh^2)*w_Rhigh)^2)^.5)/133

%Heat Loss
w_Qloss=(((((deltaT_high-deltaT_low)/(deltaT_high-deltaT_test))*w_Qlow)^2+((-
(deltaT_low-deltaT_test)/(deltaT_high-deltaT_low))*w_Qhigh)^2+((((deltaT_low-
deltaT_test)*(Qhigh-Qlow))/(deltaT_high-deltaT_low)^2)*w_deltaT_high)^2+(((-
(deltaT_high-deltaT_test)*(Qhigh-Qlow))/(deltaT_low-
deltaT_high)^2)*w_deltaT_low)^2+(((Qhigh-Qlow)/(deltaT_high-
deltaT_low))*w_deltaT_test)^2)^.5)

%Qdotnet,Qnet=Qin-Qloss
w_Qnet=(w_Qin^2+w_Qloss^2)^.5

%heat transfer coefficient, h=(Qnet/As)/(Tw-Tb)=(Qnet/As)/deltaT
w_h=(((1/(As*deltaT_test))*w_Qnet)^2+((-Qnet/(As^2*deltaT_test))*w_As)^2+((-
Qnet/(As*deltaT_test^2))*w_deltaT_test)^2)^.5

%Nusselt Number, Nu=(h*Dh)/k
w_Nu=(((Dh/k)*w_h)^2+((h/k)*w_Dh)^2)^.5

%% Uncertainty Percentage

Nu_uncertainty=w_Nu/Nu*100
```

APPENDIX C

Data Reduction

```
clear all
close all
tic
% Load in data
data = importdata('TempData.txt');
Low = importdata('T_low.txt');
High = importdata('T_hi.txt');
Tdata = data.data;
T_low = Low.data;
T_hi = High.data;

% Gather steady state temperatures by averaging last 20ish seconds of data
T_F = mean(Tdata((end-20):end,:));      % Degrees F

% Convert Temperatures to Celcius
T = (T_F-32).*(5/9);                    % Degrees C

% Rearrange Temperature Data Array
T_jet = mean(T(1,123:127));

T_room = T(1,128);

% T = [0,0,0,0,T(1,1:5),mean(T(1,6:7)),T(1,8:11),0,0,0,0,0;
%      0,T(1,12:19),mean(T(1,20:21)),T(1,22:29),0;
%      0,T(1,30:36),mean(T(1,37:38)),mean(T(1,39:40)),mean(T(1,41:42)),T(1,43:49),0;
%
0,mean(T(1,50:51)),T(1,52:54),mean(T(1,55:56)),T(1,57:58),mean(T(1,59:60)),mean(T(1
,61:62)),mean(T(1,63:64)),T(1,65:66),mean(T(1,67:68)),T(69:71),mean(T(1,72:73)),0;
%      0,T(1,74:80),mean(T(1,81:82)),mean(T(1,83:84)),mean(T(1,85:86)),T(1,87:93),0;
%      0,T(1,94:101),mean(T(1,102:103)),T(1,104:111),0;
%      0,0,0,0,T(1,112:116),mean(T(1,117:118)),T(1,119:122),0,0,0,0,0;]

 T = [NaN,NaN,NaN,NaN,T(1,1:5),mean(T(1,6:7)),T(1,8:11),NaN,NaN,NaN,NaN,NaN;
     NaN,T(1,12:19),T(1,21:29),NaN;

NaN,T(1,30:36),mean(T(1,37:38)),mean(T(1,39:40)),mean(T(1,41:42)),T(1,43:49),NaN;

NaN,mean(T(1,50:51)),T(1,52:54),mean(T(1,55:56)),T(1,57:58),mean(T(1,59:60)),mean(
T(1,61:62)),mean(T(1,63:64)),T(1,65:66),mean(T(1,67:68)),T(69:71),mean(T(1,72:73)),
NaN;

NaN,T(1,74:80),mean(T(1,81:82)),mean(T(1,83:84)),mean(T(1,85:86)),T(1,87:93),NaN;
     NaN,T(1,94:101),mean(T(1,102:103)),T(1,104:111),NaN;
```

```
NaN,NaN,NaN,NaN,T(1,112:116),mean(T(1,117:118)),T(1,119:122),NaN,NaN,NaN,Na
N,NaN];

% flow information
W = 2;                          % Width of 1st pass channel inches
H = W;                          % Height of 1st pass channel inches
d_hENG = (4*W*H/(2*W+2*H));         % Hydrolic diameter inches
d_h = (4*W*H/(2*W+2*H))*0.0254;     % Hydrolic diameter meters supply channel
d_jet = 0.375*0.0254;               % Hydrolic diameter meters of the jet
D_o = 1.0;                      % Oriface diameter
D_p = 2.0;                      % Pipe diameter
P1 = 100;                       % Static pressure (psig)
P1hg = (P1+14.7)/0.4911;            % Absolute static pressure (inHg)
dP = 0.20;                      % Pressure drop accross oriface (inH2O)
T1 = (69.8+459.67);                 % Temperature before oriface
K = 0.62;                       % Flow Coefficient
Y = 0.98;                       % Expansion Factor
y = 1.0;                        % Supercompressibility Factor
G = 1.0;                        % Specific Gravity of Air
mu = 1.79e-5;                   % Dynamic Viscosity (N*s/m^2)
rho = 1.23;                     % Density of air at 300K and 125 psi (kg/m^3)

% Mass flow rate and Reynolds number calculation
mdotENG = 0.1145*D_o^2*K*Y*((P1hg/T1)*G*y*dP)^(.5);   % Mass flow rate (lbm/s)
mdot = 0.45359237*mdotENG;          % Mass flow rate (kg/s)
u = mdot/(rho*W*H*0.0254^2);        % Velocity in supply duct m/s
Re = rho*u*d_h/mu                   % Reynolds number in supply duct
Rejet = (4*mdot/(pi*d_jet*mu))/5    % Jet Reynolds number
ujet = Rejet*mu/(rho*d_jet)         % Jet velocity

% Gather heater voltage and resistance
V = 80.90;
R = 27.64;

% Heater information
%%%%%%%%%%%%%%%%%%%%
Q_in = V.^2./R;
% calculate power on a per plate basis
Q_in = Q_in./133;

% % Heat Loss Approximation (Watts)
%%%%%%
T_low = mean(T_low((end-20):end,:));    % Degrees F
T_hi = mean(T_hi((end-20):end,:));    % Degrees F

% % Convert Temperatures to Celcius
```

```
T_low = (T_low-32).*(5/9);          % Degrees C
T_hi = (T_hi-32).*(5/9);            % Degrees C

% Room Temperature C (heat loss)
Tr_low = T_low(1,128);
Tr_hi = T_hi(1,128);

T_low =
[NaN,NaN,NaN,NaN,T_low(1,1:5),mean(T_low(1,6:7)),T_low(1,8:11),NaN,NaN,NaN,
NaN,NaN;
      NaN,T_low(1,12:19),T_low(1,21:29),NaN;

NaN,T_low(1,30:36),mean(T_low(1,37:38)),mean(T_low(1,39:40)),mean(T_low(1,41:42
)),T_low(1,43:49),NaN;

NaN,mean(T_low(1,50:51)),T_low(1,52:54),mean(T_low(1,55:56)),T_low(1,57:58),mea
n(T_low(1,59:60)),mean(T_low(1,61:62)),mean(T_low(1,63:64)),T_low(1,65:66),mean(
T_low(1,67:68)),T_low(69:71),mean(T_low(1,72:73)),NaN;

NaN,T_low(1,74:80),mean(T_low(1,81:82)),mean(T_low(1,83:84)),mean(T_low(1,85:86
)),T_low(1,87:93),NaN;
      NaN,T_low(1,94:101),mean(T_low(1,102:103)),T_low(1,104:111),NaN;

NaN,NaN,NaN,NaN,T_low(1,112:116),mean(T_low(1,117:118)),T_low(1,119:122),NaN
,NaN,NaN,NaN,NaN];


T_hi =
[NaN,NaN,NaN,NaN,T_hi(1,1:5),mean(T_hi(1,6:7)),T_hi(1,8:11),NaN,NaN,NaN,NaN,N
aN;
      NaN,T_hi(1,12:19),T_hi(1,21:29),NaN;

NaN,T_hi(1,30:36),mean(T_hi(1,37:38)),mean(T_hi(1,39:40)),mean(T_hi(1,41:42)),T_hi
(1,43:49),NaN;

NaN,mean(T_hi(1,50:51)),T_hi(1,52:54),mean(T_hi(1,55:56)),T_hi(1,57:58),mean(T_hi(
1,59:60)),mean(T_hi(1,61:62)),mean(T_hi(1,63:64)),T_hi(1,65:66),mean(T_hi(1,67:68)),
T_hi(69:71),mean(T_hi(1,72:73)),NaN;

NaN,T_hi(1,74:80),mean(T_hi(1,81:82)),mean(T_hi(1,83:84)),mean(T_hi(1,85:86)),T_hi
(1,87:93),NaN;
      NaN,T_hi(1,94:101),mean(T_hi(1,102:103)),T_hi(1,104:111),NaN;

NaN,NaN,NaN,NaN,T_hi(1,112:116),mean(T_hi(1,117:118)),T_hi(1,119:122),NaN,NaN
,NaN,NaN,NaN,NaN];
```

```
% Voltage (heat loss)
V_low = 8.14;
V_hi = 18.20;

% Resistance (heat loss)
R_low = 25.95;
R_hi = 29.81;

% Power in per plate (heat loss)
Qin_low = (V_low.^2./R_low)./133;
Qin_hi = (V_hi.^2./R_hi)./133;

% Q Loss
Q_Loss = ((Qin_hi-Qin_low)./((T_hi-Tr_hi)-(T_low-Tr_low))).*...
    ((T-T_room)-(T_low-Tr_low))+Qin_low;

% Q_net per plate
Q_net = Q_in-Q_Loss;

% Surface Area Terms (E denotes English units of in^2)
As_E = 0.263981;            % Surface area per plate (in^2)
As = As_E*(.0254)^2;        % Surface area per plate (m^2)

% Heat Transfer Coefficients
h = Q_net./(As*(T-T_jet));

% Nusselt Numbers
kf = 0.0281;        % Thermal Conductivity of Air taken at apx 320K (W/m-K)
Nu = h*d_jet/kf

toc
```

```
clear all
close all

% Load in data
Tdata = load('200rpm_Temperatures.txt');
Pdata = load('200rpm_Pressures.txt');
Heater = load('200rpmHeater.csv');

% Gather steady state temperatures by averaging last 20ish seconds of data
T_F = mean(Tdata((end-20):end,2:26)); % Degrees F

% Convert Temperatures to Celcius
T = (T_F-32).*(5/9);                % Degrees C

% Rearrange Temperature Data Array into the form of:
%  | (column 1)
%  L  T  I1  I2  I3  <-- Plate location
% [3  3   3   3   3] <-- Plate number (row 1)
% [4  4   4   4   4]
% [5  5   5   5   5]
% [6  6   6   6   6]
% [jet, rotatingroom, outlet(channel end), stationaryroom1, statinaryroom2]
T = [T(1,1),T(1,5),T(1,9),T(1,13),T(1,17);
     T(1,2),T(1,6),T(1,12),T(1,14),T(1,18);
     T(1,3),T(1,7),T(1,11),T(1,15),T(1,19);
     T(1,4),T(1,8),T(1,10),T(1,16),T(1,20);
     T(1,21),T(1,23),T(1,22),T(1,24),T(1,25)];

% Do the same for the pressure data
P = mean(Pdata((end-20):end,2));      % psia

% flow information
W = 1.0625;                    % Width of 1st pass channel inches
H = 1.0625;                    % Height of 1st pass channel inches
D = 1.600;                     % Diameter of 2nd pass inches
P2 = (pi*D/2)+D;                   % Perimeter of 2nd pass inches
A2 = ((pi/4)*D^2)/2;               % Cross sectional area of 2nd pass inches^2
d_hENG = (4*W*H/(2*W+2*H));          % Hydrolic diameter inches
d_h1 = (4*W*H/(2*W+2*H))*0.0254;     % Hydrolic diameter meters 1st pass channel
d_h2 = 0.0254*4*(A2/P2);             % Hydrolic diameter meters 2nd pass channel
d_jet = 0.25*0.0254;               % Hydrolic diameter meters of the jet
D_o = 0.5;                     % Oriface diameter
D_p = 2.0;                     % Pipe diameter
P1 = 110;                      % Static pressure (psig)
```

```
P1hg = (P1+14.7)/0.4911;            % Absolute static pressure (inHg)
dP = 0.060;                         % Pressure drop accross oriface (inH2O)
T1 = (69.8+459.67);                 % Temperature before oriface
K = 0.62;                           % Flow Coefficient
Y = 0.98;                           % Expansion Factor
y = 1.0;                            % Supercompressibility Factor
G = 1.0;                            % Specific Gravity of Air
mu = 1.79e-5;                       % Dynamic Viscosity (N*s/m^2)
rho = 10.01;                        % Density of air at 300K and 125 psi (kg/m^3)

% Mass flow rate and Reynolds number calculation
mdotENG = 0.1145*D_o^2*K*Y*((P1hg/T1)*G*y*dP)^(.5);   % Mass flow rate (lbm/s)
mdot = 0.45359237*mdotENG;          % Mass flow rate (kg/s)
u1 = mdot/(rho*W*H*0.0254^2);       % Velocity 1st pass m/s
u2 = mdot/(rho*A2*0.0254^2);        % Velocity 2nd pass m/s
u_jet = mdot/(rho*(pi/4)*d_jet^2);  % Velocity of jet m/s
Re1 = rho*u1*d_h1/mu                % Reynolds number through 1st pass
Rejet = 4*mdot/(pi*d_jet*mu)        % Jet Reynolds number

% Baseline Heat transfer information
Pr = 0.707;                         % Prandtl number
Nu1 = 0.023*Re1^(0.8)*Pr^(0.4)      % Dittus-Boelter Correlation 1st pass

% Gather heater voltage and resistance
V = Heater(1,1:5);
R = Heater(2,1:5);

% Heater information
%%%%%%%%%%%%%%%%%%%%
Q_in = V.^2./R;
% calculate power on a per plate basis
Q_in = Q_in./9;
% convert to 4x5 for easier calculation
Q_in = [Q_in;Q_in;Q_in;Q_in];

% Heat Loss Approximation (Watts) (temperatures take from 9 hole
% impingement test with duct Reynolds number of 10000. Temperature data was
% collected only for odd numbered copper plates, and temperatures for even
% numbered plates were obtained by interpolation
%%%%%
T_low =      [ 99.6832   99.8274  105.1550  105.9030  104.8489
             102.3530  103.1002  107.2276  108.2237  107.8690
             104.5697  104.8612  109.0319  109.6486  109.7563
             106.1606  105.4118  110.1576  110.1772  110.6201
             106.9527  105.0535  110.1941  109.8090  110.5697
             106.7733  104.0142  108.7311  108.5434  109.6580
```

```
            105.4494  102.2291  105.3580  106.3799  107.7123
            102.8081   99.5597   99.6643  103.3179  104.5033
             98.6766   95.8679   91.2397   99.3569   99.8021];
%
T_hi =       [143.0779  140.8440  159.6422  160.7990  158.8649
            151.9989  150.2609  166.5207  168.2587  165.7547
            158.6488  156.1970  171.4267  172.6036  171.7513
            162.8038  158.8785  173.7393  173.9412  175.5590
            164.2403  158.5311  172.8376  172.3791  175.8822
            162.7345  155.3809  168.1008  168.0250  171.8300
            158.0628  149.6538  158.9079  160.9863  164.1298
            150.0014  141.5758  144.6382  151.3706  153.9137
            138.3266  131.3727  124.6707  139.2856  142.3138];
% Convert to celcius
T_low = (T_low-32).*(5/9);
T_hi = (T_hi-32).*(5/9);

% Create new array using only temperatures of interest (Plates 3,4,5,6)
% Array is set up
%  L  T  I1  I2  I3  <-- Plate location
% [3  3   3   3   3] <-- Plate number
% [4  4   4   4   4]
% [5  5   5   5   5]
% [6  6   6   6   6]
%%%%%
T_low = [T_low(3,1),T_low(3,2),T_low(3,3),T_low(3,4),T_low(3,5);
        T_low(4,1),T_low(4,2),T_low(4,3),T_low(4,4),T_low(4,5);
        T_low(5,1),T_low(5,2),T_low(5,3),T_low(5,4),T_low(5,5);
        T_low(6,1),T_low(6,2),T_low(6,3),T_low(6,4),T_low(6,5)];
%
T_hi = [T_hi(3,1),T_hi(3,2),T_hi(3,3),T_hi(3,4),T_hi(3,5);
       T_hi(4,1),T_hi(4,2),T_hi(4,3),T_hi(4,4),T_hi(4,5);
       T_hi(5,1),T_hi(5,2),T_hi(5,3),T_hi(5,4),T_hi(5,5);
       T_hi(6,1),T_hi(6,2),T_hi(6,3),T_hi(6,4),T_hi(6,5)];

% Voltage (heat loss)
V_low = [7.875,7.49,7.125,7.286,8.286];
V_hi = [13.77,12.406,13.93,11.93,15.22];

% Resistance (heat loss)
R_low = [42.82,42.70,42.37,42.73,42.57];
R_hi = [42.98,42.85,42.56,42.92,42.74];

% Power in per plate (heat loss)
Qin_low = (V_low.^2./R_low)./9;
Qin_hi = (V_hi.^2./R_hi)./9;
```

```
% Make 1x5 matrix into a 4x5 for easy multiplication in next step
Qin_low = [Qin_low;Qin_low;Qin_low;Qin_low];
Qin_hi = [Qin_hi;Qin_hi;Qin_hi;Qin_hi];
% Rotating Room Temperature F (heat loss)
Tr_low = 83.0490;
Tr_hi = 84.9415;
% Convert to Celcius
Tr_low = (Tr_low-32)*(5/9);
Tr_hi = (Tr_hi-32)*(5/9);

% Q Loss
Q_Loss = ((Qin_hi-Qin_low)./((T_hi-Tr_hi)-(T_low-Tr_low))).*...
   ((T(1:4,1:5)-T(5,2))-(T_low-Tr_low))+Qin_low;

% Q_net per plate
Q_net = Q_in-Q_Loss;

% Surface Area Terms (E denotes English units of in^2)
As_dE = .879;              % Surface area per plate in supply duct
As_cE = .780;              % Surface area per plate in curved channel
As_d = As_dE*(.0254)^2;    % Surface area per plate in supply duct (m^2)
As_c = As_cE*(.0254)^2;    % Surface area per plate in curved channel (m^2)

% Heat Transfer Coefficients
   % Square channel side
hL = Q_net(:,1)./(As_d*(T(1:4,1)-T(5,1)));
hT = Q_net(:,2)./(As_d*(T(1:4,2)-T(5,1)));
   % Curved channel side
h1 = Q_net(:,3)./(As_c*(T(1:4,3)-T(5,1)));
h2 = Q_net(:,4)./(As_c*(T(1:4,4)-T(5,1)));
h3 = Q_net(:,5)./(As_c*(T(1:4,5)-T(5,1)));
% put back in easy to read array
h200 = [hL(1),hT(1),h1(1),h2(1),h3(1);
    hL(2),hT(2),h1(2),h2(2),h3(2);
    hL(3),hT(3),h1(3),h2(3),h3(3);
    hL(4),hT(4),h1(4),h2(4),h3(4)]

% Nusselt Numbers
kf = 0.0281;       % Thermal Conductivity of Air taken at apx 320K (W/m-K)
NuL = hL*d_h1/kf;
NuT = hT*d_h1/kf;
Nu1 = h1*d_jet/kf;
Nu2 = h2*d_jet/kf;
Nu3 = h3*d_jet/kf;
% put in easy to read array
Nu200_15k = [NuL(1),NuT(1),Nu1(1),Nu2(1),Nu3(1);
```

```
        NuL(2),NuT(2),Nu1(2),Nu2(2),Nu3(2);
        NuL(3),NuT(3),Nu1(3),Nu2(3),Nu3(3);
        NuL(4),NuT(4),Nu1(4),Nu2(4),Nu3(4)]

%
```

APPENDIX D

LabView Virtual Instruments

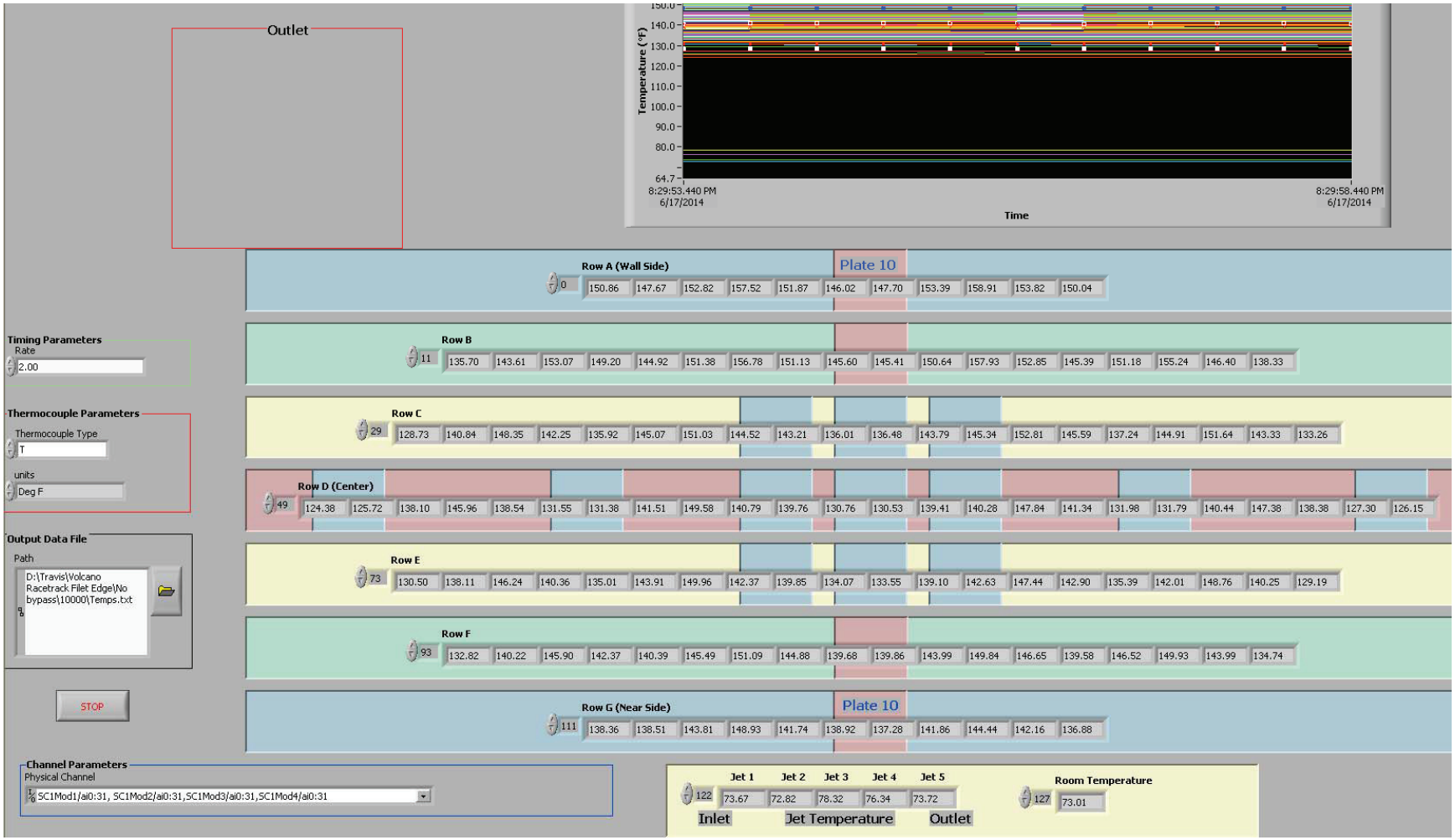

Figure D.1: Honeywell Steady State Heat Transfer LabView VI

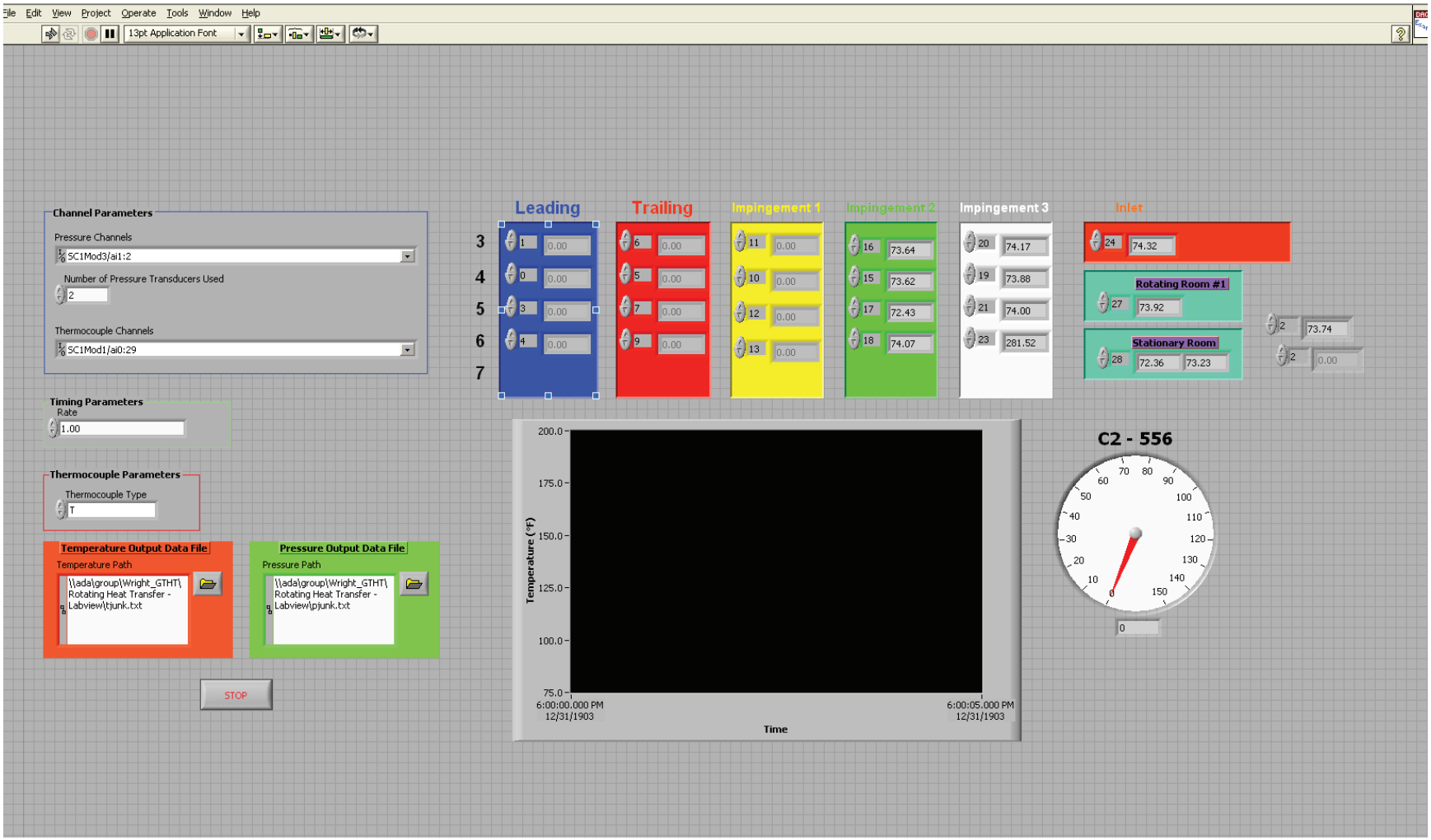

Figure D.2: Rotating Steady State Heat Transfer LabView VI

REFERENCES

[1] Han, J.C., Dutta, S., and Ekkad, S., 2013, *Gas Turbine Heat Transfer and Cooling Technology*, 2nd ed., CRC Press, Boca Raton, Florida, 869 pages.

[2] Han, J. C. and Wright, L. M., 2006, "Enhanced Internal Cooling of Turbine Blades and Vanes," The Gas Turbine Handbook, DOE, Office of Fossil Energy, National Energy Technology Laboratory.

[3] Han, B. and Goldstein, R. J., 2001, "Jet-Impingement Heat Transfer in Gas Turbine Systems," *Annals New York Academy of Sciences*, 934(1), pp. 147-161.

[4] Jordan, C. N., 2012, *Experimental Investigation of Leading Edge Jet Impingement with Varying Jet Geometries and Inlet Supply Conditions for Turbine Cooling Applications*, Master's Thesis, Baylor University, Department of Mechanical Engineering.

[5] Jordan, C.N., Elston, C. A., Wright, L.M., and Crites, D.C., 2012, "Impingement Heat Transfer on a Cylindrical, Concave Surface with Varying Jet Geometries," ASME Paper No. GT2012-68818.

[6] Jordan, C.N., Wright, L.M., and Crites, D.C., 2013, "Leading Edge Impingement with Racetrack Shaped Jets and Varying Inlet Supply Conditions," ASME Paper No. GT2013-94611.

[7] Jordan, C.N., Wright, L.M., and Crites, D.C., 2012, "Effect of Impingement Supply Condition on Leading Edge Heat Transfer with Rounded Impinging Jets," ASME Paper No. HT2012-58410.

[8] Elston, C. A. and Wright, L. M., 2012, "Leading Edge Jet Impingement Under High Rotation Numbers," ASME Paper No. IMECE2012-88332.

[9] Florschuetz, L. W., Metzger, D. E., Su, C. C. Isoda, Y., and Tseng, H. H., 1984, "Heat Transfer Characteristics for Jet Arrays Impingement with Initial Crossflow," *ASME Journal of Heat Transfer*, Vol. 106, pp. 34-41.

[10] Incropera, F. P., Dewitt, D. P., 2011, *Fundamentals of Heat and Mass Transfer*, 7th ed., John Wiley & Sons, Inc., Hoboken, NJ.

[11] Huang, Y., Ekkad, S. V. and Han, J. C., 1998, "Detailed Heat Transfer Distributions Under an Array of Orthogonal Impinging Jets," *Journal of Thermophysics and Heat Transfer*, 12(1), pp. 73-79.

[12] Kercher, D. M., and Tabakoff,W., 1970, "Heat Transfer of a Circular Jet with and without Cross Flow," *International Journal of Heat and Mass Transfer*, Vol. 106, pp. 34-41.

[13] Ekkad, S.V., Huang, Y., and Han, J. C., 1999, "Impingement Heat Transfer on a Target Plate with Film Cooling Holes," *AIAA Journal of Thermophysics and Heat Transfer*, Vol. 13, pp. 522-528.

[14] Chupp, R. E., Helms, D. E., McFadden, P. W., and Brown, T. R., 1969, "Evaluation of Internal Heat Transfer Coefficients for Impingement Cooled Turbine Airfoils" *AIAA J. of Aircraft,* Vol. 6(3), pp. 203-208.

[15] Lee, D. H., Chung, Y. S., and Won, S. Y., 1999, "The Effect of Concave Surface Curvature on Heat Transfer from a Fully Developed Round Impinging Jet." *International Journal of Heat and Mass Transfer*, Vol. 42, pp. 2489-2497.

[16] Metzger, D. E., Yamashita T., and Jenkins, C. W., 1972, "Impingement Cooling of Concave Surfaces with Lines of Circular Air Jets," ASME *Journal Eng. Power,* Vol. 91, pp. 149-158.

[17] Fenot, M., Vullierme, J. –J, and Dorignac, E., 2005, "A Heat Transfer Measurement of Jet Impingement with High Injection Temperature," *C. R. Mechanique*, Vol. 333, pp. 778-782.

[18] Martin, E. L., 2011, *Experimental and Numerical Investigation of High Temperature Jet Impingement for Turbine Cooling Applications*, Master's Thesis, Baylor University, Department of Mechanical Engineering.

[19] Tabakoff, W. and Clevenger, W., 1972, "Gas Turbine Blade Heat Transfer Augmentation by Impingement of Air Jets Having Various Configurations," *ASME Journal of Eng. Power*, Vol. 94, pp. 51-60.

[20] Bunker, R. S. and Metzger, D. E., 1990" Local Heat Transfer in Internally Cooled Turbine Airfoil Leading Edge Regions: Part I – Impingement Cooling Without Film Coolant Extraction." *ASME J. Turbomachinery*, Vol. 112, pp. 451-458

[21] Metzger, D. E. and Bunker, R. S., 1990" Local Heat Transfer in Internally Cooled Turbine Airfoil Leading Edge Regions: Part II – Impingement Cooling With Film Coolant Extraction." *ASME J. Turbomachinery*, Vol. 112, pp. 459-466

[22] Hrycak, P., 1981, "Heat Transfer from a Row of Impinging Jets to Concave Cylindrical Surfaces," *International Journal of Heat and Mass Transfer*, Vol. 112, pp. 407-419.

[23] Fenot, M., Vullierme, J. –J, and Dorignac, E., 2008, "An Experimental Study on Hot Round Jets Impinging on a Concave Surface," *International Journal of Heat and Fluid Flow*, Vol. 29, pp. 945-956.

[24] Cornaro, C., Fleischer, A. S., and Goldstein, R. J., 1999, "Flow Visualization of a Round Jet Impinging on Cylindrical Surfaces," *International Journal of Heat and Mass Transfer*, Vol. 20, pp. 66-78.

[25] Gau, C. and Chung, C. M., 1991, "Surface Curvature Effects on Slot-Air-Jet Impingement Cooling Flow and Heat Transfer Process," *ASME Journal of Heat Transfer*, 113, pp. 858-864.

[26] Choi, M., Yoo, H. S., Yang, G., Lee, J. S. and Sohn, D. K., 1999, "Measurements of Impinging Jet Flow and Heat Transfer on a Semi-Circular Concave Surface," *International Journal of Heat and Mass Transfer*, 43, pp. 1811-1822.

[27] Yang, G., Choi, M., and Lee, J. S., 1998, "An Experimental Study of Slot Jet Impingement Cooling on Concave Surface: Effects of Nozzle Configuration and Curvature," *International Journal of Heat and Mass Transfer*, 42, pp. 2199-2209.

[28] Gulati, P., Katti, V., and Pradhu, S.V., 2009, "Influence of the Shape of the Nozzle on Local Heat Transfer Distribution between Smooth Flat Surface and Impinging Air Jet," *Int. J. Thermal Sciences*, Vol. 49, pp. 602-617.

[29] Lee, J. and Lee, S. J., 2000, "The Effect of Nozzle Aspect Ratio of Stagnation Region Heat Transfer Characteristics of Elliptic Impinging Jets," *International Journal of Heat and Mass Transfer*, Vol 43, pp. 555-575.

[30] Taslim, M.E. and Setayeshgar, L., 2001, "Experimental Leading-Edge Impingement Cooling through Racetrack Crossover Holes," ASME Paper No. 2001-GT-0153.

[31] Taslim, M. E., Pan, Y., and Bakhtari, K., 2002, "Experimental Racetrack Shaped Jet Impingement on a Roughened Leading-Edge Wall With Film Holes," ASME Paper No. GT-2002-30477.

[32] Taslim, M. E. and Bethka, D., 2009, "Experimental and Numerical Impingement Heat Transfer in an Airfoil Leading-Edge Cooling Channel with Cross-Flow," *ASME J. Turbomachinery*, Vol. 131, Article 011021, 7 pages.

[33] Brignoni, L. A. and Garimella, S. V., 2000, "Effects of Nozzle-Inlet Chamfering on Pressure Drop and Heat Transfer in Confined Air Jet Impingement," *International Journal of Heat and Mass Transfer*, Vol. 43, pp. 1133-1139.

[34] Martin, E.L., Wright, L.M., and Crites, D.C., 2012, "Impingement Heat Transfer Enhancement on a Cylindrical, Leading Edge Model with Varying Jet Temperatures," ASME Paper No. GT2012-68817.

[35] Wagner, J.H., Johnson, B.V., and Hajek, T.J., 1991, "Heat Transfer in Rotating Passages with Smooth Walls and Radial Outward Flow," *ASME J. Turbomachinery*, Vol. 113, pp. 42 – 51.

[36] Wagner, J.H., Johnson, B.V., and Kopper, F.C., 1991, "Heat Transfer in Rotating Serpentine Passages with Smooth Walls," *ASME J. Turbomachinery*, Vol. 113, pp. 321 – 330.

[37] Johnson, B.V., Wagner, J.H., Steuber, G.D., and Yeh, F.C., 1994, "Heat Transfer in Rotating Serpentine Passages with Selected Model Orientations for Smooth or Skewed Trip Walls," *ASME J. Turbomachinery*, Vol. 116, pp. 738 – 744.

[38] Parsons, J.A., Han, J.C., and Zhang, Y.M., 1994, "Wall Heating Effect on Local Heat Transfer in a Rotating Two-Pass Square Channel with Rib Turbulators," *International J. Heat and Mass Transfer*, Vol. 38, No. 9, pp. 1411 – 1420.

[39] Zhang, Y.M., Han, J.C., Parsons, J.A., and Lee, C.P., 1995, "Surface Heating Effects on Local Heat Transfer in a Rotating Two-Pass Square Channel with 60° Angled Rib Turbulators," *ASME J. Turbomachinery*, Vol. 117, No. 2, pp. 272 – 278.

[40] Dutta, S. and Han, J.C., 1996, "Local Heat Transfer in Rotating Smooth and Ribbed Two-Pass Square Channels with Three Channel Orientations," *ASME J. Heat Transfer*, Vol. 118, pp. 578 – 584.

[41] Griffith, T.S., Al-Hadhrami, L., and Han, J.C., 2002, "Heat Transfer in Rotating Rectangular Channels (AR=4) with Angled Ribs," *ASME J. of Heat Transfer*, Vol. 124, pp. 617 -625.

[42] Fu, W.L., Wright, L.M., and Han, J.C., 2005, "Heat Transfer in Two-Pass Rotating Rectangular Channels (AR = 1:2 and AR = 1:4) with 45° Angled Rib Turbulators," *ASME J. Turbomachinery*, Vol. 127, No. 4, pp. 164 – 174.

[43] Fu, W.L., Wright, L.M., and Han, J.C., 2006, "Rotational Buoyancy Effects on Heat Transfer in Five Different Aspect-Ratio Rectangular Channels with Smooth Walls and 45-Degree Ribbed Walls," *ASME J. Heat Transfer*, Vol. 128, No. 11, pp. 1130-1141.

[44] Parsons, J.A., Han, J.C., and Zhang, Y.M., 1995, "Effects of Model Orientation and Wall Heating Condition on Local Heat Transfer in a Rotating Two-Pass Square Channel with Rib Turbulators" *International J. Heat and Mass Transfer*, Vol. 38, No. 7, pp. 1151 – 1159.

[45] Wright, L.M., Lee, E., and Han, J.C., 2004, "Effect of Rotation on Heat Transfer in Rectangular Channels with Pin-Fins," *AIAA J. Thermophysics and Heat Transfer*, Vol. 18, No. 2, pp. 263-272.

[46] Zhou, F., Lagrone, J., and Acharya, S., 2004, "Internal Cooling in 4:1 AR Passages at High Rotation Numbers," ASME Paper No. GT2004-53501.

[47] Wright, L.M., Liu, Y.H., Han, J.C., and Chopra, S., 2008, "Heat Transfer in Trailing Edge, Wedge-Shaped Cooling Channels under High Rotation Numbers," *ASME J. of Heat Transfer*, Vol. 130, No. 7, Article No. 071701, 11 pages.

[48] Liu, Y.H., Huh, M., Wright, L.M., and Han, J.C., 2009, "Heat Transfer in Trailing-Edge Channels with Slot Ejection Under High Rotation Numbers," *AIAA J. of Thermophysics and Heat Transfer*, Vol. 23, No. 2, pp. 305-315.

[49] Liu, Y.H., Huh, M., Han, J.C., and Moon, H.K., 2009, "High Rotation Number Effect on Heat Transfer in a Triangular Channel with 45°, Inverted 45°, and 90° Ribs," ASME Paper No. GT2009-59216.

[50] Huh, M., Lei, J., Liu, Y.H., and Han, J.C., 2011, "High Rotation Number Effects on Heat Transfer in a Rectangular (AR = 2:1) Two-Pass Channel," *ASME J. Turbomachinery*, Vol. 133, Article No. 021001, 11 pages.

[51] Rallabandi, A.P., Liu, Y.H., and Han, J.C., 2011, "Heat Transfer in Trailing Edge Wedge-Shaped Pin-Fin Channels with Slot Ejection Under High Rotation Numbers," *ASME J. Thermal Science and Engineering Applications*, Vol. 3, Article No. 021007, 9 pages.

[52] Huh, M., Lei, J., and Han, J.C., 2012, "Influence of Channel Orientation on Heat Transfer in a Two-Pass Smooth and Ribbed Rectangular Channel (AR = 2:1) Under Large Rotation Numbers," *ASME J. Turbomachinery*, Vol. 134, Article No. 011022, 14 pages.

[53] Parsons, J.A., Han, J.C., and Lee, C.P., 1998, "Rotation Effect on Jet Impingement Heat Transfer in Smooth Rectangular Channels with Four Heated Walls and Radially Outward Crossflow," *ASME J. Turbomachinery*, Vol. 120, pp. 79 – 85.

[54] Parsons, J.A. and Han, J.C., 1998, "Rotation Effect on Jet Impingement Heat Transfer in Smooth Rectangular Channels with Heated Target Walls and Radially Outward Cross Flow," *International J. Heat and Mass Transfer*, Vol. 41, No. 13, pp. 2059 – 2071.

[55] Parsons, J.A. and Han, J.C., 1996, "Rotation Effect on Jet Impingement Heat Transfer in Smooth Rectangular Channels with Heated Target Walls and Film Coolant Extraction," ASME Paper No. 96-WA/HT-9.

[56] Parsons, J.A., Han, J.C., and Lee, C.P., 2003, "Rotation Effect on Jet Impingement Heat Transfer in Smooth Rectangular Channels with Four Heated Walls and Film Coolant Extraction," ASME Paper No. GT2003-38905.

[57] Akella, K.V. and Han, J.C., 1998, "Impingement Cooling in Rotating Two-Pass Rectangular Channels," *AIAA J. Thermophysics and Heat Transfer*, Vol. 12, No. 4, pp. 582 – 588.

[58] Akella, K.V. and Han, J.C., 1999, "Impingement Cooling in Rotating Two-Pass Rectangular Channels with Ribbed Walls," *AIAA J. Thermophysics and Heat Transfer*, Vol. 13, No. 3, pp. 364-371.

[59] Lamont, J.A. and Ekkad, S.V., 2011, "Effects of Rotation on Jet Impingement Channel Heat Transfer," ASME Paper No. GT2011-45744.

[60] Kline, S. J., and McClintock, F. A. 1953, "Describing Uncertainties in Single-Sample Experiments," *Mech. Eng.* (AM. Soc. Mech. Eng.), 75, pp. 3-8.

[61] Leary, W. A., Tsai, D. H., 1951, "Metering of Gases by Means of the ASME Square-Edged Orifice With Flange Taps," Sloan Laboratory for Automotive and Aircraft Engines, Massachusetts Institute of Technology.

[62] Elston, C. A., 2013, *Numerical Prediction and Correlation of Leading Edge Jet Impingement with Varying Jet Shapes and Flow Conditions for Gas Turbine Cooling*, Master's Thesis, Baylor University, Department of Mechanical Engineering.